**DISCLAIMER:**

This document does not meet the
current format guidelines of
the Graduate School at
The University of Texas at Austin.

It has been published for
informational use only.

**The Dissertation Committee for Mahmoud Hasan Alnazghah Certifies that this is the approved version of the following Dissertation:**

# Sequence Stratigraphy and Geomodeling of the Upper Pennsylvanian Canyon and Cisco formations in SACROC Field, West Texas: Insights into The Late Paleozoic Glaciation

**Committee:**

Charles Kerans, Supervisor

Steve Bachtel

Daniel O Breecker

Xavier Janson

Rowan Martindale

# Sequence Stratigraphy and Geomodeling of the Upper Pennsylvanian Canyon and Cisco formations in SACROC Field, West Texas: Insights into The Late Paleozoic Glaciation

**by**

**Mahmoud Hasan Alnazghah**

**Dissertation**

Presented to the Faculty of the Graduate School of

The University of Texas at Austin

in Partial Fulfillment

of the Requirements

for the Degree of

**Doctor of Philosophy**

**The University of Texas at Austin**

**August 2018**

# Dedication

To my mother and siblings

and

to my wife, Zainab, and my sons, AlQasim and Ali

## Acknowledgements

I am indebted to many people who have helped and encouraged me throughout the various stages of my doctoral research. My utmost gratitude goes to Dr. Charles Kerans for his inspiration, guidance, and constructive discussion throughout the years. I am grateful to my mentor in Saudi Aramco Dr. Aus Al-Tawil, who ignited my interest in carbonates, trained me, guided me, and supported me throughout my career. I would like to thank Dr. Mohammed Khalifa who went out of his way to make sure I got everything I needed to succeed.

I would like to thank my dissertation committee members: Dr. Steve Bachtel, Dr. Rowan C Martindale, Dr. Daniel O Breecker, and Dr. Xavier Janson for their guidance and helpful comments and suggestions.

I especially thank my wife for her unwavering support and tolerance during all time I have been away. I would like to thank my mother and siblings for their constant love and support.

I wish to thank Saudi Aramco, Reservoir Characterization Department for my scholarship. I would like to thank Reservoir Characterization Research Laboratory sponsors for the data. I would like to thank all team members at the Core Research Center of the Bureau of Economic Geology, especially Nathan Ivicic and William Molthen. I would like to thank Dallas Dunlap, Thomas Hess, David Spindler, Hasart Mahmood, Khalilurhaman, Sherif Khattab, and Muntasir Elfaki for software support. Many thanks to my friends and colleagues: Luis Pomar, Abdullah Al-Shamsi, Mohammed Fallatah, Abdulkarim Al-Hussaini, Khalaf AlTemimi, Hussain Bandah, Ali Al-Saeed, Marwan Al-Thagafy, and Sami Al-Saadan. Special thanks to my friends who picked me up when I was giving up: Ahmed AlZayer, Yaser AlZayer and Ahmed Al-Nahwi.

# Abstract

## Sequence Stratigraphy and Geomodeling of the Upper Pennsylvanian Canyon and Cisco formations in SACROC Field, West Texas: Insights into The Late Paleozoic Glaciation

Mahmoud Hasan Alnazghah, Ph.D

The University of Texas at Austin, 2018

Supervisor: Charles Kerans

The Late Paleozoic has long been recognized as a time of extensive glaciation. Recent work has suggested that the Late Paleozoic represents greenhouse setting, with limited to no ice caps. The nature of the climate, greenhouse vs. icehouse, plays a major control on the observed stratigraphic architecture. Compared to the layered architecture of the greenhouse climate, where accommodation is filled to spill, the stratigraphic architecture of icehouse climate is dominated by complex geometries, discontinuous facies belts and frequent subaerial exposure surfaces and diastems. Such extreme heterogeneity represents a challenge in modeling subsurface reservoirs, which are inherently poorly sampled.

A high resolution sequence stratigraphic framework was constructed for the Late Pennsylvanian units in the Scurry Area Canyon Reef Operators Committee (SACROC) Field using an extensive dataset including more than 7000 ft of core, 650 wireline logs, and 3D seismic volume. The stratigraphic framework was used to approximate water depths of

lithofacies and subsequently used to construct a eustatic sea level curve for Late Pennsylvanian time. Several modeling methods were tested to investigate the best approach to represent complex icehouse carbonate systems in the subsurface.

The sequence stratigraphic framework of the Late Pennsylvanian shows a transition from layered-cake stratigraphy during the deposition of the Missourian Canyon Formation into a wedding-cake architecture during the deposition of the Virgilian Cisco Formation. This transition and the refined eustatic curve are indicative of an increased icehouse conditions that peaked during the Virgilian. Periodicity was estimated from number of cycles and time to be 100 k.y. and 343 k.y. for the Missourian and Virgilian respectively, suggestive of short- and long-term eccentricity signal. Modeling results showed that pure stochastic methods failed to capture the complexity expected within icehouse carbonate platforms. On the other hand, multiple-point statistics algorithm, which is guided by conceptual models based on outcrop and modern analogs, generated the most geologically sound models.

The refined eustatic curve for the Late Pennsylvanian is useful in improving and constraining paleoclimate, which can be employed in future climate simulations. The modeling efforts presented here are one of the few to capture the expected 3D heterogeneity of icehouse carbonate platforms, which is key for developing similar hydrocarbon reservoirs.

# Table of Contents

# List of Tables

# List of Figures

# CHAPTER 1: INTRODUCTION

The Late Paleozoic Ice Age (LPIA) records peak icehouse conditions comparable to the Last Glacial Maximum of the Pleistocene (Heckel, 1977; Faribanks, 1989; Crowley and Baum, 1991; Isbell et al., 2003; Peltier and Fairbanks, 2006). Although there is a universal agreement that during the LPIA ice sheets grew over Gondwana, located in the southern hemisphere, the character and the timing of these ice sheets are still debated (Montañez and Poulsen, 2013). The LPIA was originally thought to be one massive ice sheet that covered most of Gondwana (Veevers and Powell, 1987; Isbell et al., 2003; Rygel et al., 2008); however, ongoing research has revealed that the LPIA consisted of multiple glacial-interglacial intervals intervals (Fielding et al., 2008; Bishop et al., 2010; Martin et al., 2012).

Icehouse climate is a period in the geologic record that has polar ice caps, extending for more than 5000 $km^2$ and are at least 1 mile thick, that calve marine icebergs (Kidder and Worsley, 2012). Waxing and waning of ice sheets drive a high-amplitude, high-frequency eustatic sea level fluctuations that result in complex stratigraphic architecture of carbonate platforms (Read, 1985; Read, 1995). Such carbonate platforms are characterized by unfilled accommodation (Eberli and Grammer, 1999; Janson and Kerans, 2007; Eberli, 2013), missed beats (Hardie et al., 1986; Goldhammer et al., 1990), and multiple exposure and diastems horizons (Read, 1985) that make chronostratigraphic correlation in the subsurface challenging. Conventional stochastic models cannot capture the heterogeneity intrinsic to icehouse carbonate platforms. Only few studies attempted to model icehouse

carbonate platforms that focused on outcrops (Adams et al., 2005; Aigner et al., 2007; Janson and Madriz, 2012) and modern analogs (Rush and Rankey, 2017).

The Scurry Area Canyon Reef Operators Committee (SACROC) Field in West Texas produced over 1.2 billion barrels of oil from the Pennsylvanian section (Hawkins et al., 1996). The economic importance and extensive development history of the SACROC field offered a closely-spaced dataset including core, wireline logs and 3D seismic data. This provided a rare opportunity to characterize and model complex icehouse carbonate platforms at a high-resolution.

The Kelly-Snyder Field was discovered in 1948, and was renamed to Scurry Area Canyon Reef Operators Committee (SACROC) Field in 1953 (Smith, 2010). The SACROC Field is located on the eastern limb of the Horseshoe Atoll (Fig. 1.1) in the northern portion of the Midland Basin. Horseshoe Atoll was located near the paleoequator (Fig. 1.2) during the Late Paleozoic (Witzke, 1990; Golonka, 2011) and was dominated by thick carbonate succession (Fig. 1.3) consisting of strata which extend from the Desmoinesian (Strawn) to the Wolfacampian (Wolfcamp) (Galloway et al., 1983; Vest, 1970; Schatzinger, 1987; Wright, 2011).

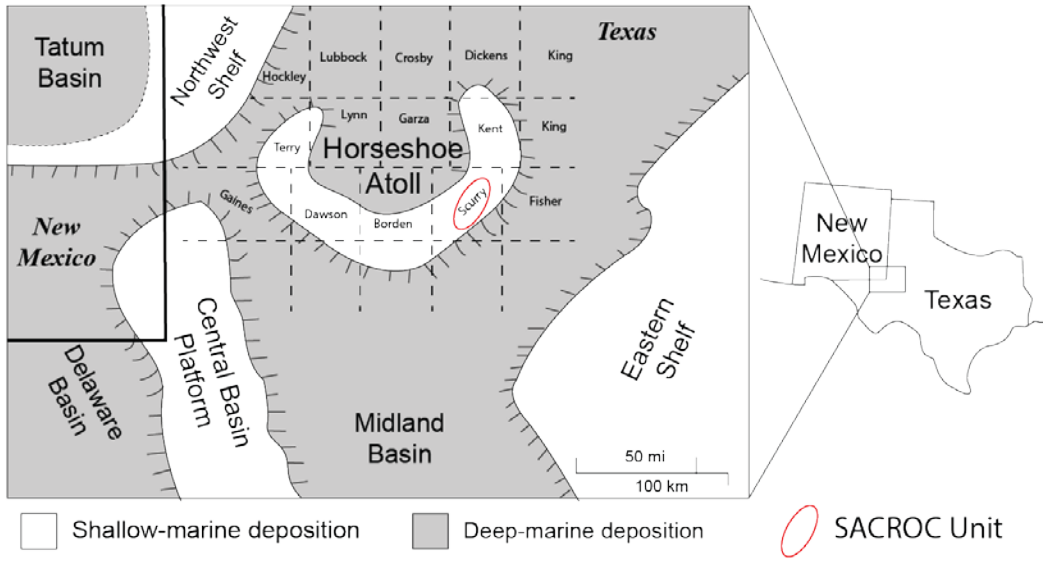


**Fig. 1.1**: Location map of the SACROC Field showing basins and other structural elements of the greater Permian Basin (modified from Saller et al., 1993). Bold lines are state boundaries and dashed lines are county lines with county name within.

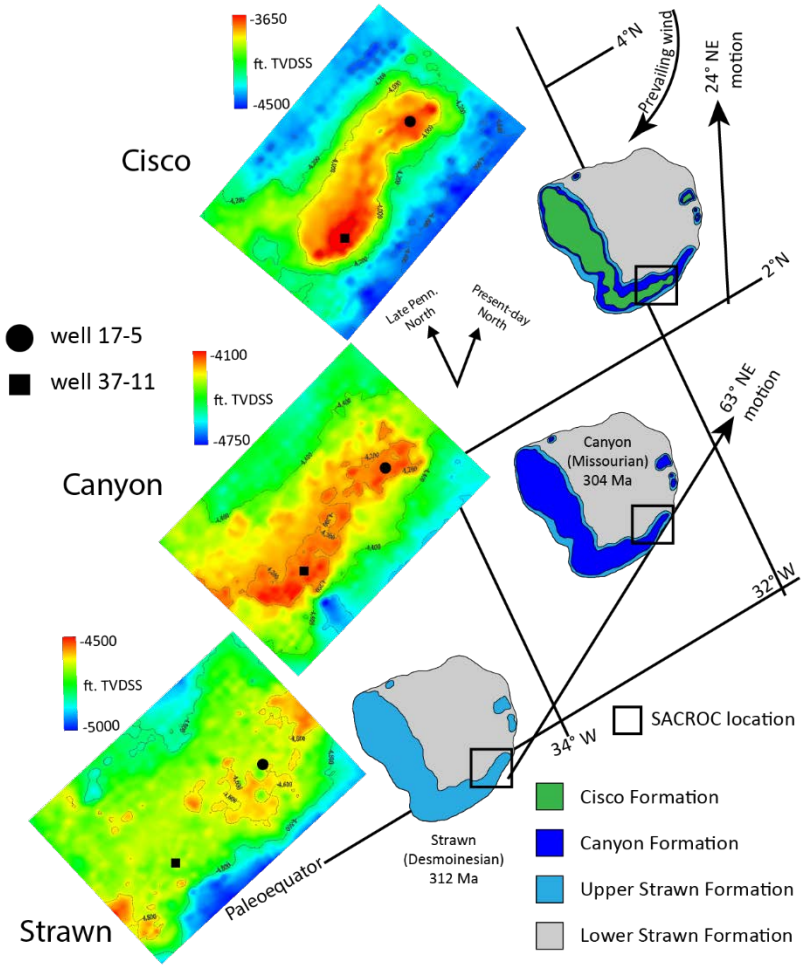


**Fig. 1.2**: Depositional and structural evolution of the SACROC platform during the Late Pennsylvanian. As the Horseshoe Atoll drifted northward (from Walker et al., 1995), the eastern margin (windward) of the SACROC platform experienced significant depositional relief growth during the deposition of the Canyon and Cisco formations giving rise to an east-west asymmetry of the SACROC platform. Bars indicate current structural depths true vertical depth subsea (TVDSS) measured in feet.

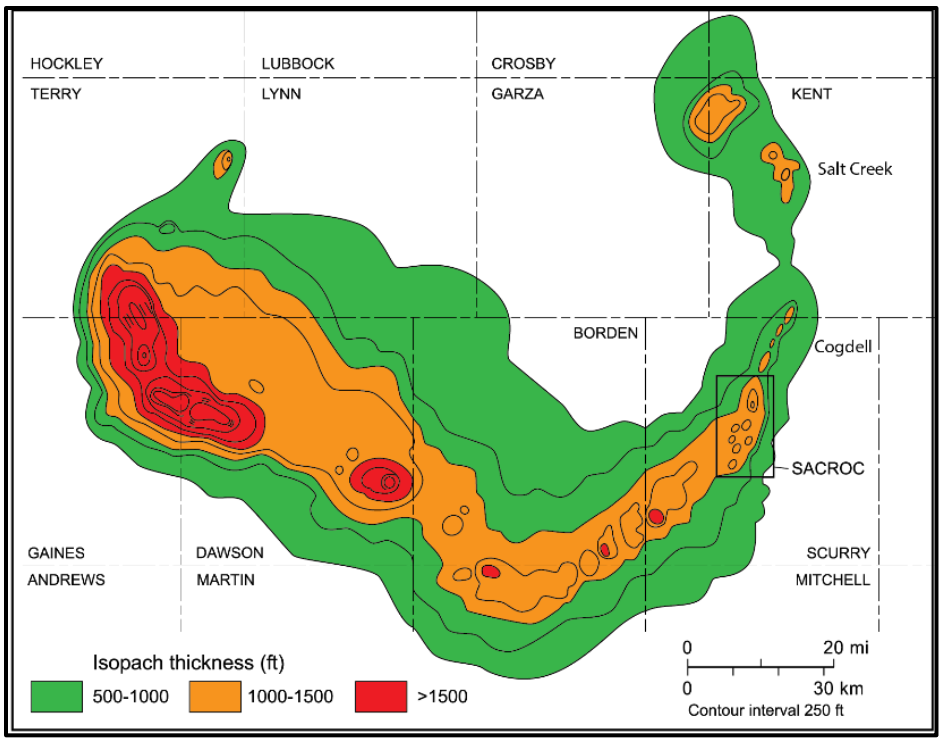


**Fig. 1.3**: Isopach map of Horseshoe Atoll carbonate. Modified from Galloway (1983) after Vest (1970).

There are several important studies of the Late Paleozoic carbonates in the Horseshoe Atoll. Earlier studies including Myers et al. (1956), Stafford (1959), Burnside (1959), and Vest (1970) focused primarily on regional biostratigraphy and the characterization of carbonate buildups. Schatzinger (1987) studied several fields on the eastern side of the Horseshoe Atoll including Kelly-Snyder (includes SACROC), Cogdell and Diamond M fields. His study documented depositional facies, facies lateral geometric relationships, and diagenetic history. He grouped the 27 depositional facies into three broad environments: tidal and peritdal, proximal, and distal. Tidal and peritidal consist primarily of lime mudstone that was restricted to structurally-high parts phylloid mounds in platform interior. Proximal facies comprised of ooid grainstones, phylloid boundstone, sponge-

algal-bryozoann mounds, and mound debris. Finally, distal facies includes open marine skeletal wackestone and packstone, basin-margin argillaceous mudstones, and black basinal shale. He used electric, gamma-ray, and neutron porosity logs to extend facies cross sections into area with limited and absent core control. He concluded that energy conditions were optimal on the eastern side of the Horseshoe Atoll allowing the phylloid boundstone to flourish. Schatzinger (1987) attributed cyclic sedimentation he documented on the eastern Horseshoe Atoll to pulsed subsidence. Meteoric diagenesis and early lithification at the top of each cycle especially at the windward side resulted in favorable relief. He noted that phylloid boundstone facing the windward side flourished compared to the leeward side. Wright (2011) compiled a general synthesis of the Late Pennsylvanian paleodepositional environments of the greater Permian Basin (Fig. 1.4).

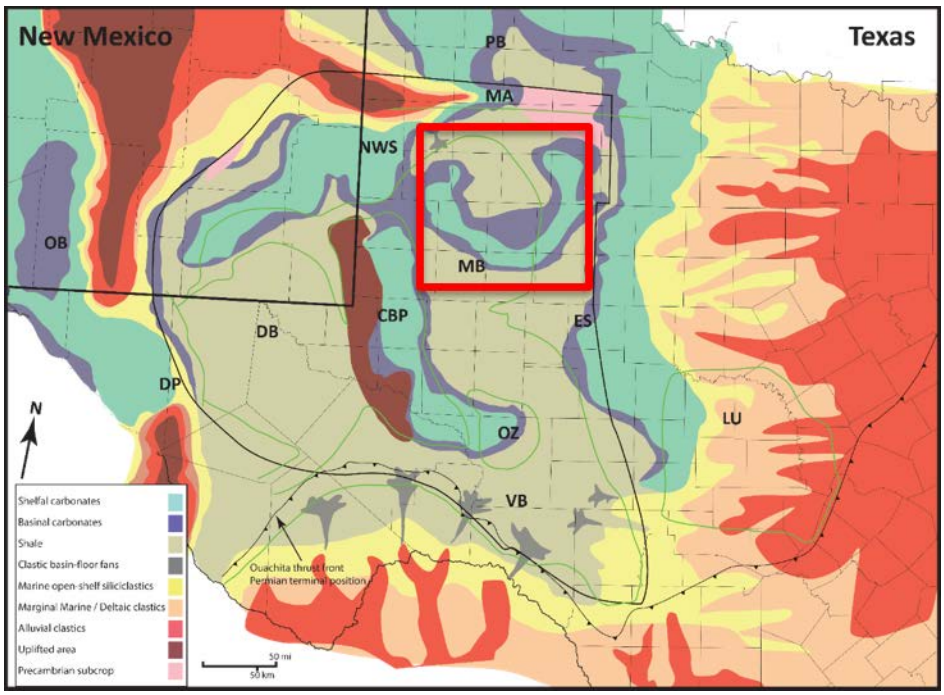


**Fig.1.4**: Map of the Late Pennsylvanian paleodepositional environments show the greater Permian basin (thin black line), which segmented into several basin and platforms. The study area is located on the eastern limb of the Horseshoe Atoll (red box) located at the northern portion of the Midland Basin. The bright colors are siliciclastics, the blue colors are carbonates, and the grey color is basinal shales.

This dissertation aims to resolve and add to the debated question of the nature of the LPIA (Fig. 1.5) by integrating sedimentology, sequence stratigraphy and providing a refined eustatic curve. In addition, it provides a good example how to build complex geological models by integrating geological understanding from modern and outcrop analogs with subsurface data. The data used from the SACROC Field include more than 7000 ft of core and 650 wireline logs providing a comprehensive stratigraphic record of the Late Carboniferous. The SACROC field is identified as an isolated carbonate platform of the greater Horseshoe Atoll (Galloway et al., 1983) that experienced a higher subsidence

rate compared to other regions of the greater Permian Basin, which resulted in the preservation of a thicker stratigraphic section.

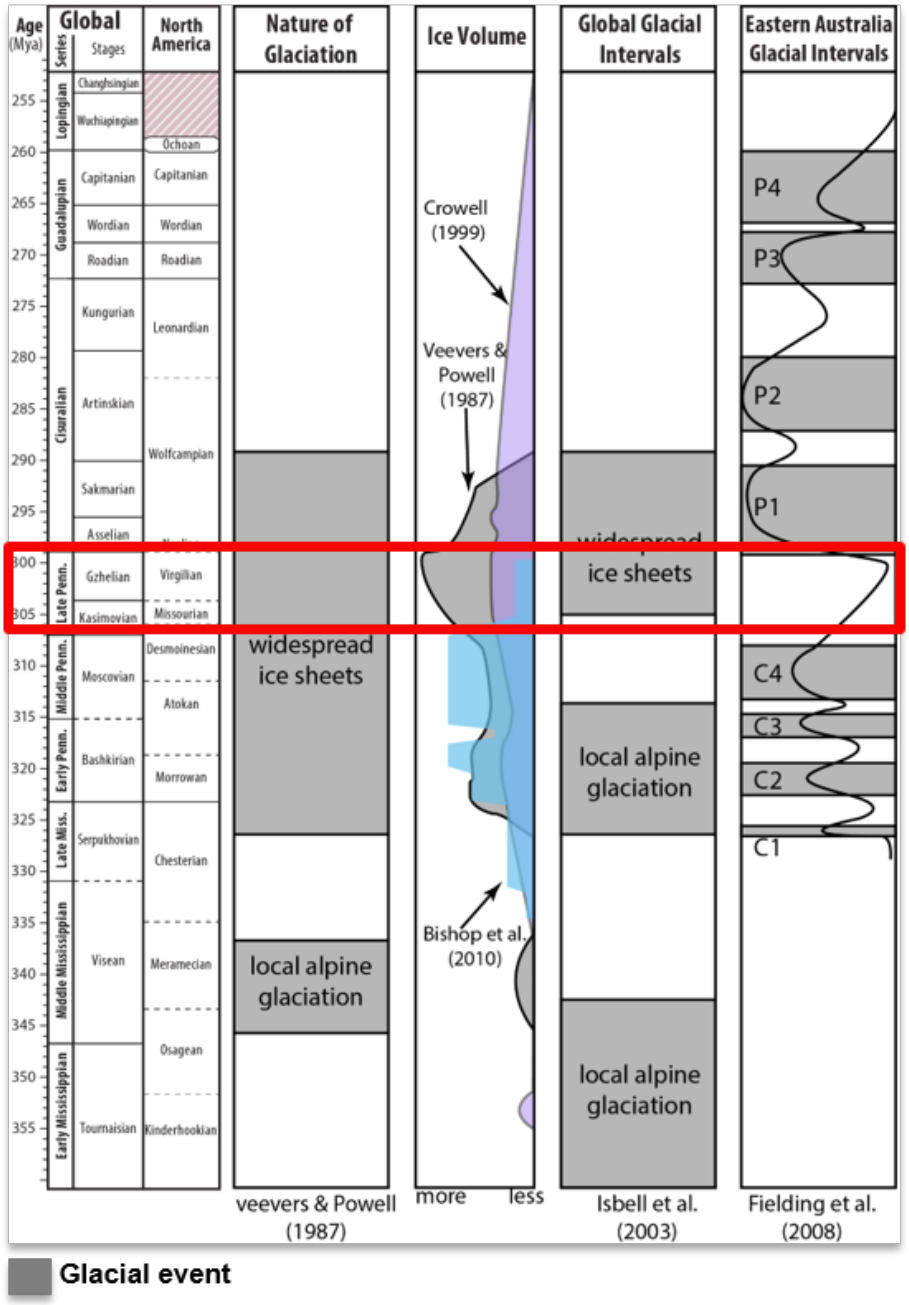


**Fig. 1.5**: Glacial events in Late Paleozoic from different studies. Controversial views recently challenged the long-held model of glaciated Late Pennsylvanian (modified from Fielding et al., 2008).

The second chapter of the dissertation provides a high-resolution sequence stratigraphic framework of the Missourian Canyon (306±1 Ma to 303.7 Ma) and the Virgilian Cisco (303.7 to 298.9±0.8 Ma) Formations based on lateral and vertical changes of depositional facies, their stacking patterns, and spatial distribution across the field. The stratigraphic picks are extended across the entire field with the aid of borehole wireline logs and structure maps generated from depth-converted 3D seismic.

The third chapter of the dissertation provides an improved eustatic curve for the Late Pennsylvanian. Detailed sedimentologic descriptions were used to infer eustatic changes based on variations in depositional lithofacies in response to waxing and waning of ice sheets. Each lithofacies is assigned an estimated water depth based on its texture, biota, and sedimentary structures and how it compares to modern and ancient analogs.

The fourth chapter of the dissertation compares several modeling methods for suitability of capturing facies heterogeneity in complex icehouse carbonate platforms. Several modeling methods were tested to examine their ability to produce sound geologic models. The best 3D facies model was then selected for petrophysical modeling of the reservoir properties.

# CHAPTER 2: STRATIGRAPHIC ARCHITECTURE AND PLATFORM GEOMETRY OF A LATE PENNSYLVANIAN ISOLATED CARBONATE PLATFORM: SACROC FIELD, HORSESHOE ATOLL, TEXAS


## ABSTRACT

The Late Pennsylvanian Scurry Area Canyon Reef Operators Committee (SACROC) field of the Horseshoe Atoll, Midland Basin, represents an isolated carbonate platform that developed during icehouse conditions. Icehouse periods are characterized by high-frequency, high-amplitude relative sea-level fluctuations under which highly complex and heterogeneous carbonate platforms develop. This study makes use of the exceptional dataset from the SACROC field including core and 3-D seismic data to document the characteristic style of stratigraphy and facies heterogeneity in this setting. First order patterns are distinct windward-leeward asymmetry with grainstone shoals focused on the present-day eastern margin. A distinct evolution from a more layer cake cycle pattern with strong porosity stratification into progressively backstepped and increasingly complex buildup-prone system reflects the transition into peak icehouse conditions in the latest Pennsylvanian. The Canyon consists of four aggradational, grainstone-capped high-frequency sequences each of which is composed of several transgressive-regressive high-frequency cycles that are highly correlatable across the platform top. The Cisco Formation is composed of five high-frequency sequences identified on the basis of 1-D sequence stratigraphic analysis. Correlations of these five sequences are made difficult by the high

lateral variability of the phylloid mounds, their flank facies, and heterogeneity caused by much of the unfilled accommodation as well as erosion during periods of subaerial exposure.

The extreme lateral and vertical heterogeneity captured within the high-resolution sequence stratigraphic framework illustrates its value with implications on the distribution and continuity of flow units controlled by original depositional fabrics. In addition, subaerial exposure events in some instances cause significant variability in porosity values across the same timeline which impede log-based correlation. Finally, the windward-leeward asymmetry documented in SACROC is inherent to isolated carbonate platforms as evidenced by its consistency with several modern and ancient examples.

## INTRODUCTION

Icehouse periods are characterized by high frequency, high-amplitude sea-level fluctuations driven by the waxing and waning of continental ice sheets (Wanless and Shepard., 1936; Crowell, 1978). High-amplitude glacioeustasy fundamentally impacts carbonate platform sequence stratigraphic architecture, resulting in a vertically and laterally heterogeneous stratigraphic record with multiple unconformities and meteoric vadose diagenetic patterns (Grotzinger, 1986; Read et al., 1991; Read, 1995). Vertical stacking pattern analysis of stratigraphic records is a fundamental tool for sequence stratigraphic interpretation (e.g., Goldhammer et al., 1990; Osleger and Read, 1991; Kerans and Fitchen, 1995; Lehrmann and Goldhammer 1999). The parameters of the one-dimensional stacking pattern analysis include lithofacies types, lithofacies proportions,

cycle thickness, cycle symmetry, and lithofacies tract offset (Kerans and Tinker, 1997). For example, in a vertical succession an increase of deep-water facies thickness at the expense of shallow-water facies implies a rise in sea level characterized by retrogradational stacking. These stratigraphic parameters are used to establish two- and three-dimensional sequence stratigraphic frameworks (e.g., Kerans, 1995; Tinker 1998; Janson et al. 2007).

Much of our understanding about icehouse isolated carbonate platform facies trends, geometry, and sequence stratigraphic architecture is documented from modern examples (Schlager and Chermak, 1979; Crevello and Schlager, 1980; Eberli and Ginsburg, 1989; Grammer and Ginsburg, 1992; Grammer et al., 1993; Wanless and Dravis, 2008; Harris and Vlaswinkel, 2008). Although these modern examples provide excellent analogs and predictive tools for ancient datasets, limited information is provided within their partially preserved stratigraphic record. Detailed outcrop studies of sequence stratigraphic architecture from isolated Phanerozoic carbonate platforms include the Upper Devonian Great Barrier Reef in the Canning Basin (Playford, 1980), the Middle Triassic Latemár of northern Italy (Egenhoff et al., 1999), and the Upper Cretaceous Apulian platform (Sanders, 1996). In addition, subsurface studies of isolated carbonate platforms, which host significant reserves of hydrocarbon, include Tengiz Field in Kazakhstan (Weber et al., 2003; Collins et al., 2006); Aneth and Ismay fields of the Paradox Basin in southeastern Utah and southwestern Colorado (Peterson, 1966), and the Natuna Field in Indonesia (Kraft and Sangree, 1982; Bachtel et al., 2004).

The Late Paleozoic SACROC Unit of the Horseshoe Atoll in West Texas represents an isolated carbonate platform that produced over 1 billion oil barrel total production from

the Strawn to Cisco (Hawkins et al., 1996). A wealth of data are available including core, wireline logs, and 3-D seismic at SACROC, which provide an opportunity to study the stratigraphic architecture and platform geometry of an ancient isolated carbonate platform that developed during peak icehouse conditions. In this study, depositional facies, their stacking patterns, and spatial distribution across the SACROC platform are described. Further, seismic data utilized in this study illustrate the evolution of the platform geometry and its windward-leeward asymmetry. Consequently, a refined understanding of the paleoenvironmental history, stratigraphic architecture, and platform geometry enhance predictions of reservoir quality and connectivity as well as allow for more accurate constraints on exploration prospects.

## GEOLOGIC SETTING

The Permian Basin (Texas, USA) was located between 5 and 10 degrees north of the equator during the Late Pennsylvanian (Witzke, 1990; Waite, 1993; Golonka, 2011). The assembly of Pangaea and the associated Ouachita Orogeny in the Late Paleozoic drove the reactivation of Precambrian faults, possibly related to the Grenvillian orogeny, and resulted in the, development of a series of basins and uplifts along high-angle reverse faults (Hills, 1984; Horak, 1985). In the latest Mississippian, dark grey and brown shale almost filled the Tobosa Basin, a 350-mile-wide depression between the Texas arch on the east and the Diablo arch on the west, which started to into smaller basins and platforms (Galley, 1958; Adams, 1965). Reactivation of zones of weakness and differential subsidence resulted in the development of smaller intracratonic basins including the Delaware and

Midland Basins, which were separated by the Central Basin Platform (Fig. 2.1) (Adams, 1965; Hills, 1984; Kluth, 1986). Vest (1970) reported that restoration of isopachous maps of pre-Strawn rocks outline a broad, low-relief ancestral platform onto which the Horseshoe Atoll developed. This platform was dipping to the west and southwest with a topographic relief that was between 15 m and 46 m allowing carbonate deposits to accumulate (Vest, 1970).

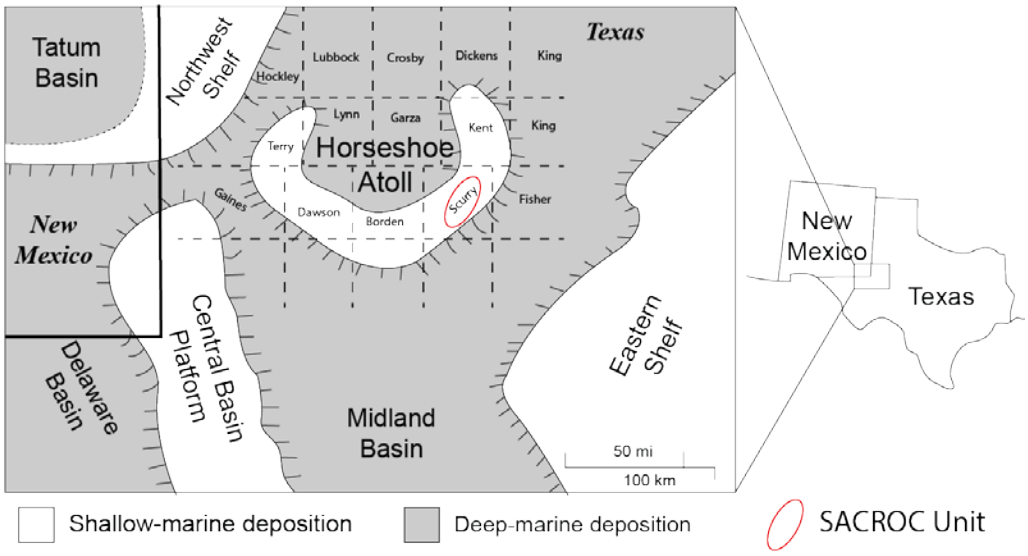


**Fig. 2.1**: Location map of the study area (SACROC) showing the basins and structural elements of the Permian Basin (modified from Saller et al., 1993). Bold lines are state boundaries and dashed lines are county lines with county names within.

The Horseshoe Atoll is situated in the northern portion of the Midland Basin. The Midland Basin is surrounded by the Matador arch to the north, Ozona arch and Ouachita–Marathon fold belt to the south, Eastern Shelf to the east, and Central Basin Platform to the

west (Fig. 2.1). During the Late Pennsylvanian, the Ouachita Orogeny caused the northeast rotation and drifting of the Horseshoe Atoll. The atoll drifted from an equatorial position during the deposition of the Missourian Canyon Formation to 4°N during the deposition of the Virgilian Cisco Formation with an overall rotation of 43° to the northeast from its current alignment (Walker et al., 1995).

The Missourian Canyon and the Virgilian Cisco formations described in this paper were deposited on an isolated carbonate platform located on the eastern limb of the Horseshoe Atoll of the Midland Basin (Fig. 2.2). Underlying Strawn platform carbonates have a uniform thickness, ranging between 70 and 85 meters, and consist of algal wackestones, crinoid wackestones/packstones, algal bioclastic grainstones, and crinoidal bryozoan wackestones (Wright, 2011). In the Midland Basin, the top of the Strawn Formation is a sequence boundary marked by a facies offset of grainstones and packstones onto which transgressive wackestones of the Canyon were deposited (Waite, 1993). Similarly, in the neighboring Central Basin Platform, a subaerial exposure separates ooid grainstone at the top of the Strawn Formation from spiculitic mudstone at the base of the succeeding Canyon Formation. The subaerial exposure is indicated by the negative shift of $\delta^{13}C$ and $\delta^{18}O$ in exposed carbonates, heavier $\delta^{18}O$ of unaltered carbonates, and abundant meteoric diagenetic fabrics (Saller et al., 1999).

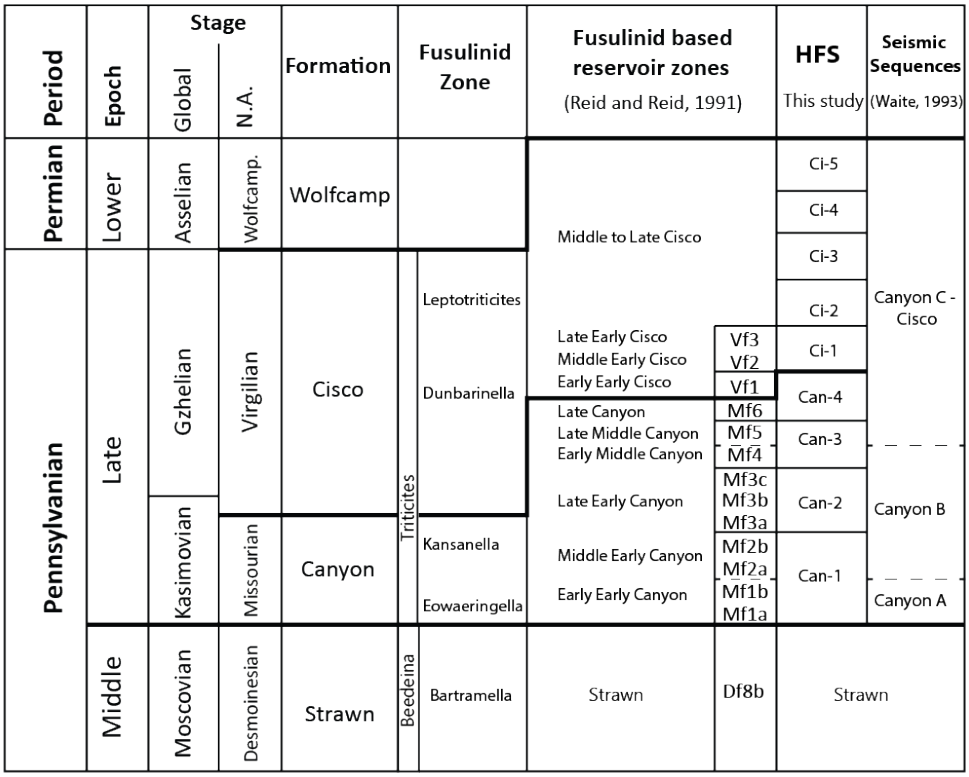


**Fig. 2.2**: A generalized stratigraphic column of West Texas with Global and North American (N.A.) stages. The fusulinid biostratigraphy from SACROC (Schatzinger, 1988) correlated with reservoir zones and ages for the succession from the base of the Canyon Formation to the top of the Cisco Formation in Cogdell Field (Reid and Reid, 1991) and with regional seismic sequences (Waite, 1993). In this study, the succession is divided into nine high-frequency sequences (HFS) in the SACROC field.

The Canyon Formation is divided into four high-frequency sequences that are further subdivided into seven high-frequency cycles (Reid and Reid, 1991; Waite, 1993). The Cisco Formation is divided into five high-frequency sequences (Kerans, 2001) with six

fusulinid biozones (Reid and Reid, 1991). The Cisco Formation is characterized by highly complex architectural variability as a result of increased eustatic amplitude (Heckel, 1977; Goldstein, 1988; Feldman et al., 2005; Alnazghah and Kerans, 2018) and unfilled accommodation space (Eberli and Grammer, 1999; Janson and Kerans, 2007; Eberli, 2013). Overlying the Cisco Formation is the Wolfcamp Group of the Lower Permian which consists mainly of shale deposits except for the western limb of Horseshoe Atoll where carbonate deposits persisted before the Horseshoe Atoll drowned (Vest, 1970). The carbonate factory on the eastern atoll was probably shut off by siliciclastic contamination sourced from the Eastern Shelf (Wright, 2011).

## METHODS

Standard carbonate description sheet was used to characterize the eleven cored wells (+7000 ft) (Fig. 2.3) used in this study (in Appendix). The depositional facies documented using Dunham Classification (1962) and were modified where appropriate by Embry and Klovan (1971). The description sheet is designed to capture natural fractures, stylolites, mineralogy, visual porosity, sedimentary structures, textures, and grain size and type. Cored wells were examined using a binocular microscope, where core slabs were examined dry and water wet. Hydrochloric acid (10-20% concentration) is used to itch core surface where needed to allow and to enhance visual examination. Thin sections were used, where available, to refine facies description from core and to better asses porosity estimate, pore type and to record diagenetic overprint. This is followed by one-dimensional stratigraphic analysis where vertical succession is broken down into several depositional cycles where conformable depositional facies result in response to allogenic controls.

Depths of the cored wells are based on driller's depth which may be different from borehole wireline logs depths. Core-to-log shift is a process where driller's depth of cores is corrected to borehole depths of the logs. Mismatch can be detected using neutron porosity, bulk density and gamma ray logs. For example, porous ooid grainstone may be detected in neutron porosity, whereas a gamma ray kick can detect siliciclastic shale.

Stratigraphic picks based on core and logs were extrapolated across the field to all uncored wells, establishing the stratigraphic framework of the Late Pennsylvanian of the SACROC Field.

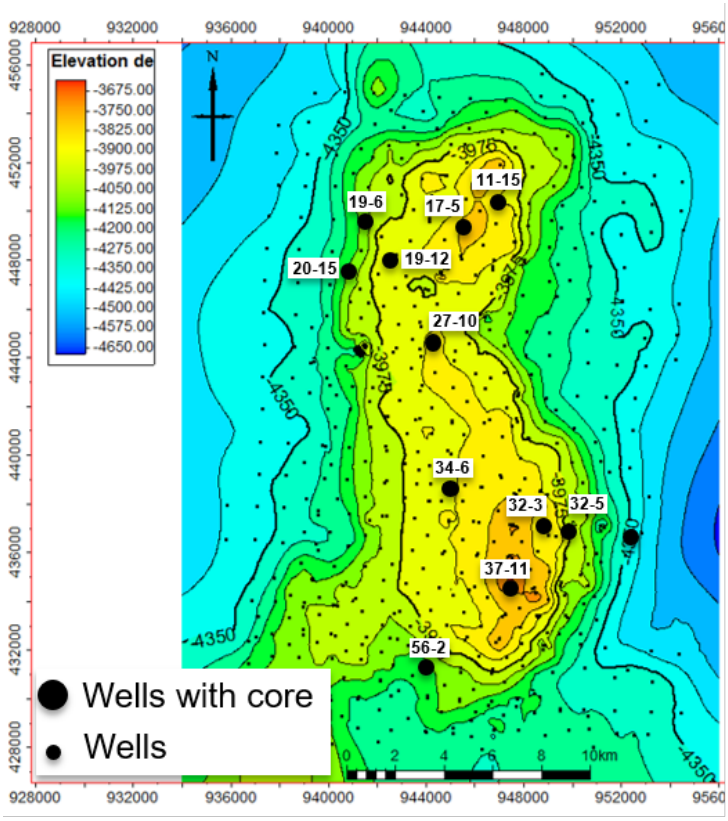


**Fig. 2.3**: Map of the top Cisco structure with the location of cored wells and wells with wireline logs.

## LITHOFACIES AND DEPOSITIONAL ENVIRONMENTS

The Missourian Canyon and the Virgilian Cisco formations can be characterized by ten lithofacies based on lithologies, textures, sedimentary structures, and main grain types. Lithofacies types were mainly differentiated by sedimentary structures and dominant skeletal versus non-skeletal grains. These lithofacies types are grouped into five facies associations, which combined lithofacies of similar characteristics and were related to broader depositional environments (Fig. 2.4).

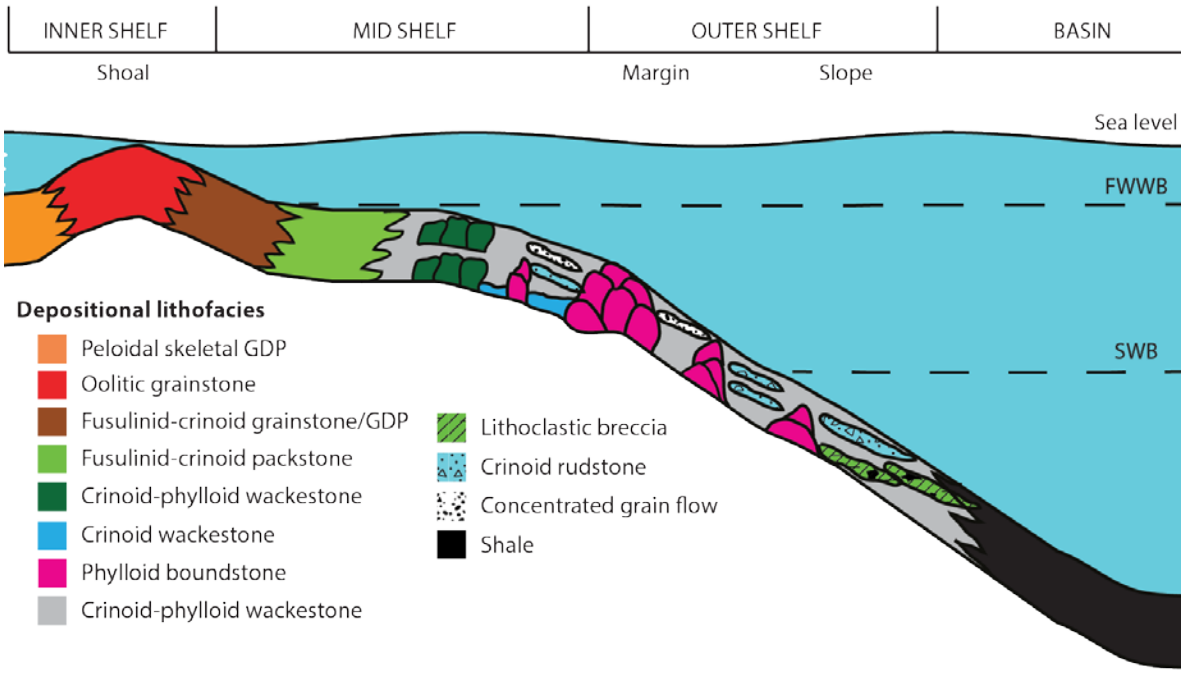


**Fig. 2.4**: Ideal depositional model for the Late Pennsylvanian carbonates in the SACROC field. GDP=grain-dominated packstone.

## Basin Facies Association

### *Shale*

Shale, in general, is not very well preserved and ranges in thickness from a few centimeters to 1.5 meters. This facies occurs as finely-laminated, dark grey to black fissile siliciclastics that interfinger up-dip with crinoid rudstones. Laminations are sometimes disrupted by unlined, rarely branching *Planolites* burrows. Shale units have sharp bases that commonly grade upwards into more carbonate-rich shales followed by pure carbonates. Bioclasts in shale are rare reworked brachiopods and crinoids. To identify shale-rich intervals in wells, high gamma-ray responses in logs were used (Fig. 2.5)

### *Interpretation*

The absence of diverse biota and the limited burrowing activity together indicate low energy, dysaerobic, sediment-starved depositional environment (Mullins, 1983), which is established either in a basin margin setting and/or during high accommodation phases on the shelf associated with significant sea level rises and platform drowning.

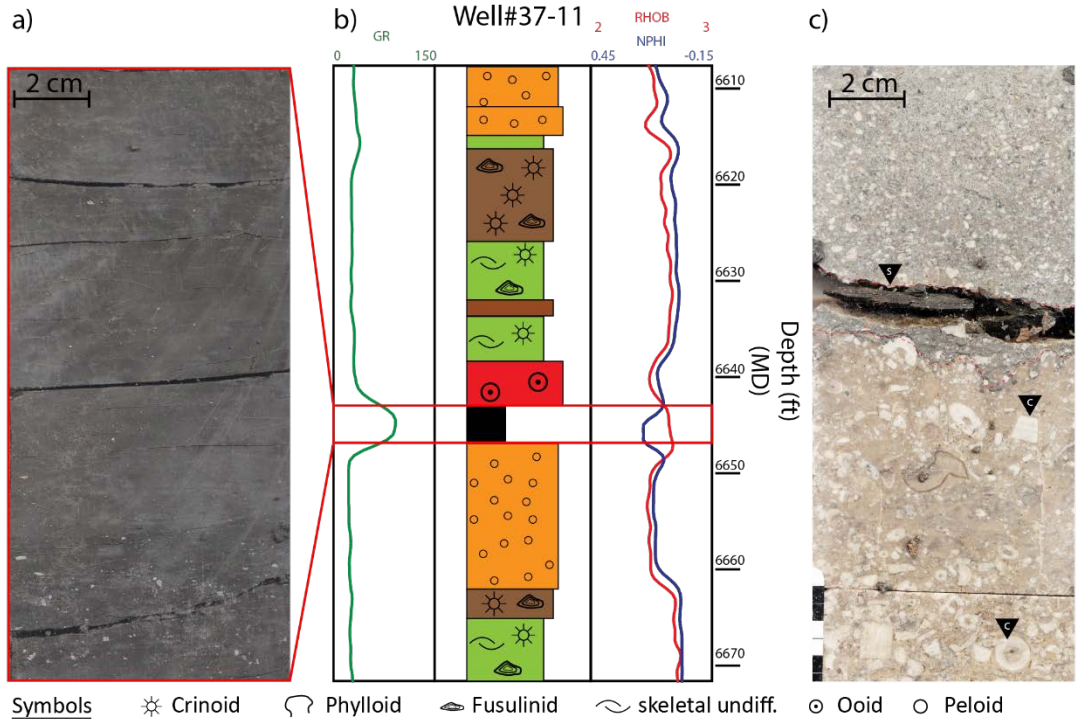


**Fig. 2.5**: Black shale of the basin facies association. a) Core image of shale and b) gamma-ray log (GR) showing an increased response to the shale interval and a crossing between neutron porosity (NPHI) and bulk density (RHOB) logs from well # 37-11 c) Core image showing poorly preserved shale (triangle with s) between crinoid floatstone and skeletal grainstone slope deposits. Triangle with "C" indicate crinoid grain. Facies colors are the same as in Fig. 2.4.

## Slope Facies Association

The slope facies association includes three facies: skeletal grainstone, crinoid rudstone, and lithoclastic breccia.

### *Skeletal grainstone*

Skeletal grainstones are composed of a mixture of skeletal and non-skeletal allochems. Crinoid debris, fusulinids, and phylloid algal plate fragments are the main skeletal allochems, with minor assemblages of bryozoans, agglutinated foraminifera, and sponge spicules. Non-skeletal grains are predominantly peloids (up to 30%). Although the lower and upper contacts of this lithofacies association are sharp, the lower contact can either be planar or display load-deformed marks. The grainstones are moderate- to poorly-sorted with a grain size that ranges from fine- to coarse-grained and shows no grading. Some of the coarser grains are imbricated to roughly 20-40 degrees (Fig. 2.6A & 2.6B).

### *Crinoid rudstone*

Crinoid rudstones are observed in wells located along platform's margin, and control points (cored wells) show an increasing abundance of these facies starting from late Missourian upwards into the late Virgilian prior to the drowning of the platform. The rudstones consist mainly of crinoid columnals with accessory fusulinids, phylloid algal fragments, bryozoans, brachiopods, agglutinated foraminifera, bivalves and minor phylloid algal boundstone intraclasts. The matrix of the rudstone is mainly carbonate mud. Large crinoid grains can be matrix supported as crinoid floatstones (*sensu* Embry and Klovan,

1971). Grain size ranges from a fine-grained muddy matrix to granule-sized columnals. In several cases, the lower contact is scoured with large intraclasts at the base that may show normal grading (Fig. 2.6C & 2.6D).

***Lithoclastic breccia***

Lithoclastic breccias are typically composed angular and subangular clasts (Fig. 2.6E & 2.6F) forming intervals up to several meters in thickness. Clasts are composed of phylloid crinoid wackestones, phylloid boundstones, fusulinid-crinoid packstones, and fusulinid-crinoid grainstones. Clasts may show coarse-tail normal grading of clasts grain size suggestive of sediment gravity flows. Individual breccia units range in thickness from 60 cm to 3.5 m.

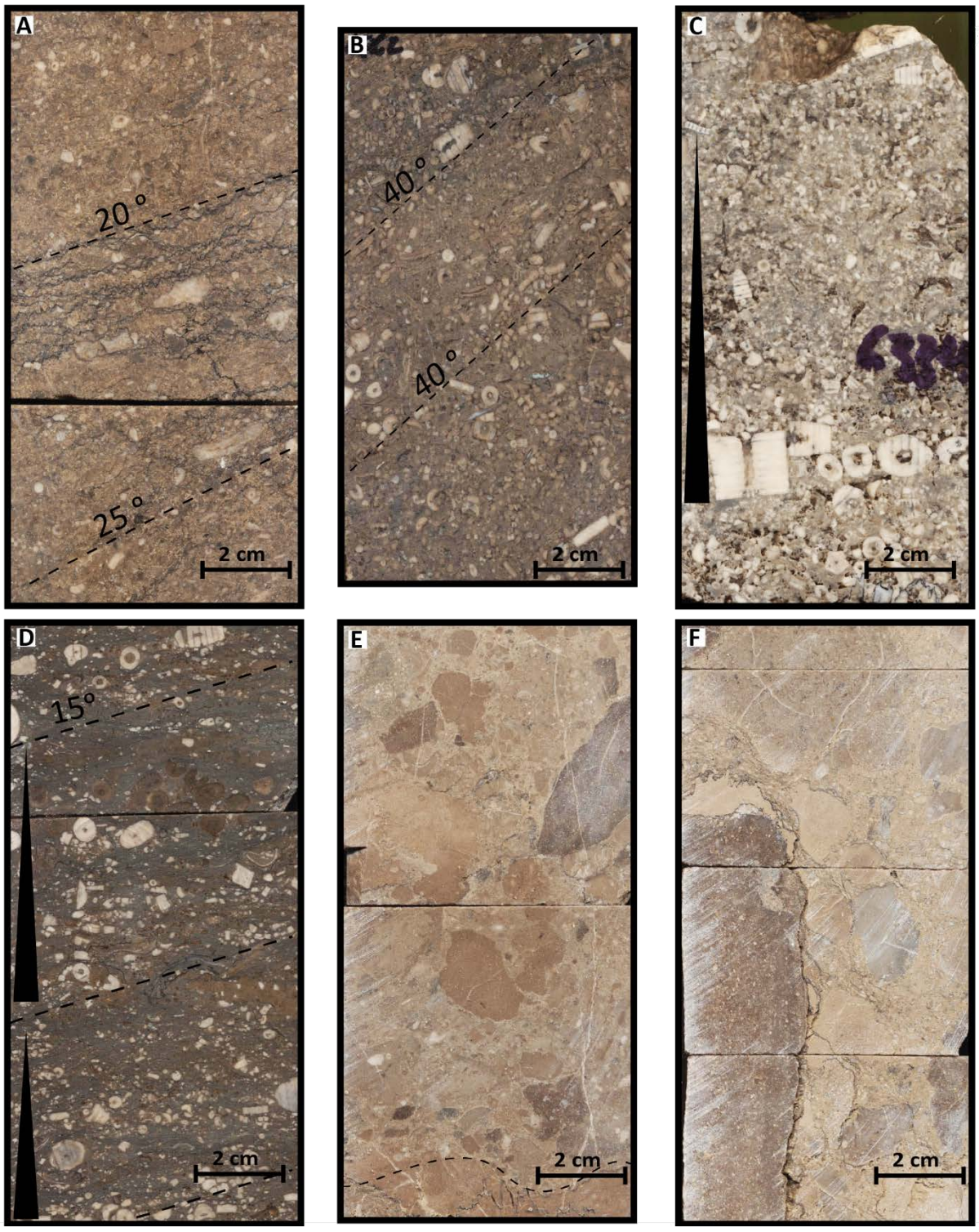
A
20°
25°
2 cm
B
40°
40°
2 cm
C
2 cm
D
15°
2 cm
E
2 cm
F
2 cm

**Fig. 2.6**: Core slab photographs of typical slope facies associations. A) & B) Concentrated density flows at platform edge with steep depositional dips increasing with coarser texture. C) Crinoid rudstone and D) crinoid floatstone showing normal grading indicated by upside-down triangles. E) & F) Platform- and mound-derived lithoclastic breccias; larger blocks of breccias are not be visible within the width of the core.

***Interpretation***

Considered collectively, the lithofacies of the slope facies association fit well with the classic model for isolated carbonate platform slope deposits (Read, 1985). The chaotic, normally graded lithoclastic breccias are interpreted to represent debris flow deposits triggered because of gravitational collapse of the oversteepened margin. Playton et al. (2010) documented similar sedimentologic characteristics of carbonate slopes of similar systems. Crinoid rudstones are interpreted to represent proximal slope turbidites indicated by the scoured bases and normal grading (Coniglio and Dix, 1992). The skeletal grainstones show large, parallel clasts that are imbricated along the dipping surfaces indicative of down-dip flow. Sharp and inclined contacts, with no apparent grading, suggest that these grainstones represent concentrated density flow deposits (*sensu* Mulder and Alexander, 2001). These deposits are consistent with slope deposits in which increased abundance of grain-dominated deposits strongly supports increased slope angles as result of increased angles of repose (Kenter, 1990).

## Mound facies association

Lenticular mounds (bioherms (*sensu* Cumings, 1932) and their flank facies (Fig. 2.7) characterize this facies association. The core of the mounds is represented by phylloid algal boundstone/floatstones, whereas the flanks are made up of crinoid phylloid wackestones.

### *Phylloid algal boundstone*

A mud-rich matrix characterizes the phylloid algal boundstone facies with abundant, poorly-preserved, calcite-replaced, cup-shaped and plate-like phylloid algae associated with stromatactis (Fig. 2.8A). Although the phylloid algal boundstone is dominated by phylloid algae, crinoids are common. Further, the boundstone may display limited biodiversity including fenestrate bryozoans, brachiopods, fusulinids, solitary rugose corals, and stromatoporoids. Phylloid algal boundstones tend to form vertically stacked bioherms with a thickness range between 2 and 25 meters (Fig. 2.11) with uncertain widths.

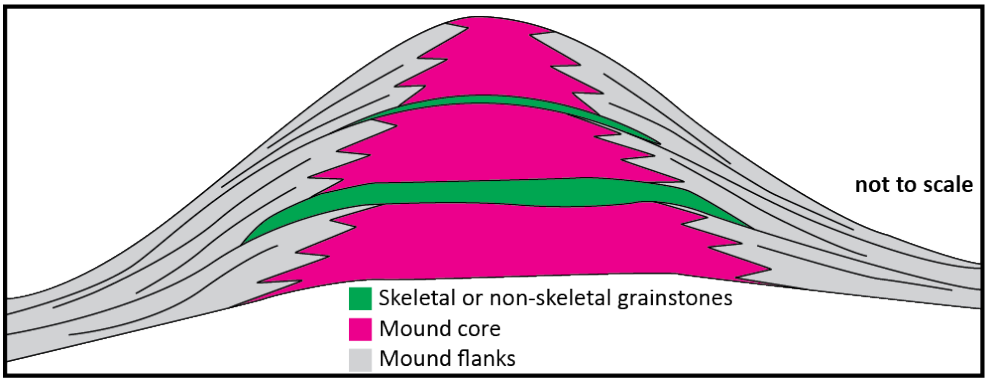


**Fig. 2.7**: Phylloid mounds typically grow upward producing convex up accumulations. Mound flanks are debris aprons derived from the main mound framework. Mound size is progressively reduced to catch up with long-term sea-level rise before giving up and drowning during the upper most Cisco Formation.

***Crinoid-phylloid wackestone/packstone***

The phylloid mound flank facies varies in texture from wackestone to packstone. This facies is mainly composed of complete and fragmented crinoid ossicles and dispersed phylloid algal plates (Fig. 2.8B). Crinoids range in size from medium-grained to granule-sized, within an often bioturbated matrix. Other accessory skeletal grains include sponge spicules, foraminifera, and disarticulated bivalves.

***Interpretation***

The presence of phylloid algae indicates growth within the photic zone down to water depths of about 130 meters (DeLong et al., 2006). *Eugonophyllum*, a genus of phylloid algae identified in the phylloid algal bioherms (Schatzinger, 1983), has been

related to modern green algae *Halimeda* and *Udotea* (Kirkland et al., 1993) which can grow in water depths up to 150 m (Freile et al., 1995). Abundance of phylloid algae and crinoids suggests open marine settings between a fair-weather wave base and storm wave base on Paleozoic platforms (Wahlman, 2002; Wahlman et al., 2013; James and Jones, 2015).

Texture is used as an important indicator of the amount of energy in the depositional system. While grain-dominated fabrics and fragmental phylloid algal plate textures reflect higher energy levels, the crinoid phylloid wackestone is consistent with quiet energy conditions (Dunham, 1962). However, disarticulated crinoids suggest that these quiet, muddy settings were interrupted by storm events, remobilizing crinoid debris, which were buried slowly. The lee side of phylloid algal bioherms are areas where quieter conditions existed, suitable for the deposition of wackestones (Fig. 2.8B, 2.8C) (Gischler, 1995; Smithers and Larcombe, 2003).

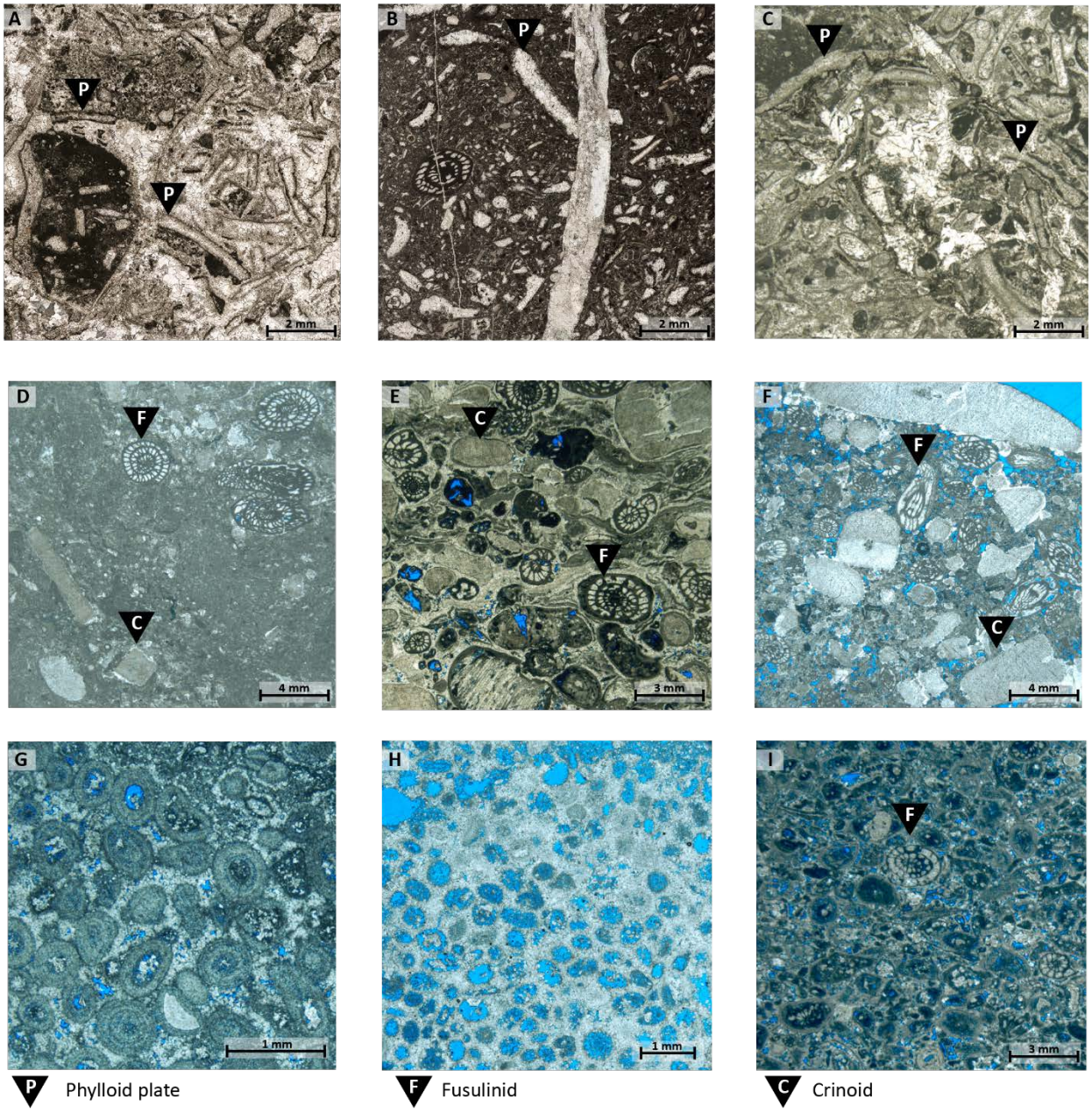
A
P
P
2 mm
B
P
2 mm
C
P
P
2 mm
D
F
C
4 mm
E
C
F
3 mm
F
F
C
4 mm
G
1 mm
H
1 mm
I
F
3 mm
P Phylloid plate
F Fusulinid
C Crinoid

**Fig. 2.8**: Photomicrographs of depositional facies, all images taken in plane polarized light. A) Phylloid boundstone (mound core), B) phylloid wackestone (flank-leeward side), C) phylloid packstone (flank - windward side), D) fusulinid-crinoid wackestone, E) & F) fusulinid-crinoid grainstone, G) ooid grainstone, H) moldic ooid grainstone, and I) peloid-skeletal grainstones. Triangles with letter refer to the following: “P” are phylloids, “F” are fusulinids, and “C” are crinoids.

The crinoid-phylloid packstones are the predominant facies of the phylloid mound flanks. Most of the grains of the packstone are broken, and much of the bioturbated matrix consists of peloids. This indicates low- to-moderate energy conditions related to shoaling and reaching a hydrodynamic threshold above which the optimum growth conditions of phylloid algal mounds are absent. Upward growth towards fair-weather wave base is associated with increased energy where the top of the phylloid mounds were "shaved" and abraded by wave action (James et al., 1994; 2001). The resulting debris aprons deposited at the periphery of the mound as flank facies (Fig. 2.7) and/or at intermound areas referred to as “algal meadows” (Orme et al., 1978; Drew and Abel, 1985).

**Middle shelf facies association**

This facies association is represented by subtidal, open marine carbonate lithofacies somewhat shallower than the ones developed around the shelf margin. The deposition of fusulinid-crinoid packstone/wackestone and grainstone is mostly restricted to the middle

shelf area where these facies are interpreted to be deposited in normal marine conditions under moderate to high-energy conditions.

***Fusulinid-crinoid packstone/wackestone***

The fusulinid-crinoid packstone/wackestone facies is composed of primarily disarticulated crinoids and large fusulinid tests (Fig. 2.8D). Other allochems include brachiopods, agglutinated foraminifera, peloids, and grapestone grains. While grains range from fine-grained to granule-sized, most grains are medium-grained with moderate sorting.

***Fusulinid-crinoid grainstone***

Fusulinid-crinoid packstones commonly grade upward into crinoid-fusulinid grainstones with an aggradational interface. This facies shows cross-stratification and parallel laminations that may be obliterated and obscured by bioturbation. Abundant crinoid ossicles, common fusulinids, and lesser agglutinated foraminifera characterize this moderately- to well-sorted, coarse- to very coarse grainstone (Fig. 2.8E, 2.8F).

***Interpretation***

The sparsity of fine-grained material in the crinoid grainstone is interpreted to represent a high-energy environment. During periods of high wave agitation, carbonate mud was winnowed away along with some other fine materials, which resulted in the deposition of intervals of massive fusulinid-crinoid grainstone with no observable stratification. High-energy, wave-influenced conditions are unlikely to have been maintained over vast distances and/or with increasing water depths. Thus, fusulinid-crinoid

packstones are interpreted to represent a lower-energy subtidal setting in contrast to grainstone textures. Further, crinoids tolerate a range of water temperatures but are restricted to normal marine salinities (James and Jones, 2015; Flügel, 2004). Hence, the environment of deposition is likely an open middle shelf near and below fair-weather wave base.

### Shoal Facies Association

The shoal facies association includes two facies: ooid grainstone and peloid-skeletal grainstone.

#### *Ooid grainstone*

Ooid grainstone is composed of well-sorted, fine- to medium-grained, coated grains and ooids with mostly bioclastic nuclei (Fig. 2.8G). Other non-skeletal constituents include peloids and superficial ooids, whereas accessory skeletal components include crinoids, bivalves, and gastropods. Ooid grainstones display low angle planar cross-stratification with limited to no bioturbation. During periods of sea-level lowstands, exposure of ooid grainstones promotes the development of moldic ooid grainstones (Fig. 2.8H) and/or caliche crusts.

#### *Peloid-skeletal grainstone*

Peloid-skeletal grainstones and grain-dominated packstones are characterized by skeletal allochems and abundant peloids with moderate sorting and fine- to medium-grain size (Fig. 2.8I). Common skeletal grains include crinoids and agglutinated foraminifera;

rare occurrences of bivalves and phylloid algal plates are observed. Sedimentary structures include low-angle lamination and minor bioturbation.

### *Interpretation*

Using modern carbonate depositional environments as an analogue, aragonitic ooids form in strongly agitated, current-swept, warm and shallow waters (< 5 m) at normal salinity condition (Loreau and Purser, 1973). On this basis, the well-winnowed, stratified oolitic grainstones at SACROC are interpreted to represent shoal facies that may have built to sea level.

The peloid-skeletal grainstone represents sediments that were deposited in relatively low- to moderate-energy conditions and were lithified early (Tucker and Wright, 2009). Grainstone texture, close association with ooid grainstones, low faunal diversity compared to fusulinid-crinoid grainstones, and low-angle lamination suggest a semi-protected, back-shoal depositional setting (Morin et al., 1994).

## CYCLE DEVELOPMENT AND STACKING PATTERNS

Sequence stratigraphic analysis revealed several diagnostic cycle stacking patterns that were used to infer the lateral juxtaposition of depositional facies as well as to track patterns of accommodation change. The depositional facies occur in repeated asymmetrical, upward shallowing hemicycles, commonly with abrupt facies offset at the top highlighted in many cores by deposition of deeper, subtidal facies overlying common subaerial exposure surfaces (Fig. 2.9). The vertical facies succession that makes up each

cycle is dependent on the stratigraphic age and depositional location within the platform (i.e., windward, leeward, flanks) as well as the magnitude of the eustatic signal at the time of the deposition. A summary of idealized cycle-stacking patterns for the Canyon and the Cisco formations from platform top settings is shown in figure 2.9. Establishing stacking patterns for the slope succession would require substantially more data than currently available. On the platform, cycles are capped by crinoid fusulinid grainstones/packstones, or oolitic grainstones. In these cycles, the flooding facies are variable with deeper facies at the flanks and relatively shallower facies in crestal areas. Additionally, flooding facies occurring along the windward flank tend to be higher energy deposits than those of the leeward margin. Overall, the succession of cycles in the Canyon Formation shows a progressive upward shallowing trend, whereas the Cisco Formation succession shows a progressive upward deepening trend.

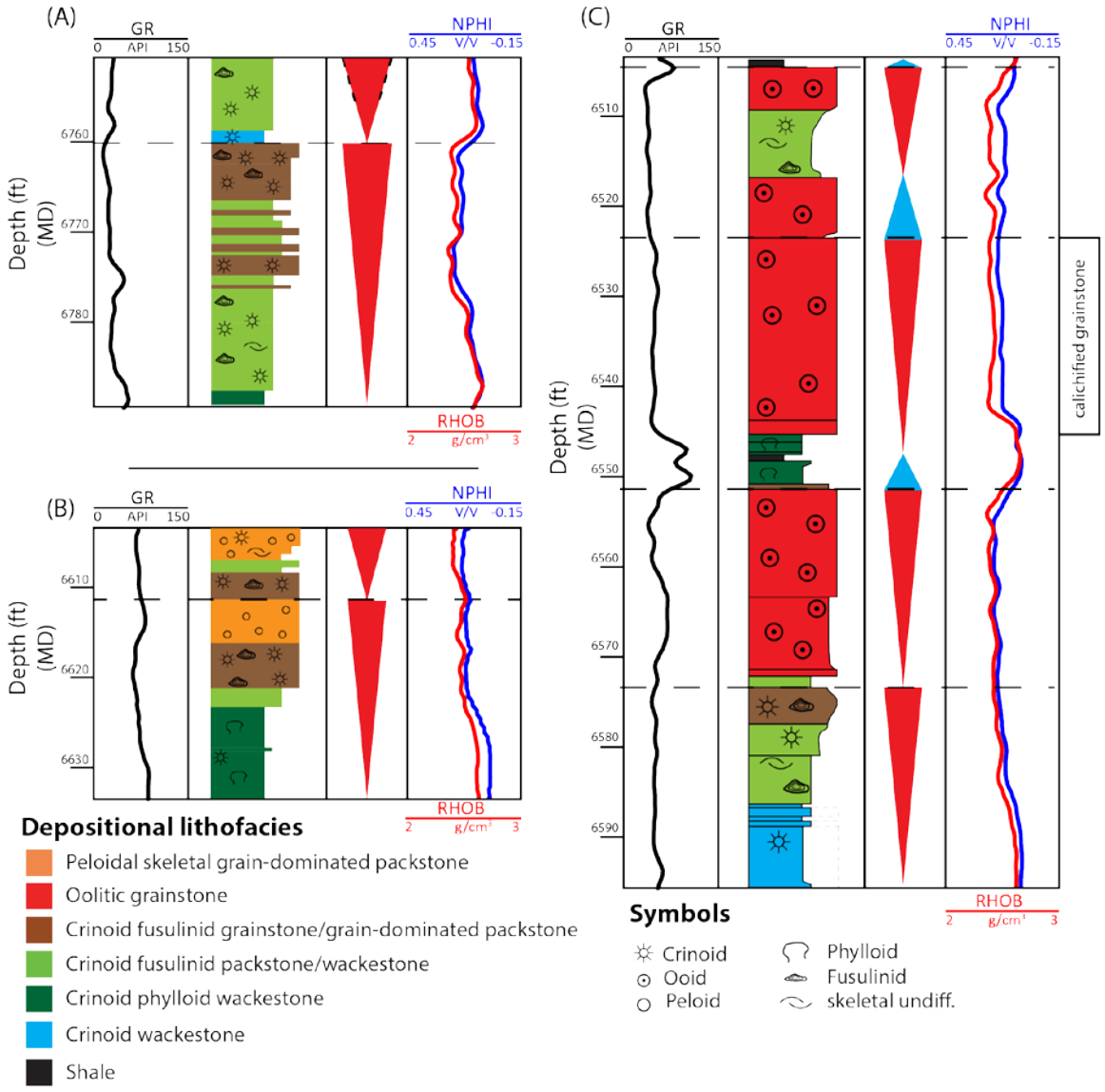


**Fig. 2.9**: One-dimensional facies stacking patterns of high-frequency cycles with different depositional facies of the Late Pennsylvanian from well 37-11. Wireline logs used are gamma ray (GR), bulk density (RHOB) and neutron porosity (NPHI). (A) Crinoid-fusulinid grainstone capped cycle. (B) Skeletal grainstone/grain-dominated packstone capped cycles. (C) Stacked shallowing upward cycles starting at the base with crinoid fusulinid capped cycles, followed by oolitic grainstone capped cycles that show exposure features up section. All measured depth (MD) in feet.

The vertical facies succession composing each cycle is dependent on the stratigraphic and geographic position of the observed strata within the platform as well as the strength of the eustatic signal at the time of the deposition. A summary of idealized of cycle-stacking patterns for the Canyon and the Cisco is shown in figure 2.10. We divided the cycles stacking pattern by formation and by the cycle position on the platform i.e. leeward, windward and crestal. The short-term high-frequency cycles are generally shallowing upward cyles capped by phylloid algal boundstone, crinoid fusulinid grainstone, or oolitic grainstone. The flooding facies of these cycles is variable with deeper facies at the flanks and relatively shallower facies at crestal areas. Nonetheless, significant transgression are episode are still recorded where basinal shale is brought onto the shelf crest. The flooding facies of the windward margin tend to be higher energy deposits than those of the leeward side. Overall, the long-term signal shows a progressive shallowing trend throughout the Canyon Formation, whereas the long term signal suggest an overall deepening. These signals influenced the architectural style of both the Canyon and Cisco Formations.

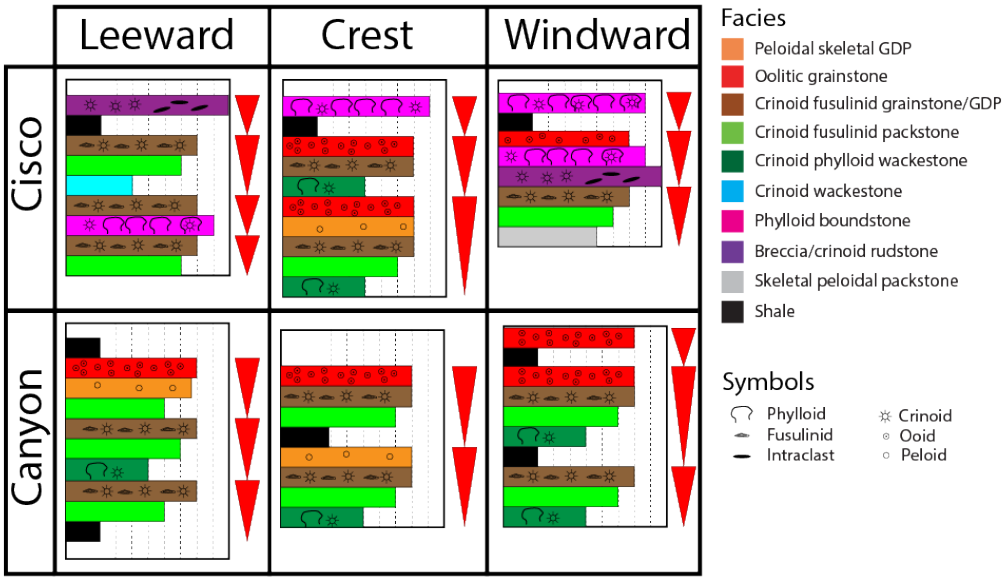


**Fig. 2.10**: A catalog of 1-dimensional facies stacking architecture of high-frequency cycles of the Late Pennsylvanian as observed in the SACROC Field. The catalog represents the most common shallowing-upward cycle trends for each formation and categorized by geographic location on the platform.

## SEQUENCE STRATIGRAPHY

The Pennsylvanian section of the SACROC field represents an isolated carbonate platform that consists of cyclic carbonates (Schatzinger, 1983; Waite, 1993; Kerans, 2001; Wright, 2011). High-frequency cycles are fundamental building blocks of high-frequency sequences defined by the upper and lower bounding surfaces of genetically related strata. Sequence boundaries are defined by maximum flood events indicated by a facies offset or by the development of subaerial exposure surface. The Late Pennsylvanian succession spanning from the base of the Canyon Formation to the top of the Cisco Formation was divided into at least four high-frequency sequences (Waite, 1993) (Fig. 2.2). Reid and Reid (1991) subdivided the Canyon Formation into six fusulinid biozones and identified three fusulinid biozones in the preserved and incomplete section of the Cisco Formations (Fig.

2.2). The uppermost high-frequency sequence, or sequences, were predicted to likely exist in a specific portion of the Horseshoe Atoll beyond the control of the current dataset (Waite, 1993). In this study, the Canyon Formation is divided into four high-frequency sequences while the Cisco Formations is divided into five high-frequency sequences (Fig. 2.11). The lower three Canyon Formation sequences are dominated by aggradational stacking patterns with fusulinid-crinoid grainstone capped cycles being the most common (Fig. 2.12). The Cisco Formation is dominated by aggradational to retrogradational stacking patterns (Fig. 2.12). Some of the observed leeward progradation was from laterally accreted crinoidal flank beds sourced from phylloid buildups, but some of the westward-filling deposits may have been generated by erosion of the top of the platform and westward shedding of that sediment. Seismically, although there are no clear progradational sigmoids, westward thickening is evident (Fig. 2.13), which was most likely associated with progradation, similar to Straits of the Andros (Eberli and Ginsburg, 1989). In the Cisco Formation, the five high-frequency sequences are recognized using one-dimensional sequence stratigraphic analysis from two crestal wells with the thickest sections (Fig. 2.11). Nonetheless, establishing a 2-D and 3-D stratigraphic framework is not without substantial uncertainty due to the complex architectural variability of such system (Read, 1995).

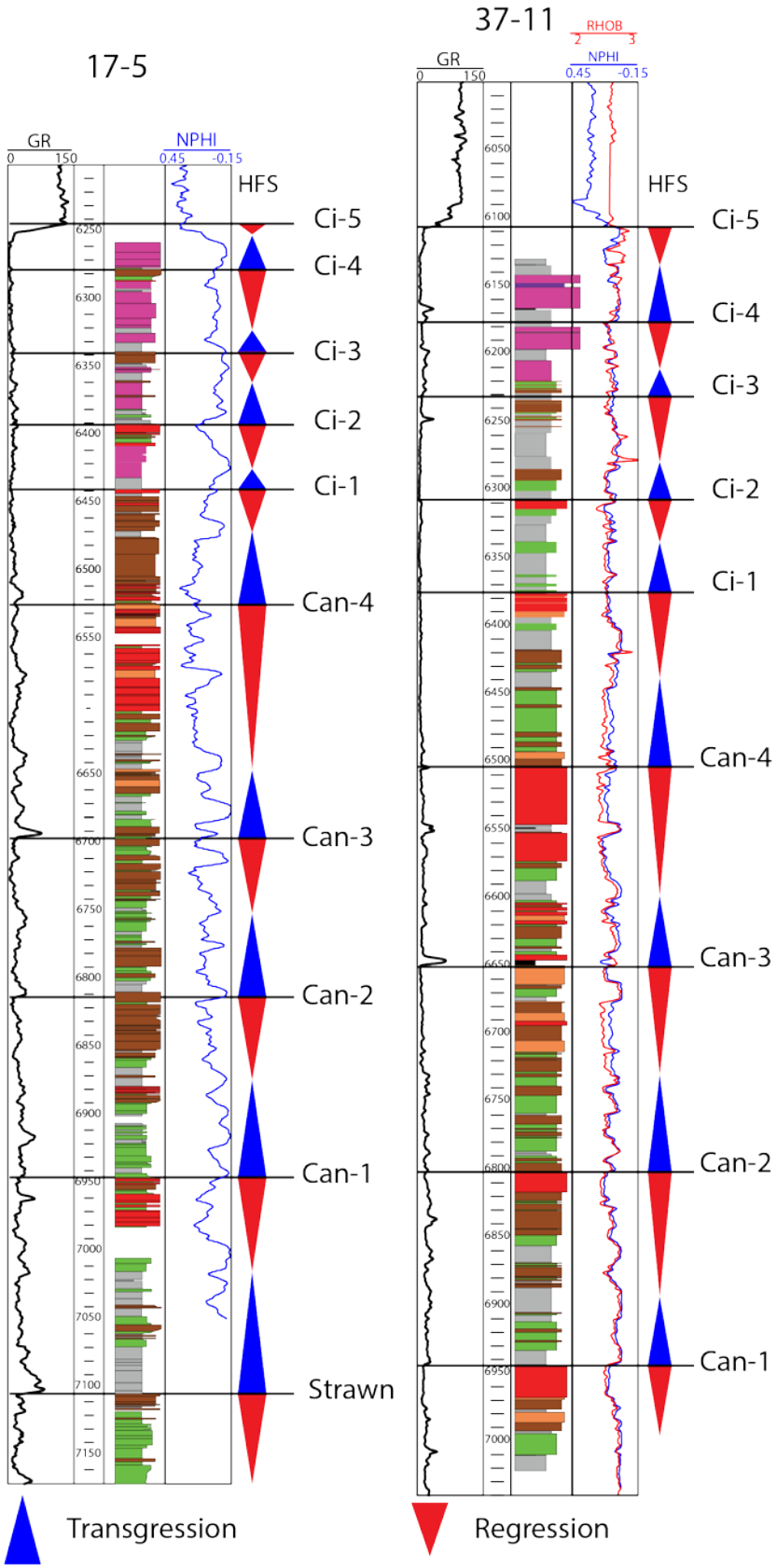
17-5
GR
0 150
NPHI
0.45 -0.15
HFS
Ci-5
Ci-4
Ci-3
Ci-2
Ci-1
Can-4
Can-3
Can-2
Can-1
Strawn
Transgression
37-11
RHOB
2 3
GR
0 150
NPHI
0.45 -0.15
HFS
Ci-5
Ci-4
Ci-3
Ci-2
Ci-1
Can-4
Can-3
Can-2
Can-1
Regression

**Fig. 2.11**: One-dimensional sequence stratigraphic analysis of two crestal wells. The Canyon Formation consists of four high-frequency sequences whereas the Cisco Formation consists of five high-frequency sequences. The Canyon Formation sequences are correlatable across much of the platform with high confidence. The Cisco Formation sequences cannot be correlated beyond local control as much of their thickness and facies stacking patterns are controlled by several factors (e.g., unfilled accommodation, antecedent topography). Core depths are corrected to wireline logs depths. Wireline logs displayed are gamma-ray (GR), bulk density (RHOB) and neutron porosity (NPHI). Blue and red triangles represent transgression and regression, respectively, of the high-frequency sequences (HFS). Depositional lithofacies colors are the same as in Fig. 2.4.

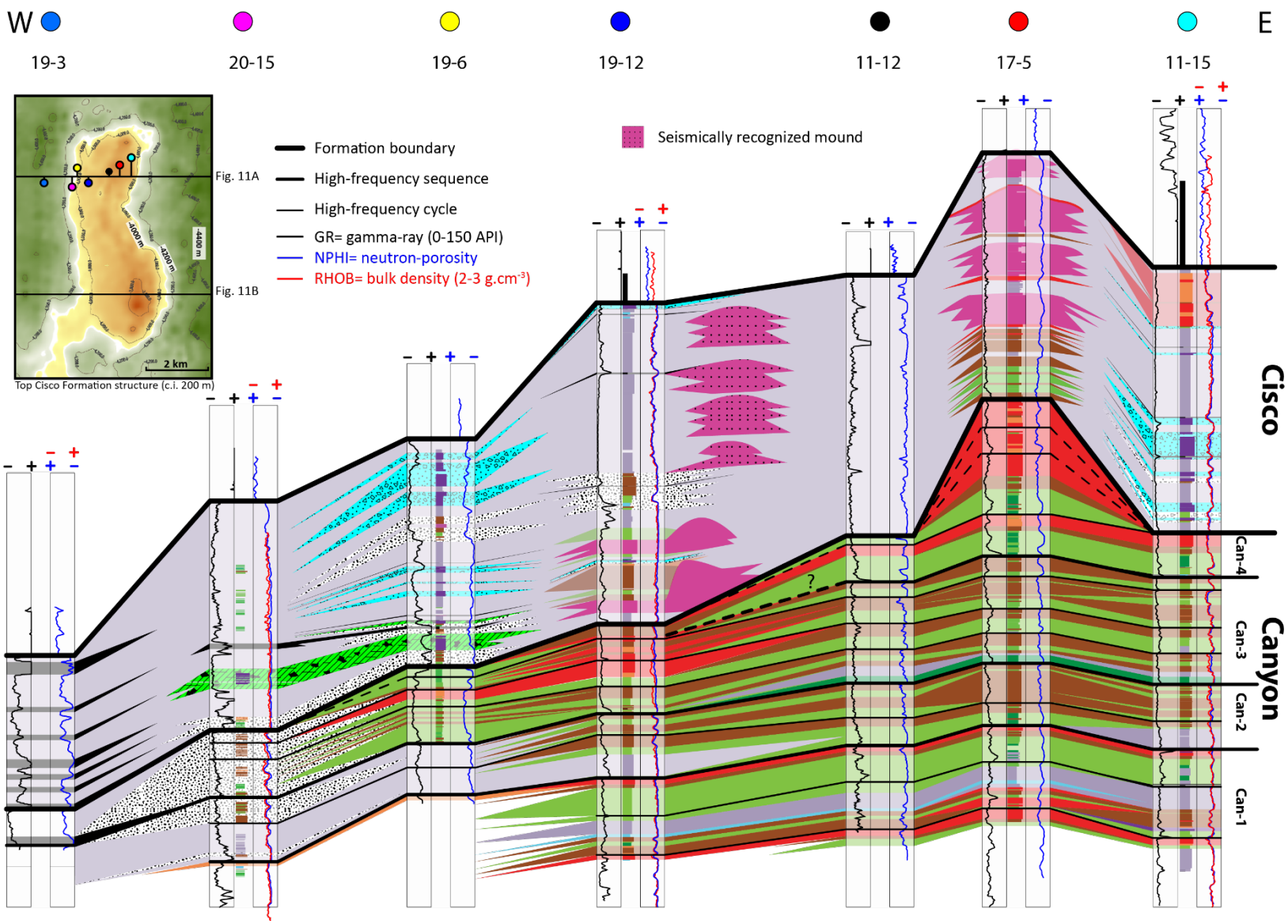
W
E
19-3
20-15
19-6
19-12
11-12
17-5
11-15
Fig. 11A
Fig. 11B
-4000 m
-4200 m
-4400 m
2 km
Top Cisco Formation structure (c.i. 200 m)
Formation boundary
High-frequency sequence
High-frequency cycle
GR= gamma-ray (0-150 API)
NPHI= neutron-porosity
RHOB= bulk density (2-3 g.cm-3)
Seismically recognized mound
Cisco
Canyon
Can-4
Can-3
Can-2
Can-1

**Fig. 2.12**: Correlation panel showing the Canyon and Cisco formations and their lithofacies distribution in the northern part of the SACROC Field including high-frequency cycles and high-frequency sequences. The Canyon cycles and sequences are highly aggradational and can be correlated with high confidence using core and wireline logs. The Cisco Formation shows an overall retrogradational stacking patterns. The complex nature of the Cisco deposit hinders establishing a correlation between wells. Colored wireline logs are the following: black= gamma-ray (range from 0 (left) to 150 (right) api), red= bulk density (range from 2 (left) to 3 (right) g/cm$^3$), and blue= neutron density (ranges from -0.15 (right) to 0.45(left)). Depositional lithofacies colors are the same as in Fig. 2.3. Colored circles correspond to well location on inset map. Map shows the top of Cisco Formation structure with contour intervals (c.i.) of 200 m.

**Strawn high-frequency sequences**

The Desmoinesian Strawn Formation sits unconformably on top of the Mississippian and has been divided into five cycles based on biostratigraphy and wireline character (Waite, 1993). However, the unconformity is still debatable as a conformable succession of the Atokan and Desmoinesian strata in parts of the Horseshoe Atoll (Vealmore and Oceanic fields) is suggested by Wright (2011). The upper contact of the Strawn and the overlying Canyon is characterized by type 2 sequence boundary where transgressive subtidal deposits of the Canyon overlie the grainstones of the uppermost

Strawn (Waite, 1993). In the Central Basin Platform, the upper contact of the Strawn is characterized by type 1 sequence boundary indicated by subaerial exposure features (Stafford, 1959; Reid and Reid, 1991; Saller et al., 1999).

Sedimentological details of the top-Strawn (basal contact of the Canyon Formation) can only be recognized from one cored well (17-5) that penetrated the Pennsylvanian succession from the latest Virgilian and down into the upper Desmoinesian (Fig. 2.11). The contact is a sequence boundary characterized by fusulinid-crinoid grainstone with blackened grains which are interpreted to represent paleosols and subaerial exposure (Goldstein, 1988). The top-Strawn surface is corroborated by paleontological data showing *Beedeina* fusulinids below the Strawn sequence boundary and *Triticites* above it (Schatzinger, 1987; Wahlman, 2013). Seismically, the top-Strawn is consistently a strong reflector that can be mapped with ease across the entire study area (Fig. 2.13). The uppermost cored interval of the Strawn (7,106'–7,562') consists of six high-frequency sequences (HFS) (Fig. 2.14A). Whereas the transgressive system tract (TST) of the sequences is composed predominantly of skeletal wackestone and mudstone, the highstand system tract (HST) is comprised of peloid-skeletal and fusulinid-crinoid grainstones that often show subaerial exposure features including calichification and blackened grains.

A)

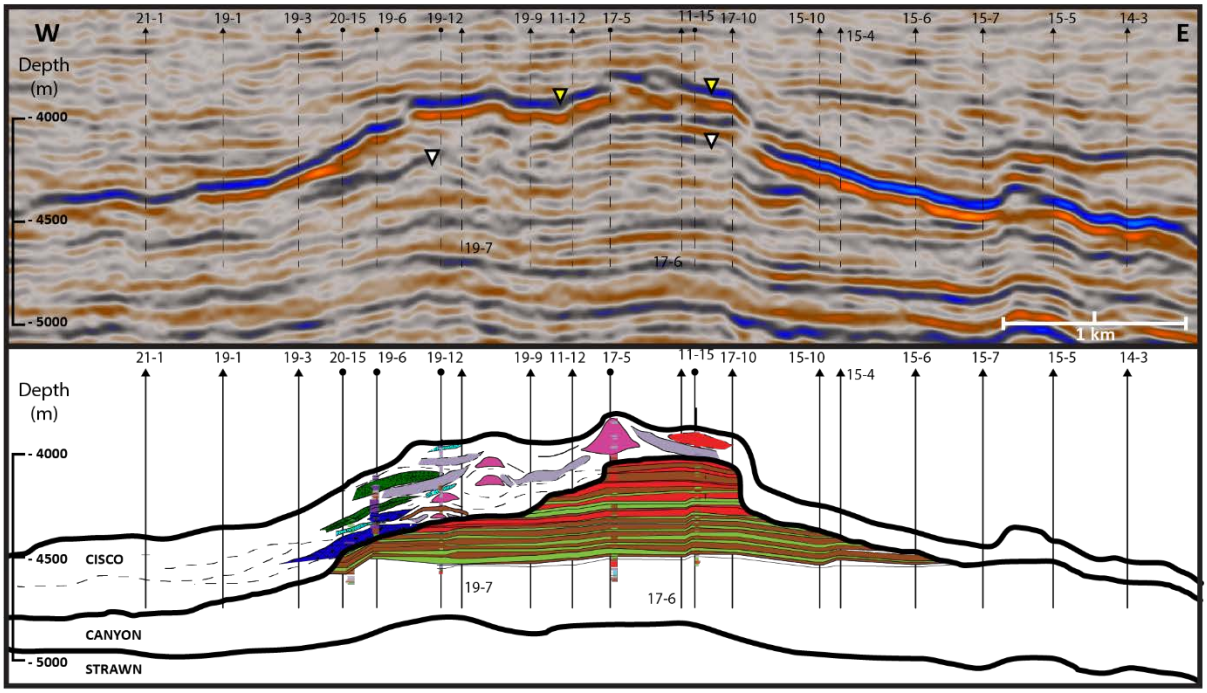


B)

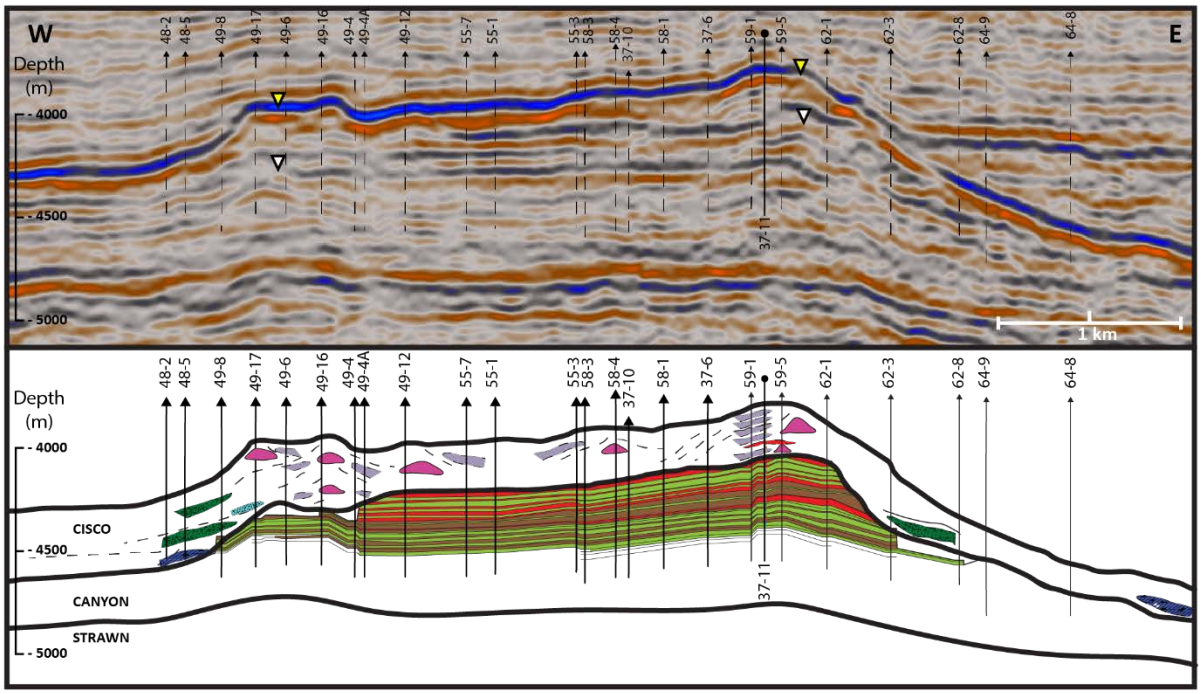


Ooid grainstone
Pylloid boundstone
Debris flows
Turbidites
Fusulinid-crinoid grainstone/gdp
Crinoid-phylloid wackestone/packestone
Fusulinid-crinoid wackestone/packstone
Concentrated density flow
well with core and wireline logs
well with wireline logs only
Cisco-time platform margins
Canyon-time platform margins

**Fig. 2.13**: Two uninterpreted and interpreted seismic profile of the Canyon and Cisco formations. Location of seismic lines in (A) and (B) are shown in the inset map in Fig. 2.11. The Canyon Formation shows mostly aggradational stacking dominated by grainstone capped cycles. The Cisco Formation is dominated by phylloid algal mounds, flank facies, and intermound complexes and shows a significant thickening and progradation towards the leeward side with abundant marine gravity flow deposits. Vertical exaggeration = 31X.

**Canyon high-frequency sequences**

Early transgression of the Canyon is documented from one well (17-5) where a flooding surface separates the top of the Strawn fusulinid-crinoid grainstone from the crinoid wackestone of the Canyon (Fig. 2.14B). The Canyon Formation has a maximum thickness of 175 m and can be divided into four high-frequency sequences (Can-1 through Can-4). Each high-frequency sequence consists of several mappable transgressive-regressive high-frequency cycles (HFC) (Fig. 2.14B-2.14E).

The Can-1 high-frequency sequence has a maximum thickness of 48 m and is composed of two transgressive-regressive high-frequency cycles (Can-1a and Can-1b) (Fig. 2.14B). High-frequency cycles can be correlated across the field using primarily neutron-porosity log (NPHI). In general, low neutron-porosity readings correspond to mud-dominated deposits of the TST whereas high readings coincide with grain-dominated facies of the HST (Fig. 2.11, 2.14). Utilization of neutron-porosity logs proved to be successful and consistent throughout the Canyon succession (Fig. 2.12). Nonetheless, exposure events

at cycles' tops may reduce porosity; especially during periods of prolonged exposure (Saller et al., 1999), which may change the log character (e.g., Can-4c) and hinder the correlation between wells (Fig. 2.14E).

The Can-1a high-frequency cycle has a maximum thickness of about 15 meters. The transgressive system tract of the Can-1a high-frequency cycle consists of thick skeletal and crinoid wackestone units with chert (Fig. 2.14B) overlain by peloid-skeletal grainstone of the HST. The top of the Can-1a high-frequency cycle is overlain by skeletal and crinoid wackestones (~26 m) marking the transgression of the Can-1b. The overlying HST of the Can-1b is characterized by ooid and coated-grain grainstones punctuated by multiple exposure surfaces (Fig. 2.14B).

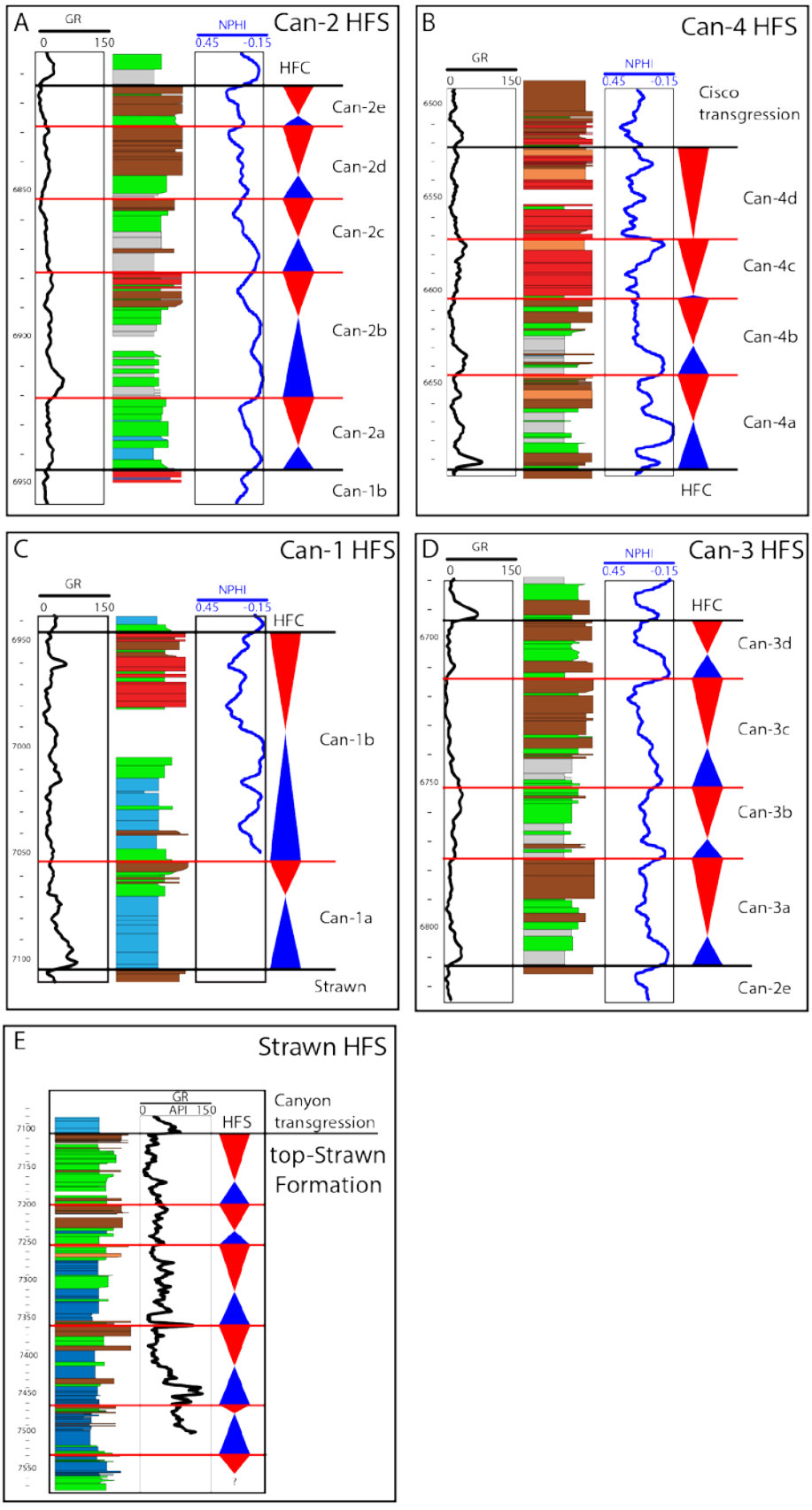
A
Can-2 HFS
GR
0
150
NPHI
0.45
-0.15
HFC
Can-2e
Can-2d
Can-2c
Can-2b
Can-2a
Can-1b
6850
6900
6950
B
Can-4 HFS
GR
0
150
NPHI
0.45
-0.15
Cisco
transgression
Can-4d
Can-4c
Can-4b
Can-4a
HFC
6500
6550
6600
6650
C
Can-1 HFS
GR
0
150
NPHI
0.45
-0.15
HFC
Can-1b
Can-1a
Strawn
6950
7000
7050
7100
D
Can-3 HFS
GR
0
150
NPHI
0.45
-0.15
HFC
Can-3d
Can-3c
Can-3b
Can-3a
Can-2e
6700
6750
6800
E
Strawn HFS
GR
0
API
150
HFS
Canyon
transgression
top-Strawn
Formation
7100
7150
7200
7250
7300
7350
7400
7450
7500
7550

**Fig. 2.14**: Detailed facies stacking patterns and log character of the Strawn and Canyon high-frequency sequences (HFS) and detailed high-frequency cycles (HFC) within the Canyon HFSs in well 17-5. HFCs and HFSs were used to correlate wells across the SACROC Field. Wireline logs are gamma-ray (GR) in black (range: 0 to 150 api) and neutron porosity (NPHI) in blue (range: -0.15 to 0.45). Depositional lithofacies colors are the same as in Fig. 2.4.

The Can-2 high-frequency sequence has a maximum thickness of 42 m and consists of five transgressive-regressive high-frequency cycles (Can-2a through Can-2e) (Fig. 14C). As the lowermost high-frequency cycle, Can-2a is about 8-meter-thick and sits unconformably on top of Can-1 high-frequency sequence. Crinoid wackestone of the Can-2a TST is overlain by the HST peloid-skeletal grainstone and grain-dominated packstone. In the following Can-2b high-frequency cycle, the TST is composed of fusulinid-crinoid and crinoid wackestones overlain and capped by fusulinid-crinoid grainstones of the HST. Locally, the top of the Can-2b high-frequency cycle is marked by cemented oolitic grainstone (e.g., 17-5) (Fig. 2.14C). The Can-2b cycle boundary is marked by a sharp upper contact separating fusulinid-crinoid and ooid grainstones of the HST from fusulinid-crinoid wackestones of the ensuing transgression of the Can-2c. Regressive fusulinid-crinoid grainstones overlie the lower wackestones of the Can-2c TST. The succeeding Can-2d and Can-2e high-frequency cycles have the same facies stacking patterns as Can-2c; however, changes in cycle thickness and facies proportions are observed (Fig. 2.14C). While Can-2d has the same thickness as the Can-2c, Can-2d has thicker HST fusulinid-crinoid grainstones at the expense of fusulinid-crinoid wackestones of the TST. In the same way,

the Can-2e high-frequency cycle shows similar facies proportions to those of the Can-2d but with thinner section (4 m) (Fig. 2.14C). The top of the Can-2e marks the sequence boundary of the Can-2 HFS characterized by a facies offset of the Can-3 transgression.

Total thickness of the Can-3 high-frequency sequence is 28 m and consists of four transgressive-regressive high-frequency cycles (Can-3a through Can-3d) that are mappable across the field. The basal contact of the Can-3a high-frequency cycle is a sequence boundary marked by a facies offset that separates fusulinid-crinoid grainstone of the top Can-2 high-frequency sequence from fusulinid-crinoid wackestone of the Can-3 HFS transgression. This transgression marks an evident change of facies proportions (Fig. 2.14D) where deeper, muddier wackestones become thicker at the expense of grainstones reflecting a relative rise in sea level. The TST of the lowermost HFC (Can-3a) is marked by thick, transgressive fusulinid-crinoid wackestones overlain and capped by regressive fusulinid-crinoid grainstone. The following Can-3b high-frequency cycle has a thickness of about 8 m, showing an upward reduction in thickness and abundance of fusulinid-crinoid grainstone during transgression which was replaced and capped by subaerially exposed fusulinid-crinoid packstones marked by blackened grains (Goldstein, 1988).

The Can-3c high-frequency cycle is about 11 meters thick and marks the turnaround from transgression to regression of the Can-3 high-frequency sequence. The TST of the Can-3c high-frequency cycle is composed of fusulinid-crinoid wackestone and packstone overlain and capped by thick fusulinid-crinoid grainstone. Following Can-3c, the Can-3d high-frequency cycle is thinner with a maximum thickness of 7-m and shows a change in facies proportions with thicker regressive fusulinid-crinoid grainstone at the expense of

transgressive wackestones and packstones. The top of the Can-3d high-frequency cycle marks the sequence boundary of the Can-3 HFS.

The Can-4 high-frequency sequence has a maximum thickness of 48 m and consists of three transgressive-regressive high-frequency cycles (Can-4a through Can-4c) and one regressive high-frequency cycle (Can-4d). In contrast to the lower three high-frequency sequences of the Canyon (Can-1 through Can-3), the Can-4 high-frequency sequence has a limited lateral and areal extent.

The TST of the Can-4a high-frequency cycle is marked by a significant change in cycle's thickness and facies proportions above the Can-3 sequence boundary. Cycle thickness increased to 12 m compared to preceding high-frequency cycle (Can-3d) with thicker fusulinid-crinoid wackestone units. Multiple subaerial exposure events, recognized by blackened grains, punctuate fusulinid-crinoid and peloid skeletal grainstones of the Can-4a HST.

The Can-4b high-frequency cycle is about 13 meters thick and represents the maximum transgression pulse of the Can-4 high-frequency sequence. Whereas the TST of the Can-4b high-frequency cycle is composed almost entirely of fusulinid-crinoid wackestone and packstone, the HST is composed of thin fusulinid-crinoid grainstone that caps the cycle (Fig. 2.14E). In the overlying Can-4c, the thickness is 10 m with a thin TST comprised of fusulinid-crinoid wackestones and a thick HST composed of mainly peloid-skeletal and ooid grainstones (Fig. 14E). Can-4c HST is extensively calichified suggesting multiple subaerial exposure events. In some of the cored wells, the top of this cycle is cemented, which may introduce uncertainty in neutron-porosity log correlation as tight

zones are correlated to porous zones (Fig. 2.14E). Nevertheless, the approach mentioned above utilizing neutron-porosity log still stands as the best tool for correlation (Fig. 2.15).

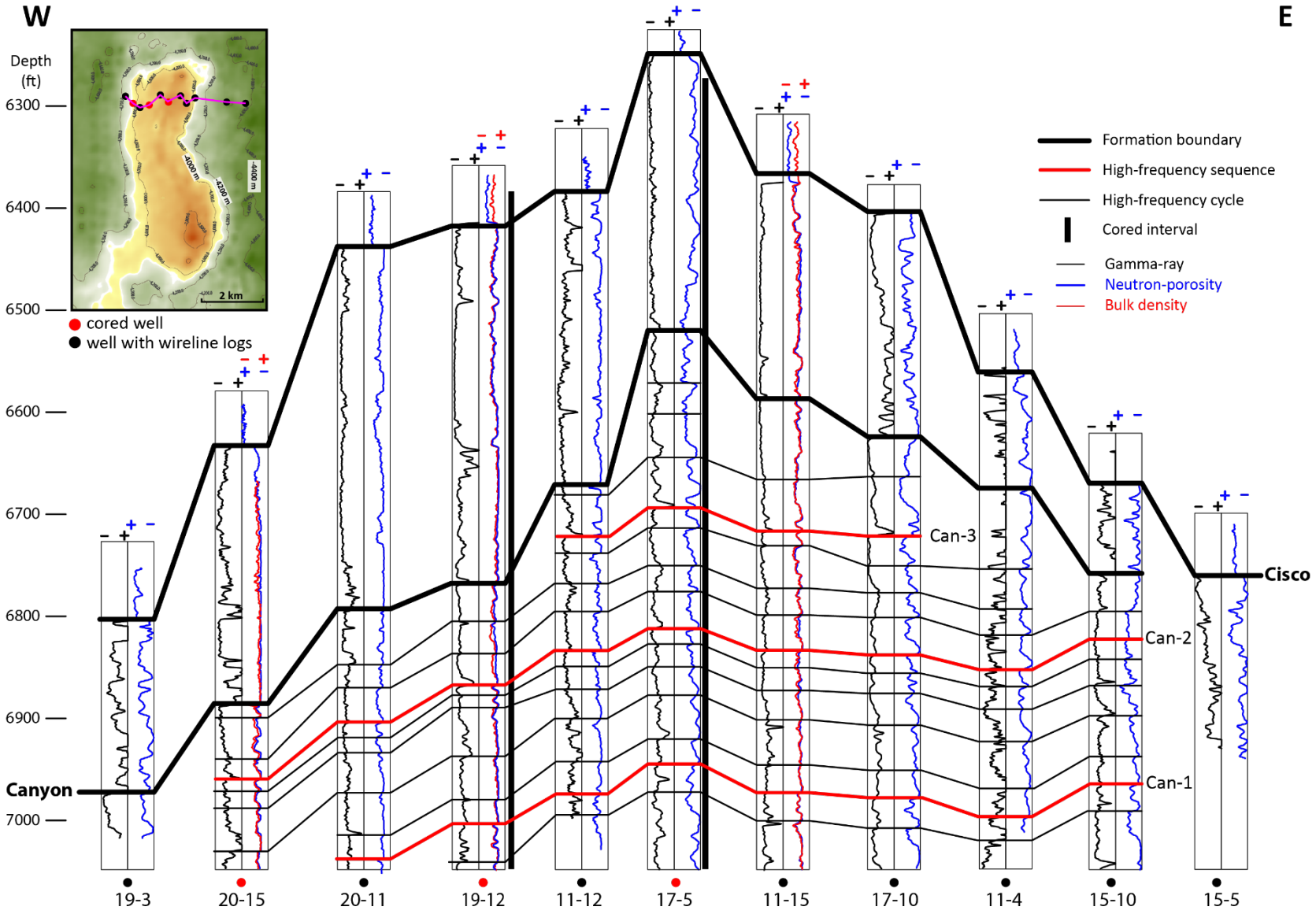
W
E
Depth (ft)
6300
6400
6500
6600
6700
6800
6900
7000
cored well
well with wireline logs
2 km
Formation boundary
High-frequency sequence
High-frequency cycle
Cored interval
Gamma-ray
Neutron-porosity
Bulk density
Canyon
Can-3
Can-2
Can-1
Cisco
19-3
20-15
20-11
19-12
11-12
17-5
11-15
17-10
11-4
15-10
15-5

**Fig. 2.15**: Correlation panel showing the consistent neutron log character used to correlate the Canyon high-frequency cycles and sequences across the field. Circles correspond to well locations on the inset map where reds are cored wells and blacks are wells with wireline logs only. Map shows the top of Cisco Formation structure with contour intervals (c.i.) of 200 m. Wireline logs include gamma-ray (black; range 0-150 api), neutron porosity (blue; range -0.15 to 0.45), and bulk density (red; range 2 to 3 g/cm$^3$).

The Can-4d high-frequency cycle is about 14 meters thick and is composed almost entirely of ooid and peloid-skeletal grainstones that are extensively calichified. This suggests an increased frequency of eustatic fluctuations driving the development of multiple exposure horizons. Increased frequency of subaerial exposure events, limited lateral extent of the Can-4d, and the evident change in seismic character laterally (Fig. 2.13) point to possible dissolution and karst features that may have developed during this time. These features may have been removed and reworked down-dip during the ensuing transgression of the Cisco. Seismically, in areas where the upper part of the Canyon is missing, the flat-bedded character of seismic reflectors turns into chaotic (Fig. 2.13).

**Cisco high-frequency sequences**

Facies in the Cisco Formation are dominated by a mixture of phylloid boundstones and their flank facies. This succession represents a challenge to standard sequence stratigraphic analysis tools. A major assumption in sequence stratigraphic analysis is that shallowing upward cycles fill accommodation space. However, the dominance of subtidal

facies and the scarcity of gradually shallowing depositional facies, especially facies forming at sea level (e.g. ooids), suggest that accommodation space is not completely filled. The Virgilian stage of the Late Pennsylvanian was a time of peak icehouse conditions (Veevers and Powell, 1987; Isbell *et al.*, 2003; Alnazghah and Kerans, 2018). This peak icehouse eustasy forced a complex stratigraphic architecture. Part of the complexity is intrinsic to the strong eustatic signal and associated unfilled accommodation space (Eberli and Grammer, 1999; Janson and Kerans, 2007; Eberli, 2013). One-dimensional stratigraphic analysis is one of the foundations of the 2-D and 3-D stratigraphic correlation frameworks and may be carried out successfully on the platform top, where facies can fill accommodation; however, during peak icehouse eustatic fluctuations in the Virgilian, correlation is hindered by much of unfilled accommodation and missed beats (Hardie et al., 1986; Goldhammer et al., 1990).

Missed beats are stratigraphic records that are not considered due to their absence in the area of investigation resulting in an incomplete record. Missed beats are produced by sea level oscillation below the platform (Fig. 2.16A) or by a pulsed transgression where subtidal facies amalgamate without distinguishing character (Fig. 2. 16B).

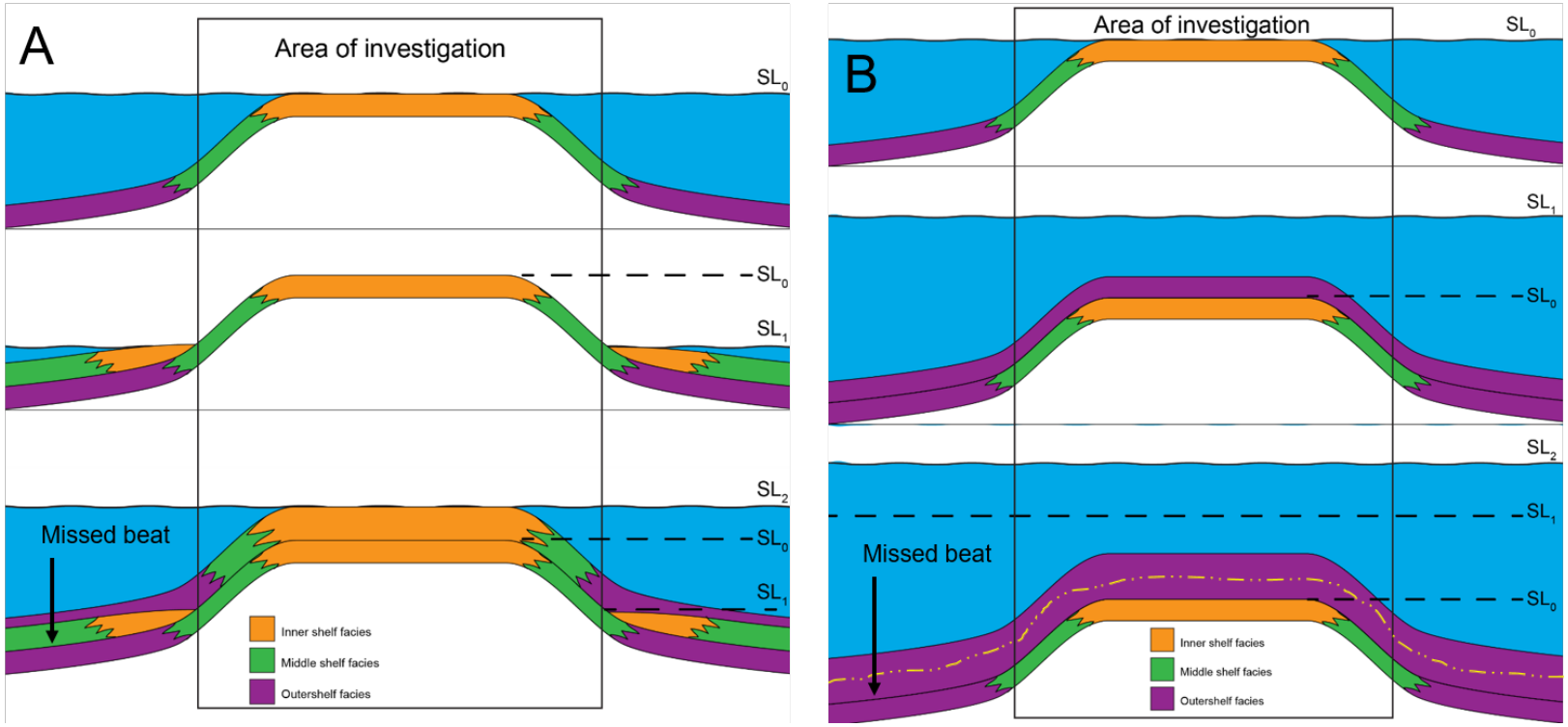


**Fig. 2.16:** Missed beats are stratigraphic records that lies outside the area of investigation during fall of sea level below the shelf (A) or records of amalgamated subtidal deposits in which individual sea level pulses cannot be recognized (B). Yellow dashed line refer to the top of otherwise undiscernible cycle.

During Cisco deposition, the platform top was dominated by phylloid mounds and flank debris. Field observations of time-equivalent mounds in Holder Formation (Virgilian), Sacramento Mountains, New Mexico suggest that mounds on platform top are composed of 20% core and 80% flank debris (Janson and Madriz, 2012). The platform's leeward margin was dominated by off-platform current-reworked and gravity-driven deposits. As a result, the leeward margin was mostly accretionary and net-progradational, whereas the windward margin was net-aggradational owing to on-platform sediment transport. Thus, the highly complex facies architecture and absence of any consistent wireline signatures that can be correlated with confidence hinder establishing a 2-D correlation (Fig. 2.12). Consequently, the sequence analysis presented here is derived from 1-D stratigraphic analyses principally from two wells (well 17-5 & 37-11) (Fig. 2.11) in conjunction with seismic stratal geometries. Using this approach, five high-frequency sequences are recognized in the Cisco Formation (Ci-1 to Ci-5).

The first high-frequency sequence (Ci-1) sits unconformably above the Canyon Formation. The TST across the entire platform reflects a significant facies offset associated with a substantial rise in sea level (Fig. 2.12). On the windward side of the platform, the platform margin remains almost stationary (Fig. 2.13B), whereas on the leeward side, the margin backsteps toward the windward margin, reducing the width of the platform top by 0.5 km (Fig. 2.13A). While Ci-1 transgression covered the platform with fusulinid-crinoid wackestone and crinoid-phylloid wackestone, ooid grainstone and fusulinid-crinoid grainstone were deposited and subsequently punctuated by multiple exposure events during regression. The TST of the Ci-2 is characterized by fusulinid-crinoid and crinoid-phylloid

packstone/wackestone, whereas the HST is expressed by a gradual shift in facies proportions and increased thickness of shallow-water ooid grainstone. (Fig. 2.11).

An aggradational stacking pattern characterizes the Ci-3 high-frequency sequence (Fig. 2.11, 2.12). The transgression of the Ci-3 is marked by a significant facies offset that separates crinoid-phylloid wackestone/packstone from ooid grainstones of the Ci-2 HST. Regressive fusulinid-crinoid grainstones characterize the HST of the Ci-3.

Crinoid-phylloid wackestones overlying the top of Ci-3 sequence boundary represent the transgression of the Ci-4 (Fig. 2.11), in which the maximum flooding surface is marked locally by shale (well 37-11) (Fig. 2.11). While the succession shallows to and is capped by fusulinid-crinoid grainstones (well 17-5), the Ci-4 HFS is capped locally by crinoid-phylloid packstones with subaerial exposure features (well 37-11).

In the following Ci-5 high-frequency sequence, the transgression is characterized by crinoid-phylloid wackestone/packstone and crinoid rudstone that probably aggraded prior to the next pulse of transgression causing the platform drowning. The HST of the Ci-5, at well 37-11, shows an aggradational stacking of crinoid-phylloid wackestone/packstone and crinoid rudstone, whereas in well 17-5, located upwind from 37-11, shows grainer deposits (Fig. 2.11).

## PLATFORM GEOMETRY

### Structure and thickness

Combined isopach and structure contour maps were generated by interpreting the top of the Strawn, Canyon and Cisco formations in the 3-D seismic volume and

incorporating borehole data to constrain thickness and vertical position. The growth of the Horseshoe Atoll was influenced by persistent paleo-east-to-west winds (Walker et al., 1995). High-energy conditions along the windward margin allowed for deposition, early cementation, and stabilization and therefore growth compared to the leeward margin that was dominated by off-platform transport (Mullins and Cook, 1986). A series of structure contour maps (Fig. 2.16) shows the evolution of the platform from a broad, low-relief system during the Strawn deposition through a distinctly asymmetrical profile with an elevated easterly rim as the SACROC platform drifted northward during the deposition of the Canyon and Cisco formations.

In general, maps show that sequences on the platform top tend to be thicker on the eastern margin than the western margin of the platform (Fig. 2.16, 2.17), and this asymmetry increases in younger sequences (Fig. 2.18). In the Canyon Formation, the average thickness of the platform top is ~100 m, and the maximum thickness on the eastern margin does not exceed 180 m (Fig. 2.17). The average thickness of the Cisco Formation across the platform top is ~95 m on the eastern margin compared to ~77 m on the western margin. The Cisco Formation thickens significantly (up to 140 m) off the platform leeward margin in the paleo-west direction (Fig. 2.17). The westward (leeward) increase in thickness is related to leeward progradation as well as increased off-bank shedding of sediment during Cisco deposition (Fig. 2.13, 2.17). A similar architecture is observed in the Straits of Andros of the Great Bahamas Bank, where the Middle/Upper Miocene progrades towards the northwest to fill the Straits of the Andros (Eberli and Ginsburg, 1989).

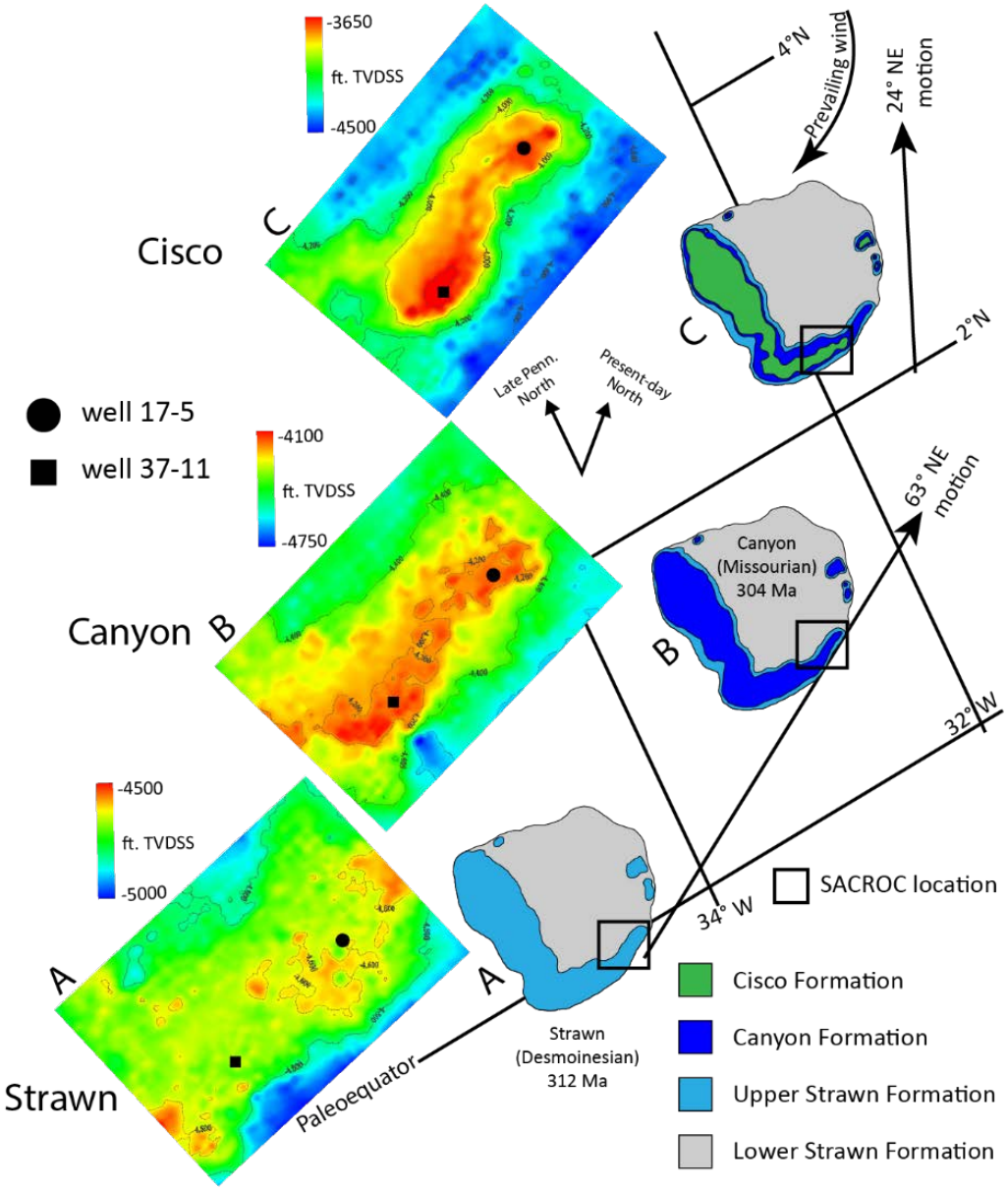
-3650
ft. TVDSS
-4500
Cisco
C
well 17-5
well 37-11
-4100
ft. TVDSS
-4750
Canyon
B
-4500
ft. TVDSS
-5000
A
Strawn
Paleoequator
Late Penn. North
Present-day North
4°N
Prevailing wind
24° NE motion
2°N
63° NE motion
32° W
34° W
Canyon (Missourian) 304 Ma
Strawn (Desmoinesian) 312 Ma
SACROC location
Cisco Formation
Canyon Formation
Upper Strawn Formation
Lower Strawn Formation

**Fig. 2.16**: Depositional and structural evolution of the SACROC platform during the Late Pennsylvanian. The Strawn carbonates were deposited near the paleoequator (A). As the Horseshoe Atoll drifted northward (from Walker et al., 1995), the eastern margin (windward) of the SACROC platform experienced significant depositional relief growth during deposition of the Canyon (B) and Cisco (A) formations giving rise to an east-west asymmetry of the SACROC platform. Bars indicate structural depths true vertical depth subsea (TVDSS) in feet.

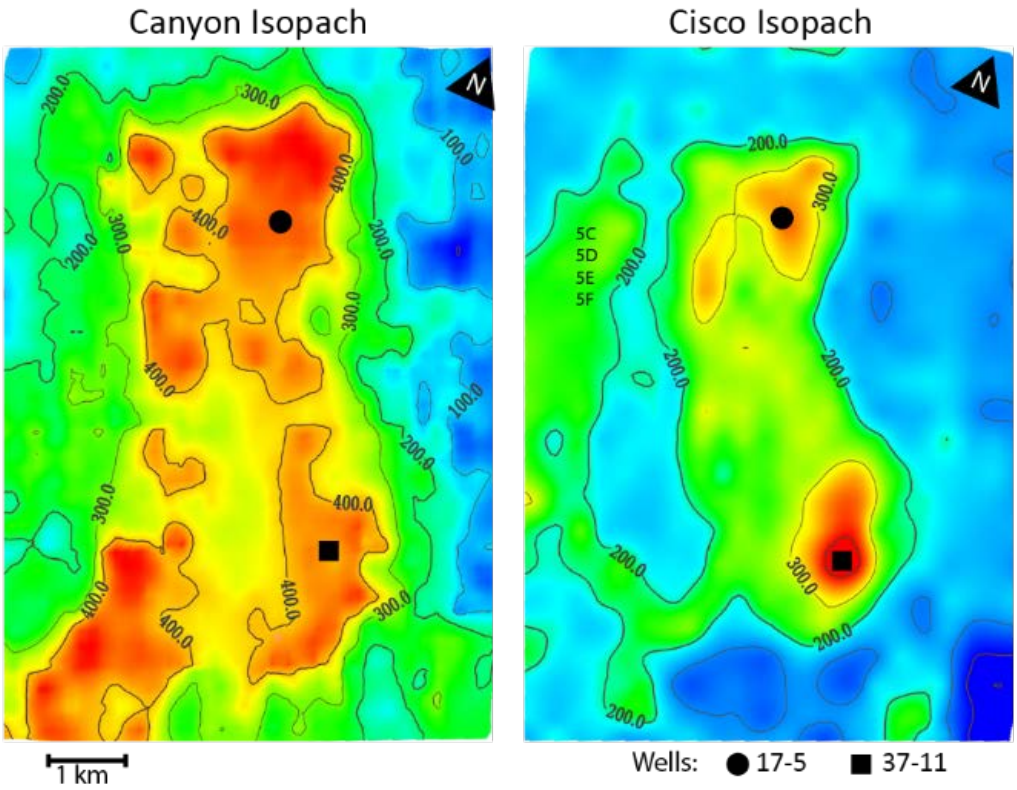


**Fig. 2.17**: Isopach maps of the Canyon and Cisco formations across the SACROC field. Overall the Canyon Formation is thicker than the Cisco Formation and both show a thickening on the eastern margin. The Cisco Formation shows off-platform thickening on the western side as a result of off-platform sediment transport (see Fig. 5C, D, E, F). Thicknesses are in feet.

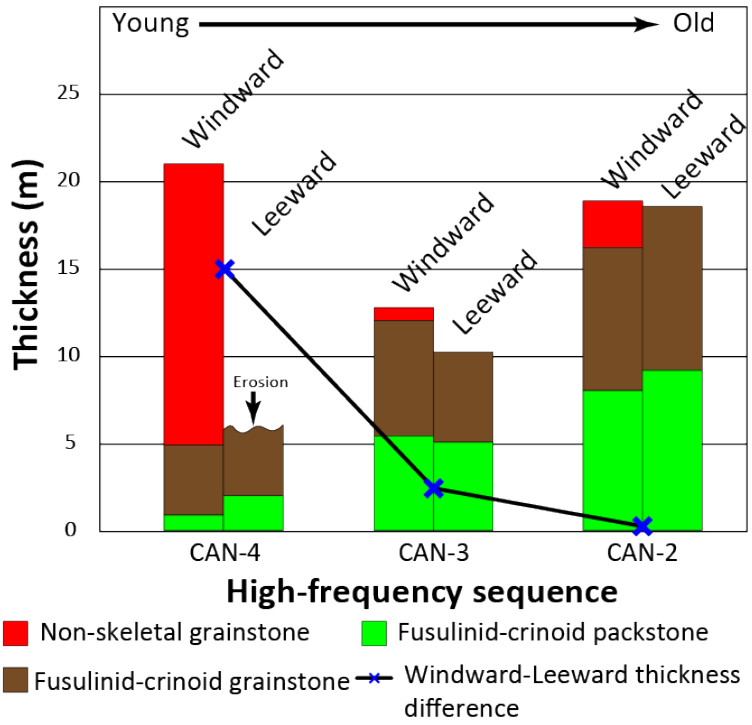


**Fig. 2.18**: Windward versus leeward thickness variation across the east-west profile of the platform top for the Canyon high-frequency sequences (Can-2 through Can-4). The platform becomes exponentially asymmetric in younger sequences. Erosion likely removed parts of the originally deposited succession as shown in Can-4 high-frequency sequence deposited in the leeward side.

**Platform slopes**

Slope angles for the carbonate platform were measured along the upper surface of 4 sequences (Can-2, Can-3, Can-4, Ci-5) for both the windward (east) and the leeward (west) positions (Fig. 2.19). The horizontal distance and vertical height were measured and used to calculate slope angle (Fig. 2.19). Two positions were identified and measured: an

upper slope and a lower slope. The positions of upper and lower slope are determined by recognition of inflection points in seismic, physiographic position and sedimentologic character. Results show that the platform overall is asymmetric with a steeper slope on the windward side (east) than on the leeward side (west). Determining slope angles in a N-S axis was more challenging as a result of data limitations. In general, the gradient becomes steeper in younger sequences for the upper slope especially in the windward side, whereas the difference in the lower slope is limited and becomes similar in younger sequences (Fig. 2.20).

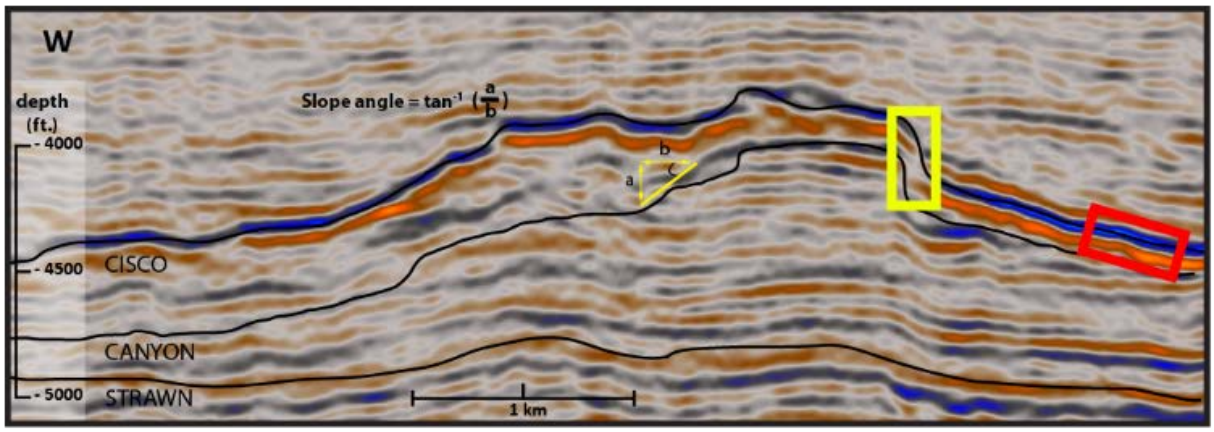


**Fig. 2.19**: Slope angle calculation from a 3-D seismic line using tangent trigonometric function. Two types of slopes were measured, a steeper uppermost slope (yellow box) and a lower gentler slope (red box). Vertical exaggeration is 31X.

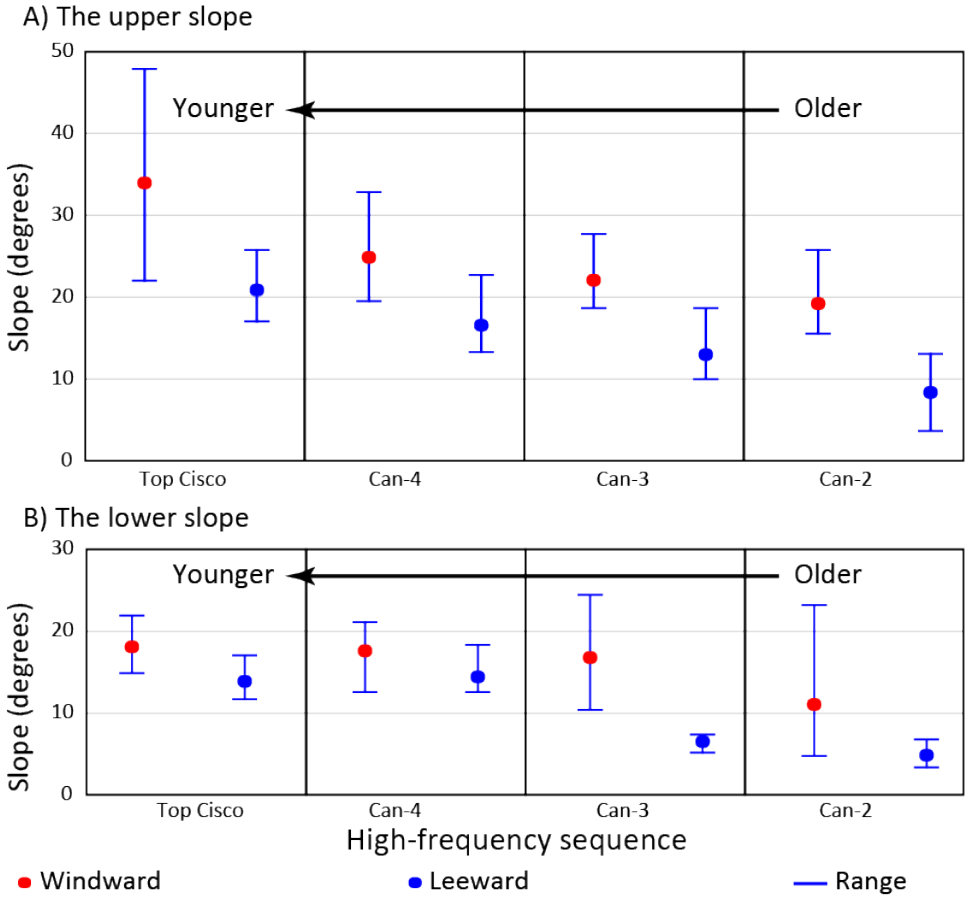


**Fig. 2.20**: Slope evolution through time for several sequences across east-west profile for the windward and leeward margins. A) The upper slope becomes steeper in younger sequences. B) The lower slope in the lower Canyon Formation is steeper at the windward margin but becomes comparable at younger sequences.

The calculated slopes from the SACROC field are comparable in many ways to different datasets of analogous systems (Fig. 2.21). In this study, windward and leeward slope measurements for upper and lower slopes were separated to assess the influence of

the paleogeographic setting on platform's slope (Fig. 2.20, 2.21). Slope declivity measurements have an average that range between 20° and 35° for the upper slope and between 10° and 18° for the lower slope. These slope measurements are similar to the ones reported from Exuma Sound consisting of an upper slope, gullied slope, and lower slope (*sensu* Crevello and Schlager, 1980). These morphologies are different from the Tongue of The Ocean (TOTO) where the anatomy of the upper slope is different. The slope of TOTO is segmented into three main parts: *wall* (70-90°), *cemented slope* (34-35°), and *soft sediment slope* (25-28°) (Grammer and Ginsburg, 1992; Grammer et al., 1993). One remarkable difference when comparing our data to this modern model is the absence of a "*wall*", which may be attributed to the absence of reef framework builders and the action of erosive processes that scallop the margin (Schlager and Camber, 1986). Thus, the margin of the platform is considered "accretionary" rather than "escarpment" (McIlreath and James, 1978; James and Mountjoy, 1983; Playton et al., 2010).

At SACROC, the windward upper slopes ranged from 20° to 47° whereas leeward upper slopes ranged between 10° and 21°. The slopes of the windward margin are remarkably similar to many studied platforms (Fig. 2.21). The Late Devonian Lennard Shelf in Western Australia has upper slopes ranging between 30° and 40° (Playton and Kerans, 2015), the upper Carboniferous Sierra del Cuera, northern Spain, upper slopes ranged between 30° and 35° degrees (Della Porta et al., 2004; Kenter et al., 2005). Similarly, the Triassic of the Dolomites in northern Italy had upper slopes between 30°-40° constructed by the Ladinian reefs with slopes ranging between 20°-30° in the Carnian (Bosellini, 1984). In the subsurface, the Mississippian Tengiz Field has upper slope angles

that range between 20°-25° and 30° for accretionary margins and detachment failure respectively but can reach 35° to 45° locally (Collins et al., 2006). The steeper windward margins were probably the result of early cementation, erosion, and vertical growth of buildup organisms, whereas the gentler leeward margin slopes were reduced because of down-wind transportation and deposition of sediments (Mullins and Cook, 1986).

The lower slopes show similar gradients for both the windward and leeward margins ranging between 6° and 18° with an average of 15°. These slopes are slightly higher than gradients reported for the lower slope from modern and ancient examples. In Exuma Sound, the gradients reported for *gullied slopes* ranged between 12° to 15° whereas the lower slope ranged between 3° and 5° (Crevello and Schlager, 1980). In the Tongue of The Ocean, lower slopes ranged between 6° to 9° (Schlager and Chermak, 1979). In the Paleozoic, the lower slopes of the Lower Frasnian Lennard Shelf ranged between 2° and 10° (Playton and Kerans, 2015). The gradients we report for the lower slope appears to be higher than those reported in most studies, and thus we interpret them to represent gullied slopes (*sensu* Crevello and Schlager, 1980) of an accretionary margin (McIlreath and James, 1978; James and Mountjoy, 1983; Playton et al., 2010).

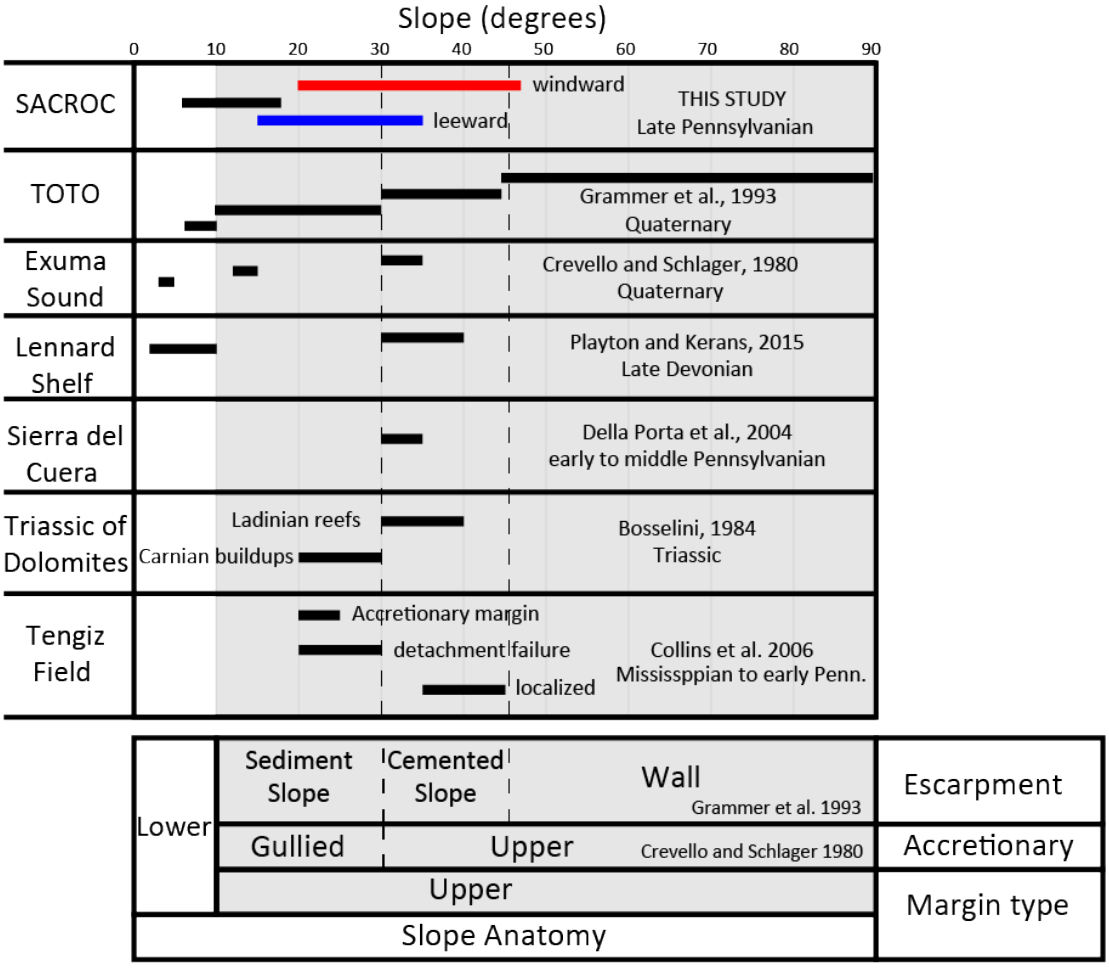


**Fig. 2.21**: A comparison between slope ranges of Phanerozoic platforms from different studies. The slope anatomy is divided into upper and lower slopes. The upper slope is divided into subdivisions by two studies and is mainly controlled by margin type. The upper slope, in general, appears to be stranded between 20° and 40° whereas the lower slope tends to be <10°.

## CONCLUSIONS

Stratigraphic architecture of the Canyon and Cisco formations of the Late Pennsylvanian reveals distinct changes in lithofacies and cycle staking patterns. The Canyon Formation consists of four, highly-aggradational, high-frequency sequences (Can-1 to Can-4), which are composed of several transgressive-regressive high-frequency cycles identifiable in the core and on well log data. Transgressive lithofacies of the Canyon's high-frequency cycles are predominantly composed of fusulinid-crinoid wackestones and packstones, whereas the regressive lithofacies are composed of fusulinid-crinoid and ooid grainstones punctuated by several subaerial exposure horizons that increase in frequency towards the top-Canyon boundary.

The Cisco's internal stratigraphic architecture is remarkably complex because of deposition during peak icehouse conditions, resulting in highly juxtaposed shallow- and deep-water facies with multiple subaerial emergence features. Five high-frequency sequences (Ci-1 to Ci-5) are recognized from 1-D stratigraphic analysis from two cored crestal wells. Establishing correlative timelines between wells is extremely challenging and highly uncertain. The windward margin is net-aggradational owing to on-platform sediment transport, whereas the leeward margin is net-progradational because of dominant off-platform sediment transport. Different modes of sediment transport controlled the platform’s asymmetric morphology and resulted in the development of an accretionary windward margin with steeper upper slopes compared to the leeward margin. This asymmetry is enhanced by early cementation and stabilization of the windward margin.

This study provides an example of the considerations required to assess facies architecture and their relation to porosity distribution and connectivity in a 3-D model. Core, wireline logs, and seismic data analyzed from the SACROC Field illustrates the complexity and heterogeneity of icehouse isolated carbonate platforms. The highlighted complexity of the SACROC Field reveals the need of integrating geological and geophysical data to build a geologically sound model.

# CHAPTER 3: LATE PENNSYLVANIAN GLACIATION: EVIDENCE OF ICEHOUSE CONDITIONS FROM CANYON AND CISCO UNITS, MIDLAND BASIN, TEXAS


## ABSTRACT

The late Paleozoic has long been recognized a time of significant continental glaciation associated with high-frequency, high-amplitude glacioeustasy. Although, precise assessment of glacioeustatic amplitudes are difficult to extract from the stratigraphic record, best approximations may be possible by analyzing spatial and temporal distributions of depositional facies utilizing several wells across the study area. We used detailed sedimentologic description and depositional facies analysis from 12 wells and applied rigorous cycle stacking pattern analysis, exposure surfaces recognition and wireline logs to correlate timelines across the wells. On the basis of the high-resolution sequence stratigraphic framework built for the Scurry Area Canyon Reef Operators (SACROC) field, a highly-resolved glacioeustatic curve was generated for latest Desmoinesian to the latest Virgilian.

Our eustatic curve suggests that the Missourian and Virgilian stages of the late Pennsylvanian are characterized by high frequency, high-amplitude eustatic fluctuations. The Missourian stage was a period dominated grainstone-capped cycles that are isopachous and conformable. These cycles reflect a eustatic amplitude of at least 37 m with an average duration of 100 ka suggesting the dominance of short-term eccentricity signal. The Virgilian stage is far more complicated and is characterized by highly shingled cycles

compared to the Missourian stage. Deeper water phylloid boundstone and calichified shoal complex grainstones are juxtaposed next to each other which suggests a stronger eustatic amplitude (>40 m) compared to the Missourian stage. Although the eustatic amplitude of the Virgilian cycles is similar to those of the Missourian cycles, they have a longer frequency (343 ka) representative of long-term eccentricity.

We conclude that the late Pennsylvanian stratigraphy of the SACROC field in the Midland Basin records extensive continental glaciation during the Missourian stage and increased and reached an acme during the Virgilian stage.

## INTRODUCTION

The Late Paleozoic has been documented to be a time of widespread continental glaciation, but the extent of the glaciation and associated glacioeustasy are not well-constrained (Heckel, 1977; Veevers and Powell, 1987; Crowley and Baum, 1991; Isbell et al., 2003; Fielding et al., 2008; Montañez and Poulsen, 2013; Montañez et al., 2016). Cyclic waxing and waning of Gondwanan ice sheets left not only direct geological evidence of continental glaciation in the stratigraphic record (Wanless and Shepard, 1936; Crowell, 1978; Heckel, 1986; Boardman and Heckel, 1989), but also indirect evidence in diagenetic and stable isotope signatures within low-latitude carbonate platform strata (Adlis et al., 1988; Goldstein, 1991; Dyer and Maloof, 2015). Stratigraphic records from low paleolatitudes are the foundation for our understanding of the Late Paleozoic Ice Age (LPIA). They are considered to be sensitive, indirect representation of the high-frequency glacioeustasy, especially since these records most likely lack or show reduced impact of glacioeustasy.

Early studies of the LPIA argued for one long-term expansive continental ice sheet that existed in southern Gondwana (Veevers and Powell, 1987; Crowley and Baum, 1991; Crowell, 1999). Veevers and Powell (1987) compiled global stratigraphic records and identified three glacial episodes in the Late Paleozoic: Glacial I (Famennian-Tournaisian), Glacial II (early Visean) and Glacial III (Namurian-mid Sakmarian). Although they recognized that Glacial III can be subdivided into three sub-events (IIIA; IIIB; IIIC), they suggested that ice sheets had always existed during that period. However, Isbell et al. (2003) compiled and examined stratigraphic records of the Late Paleozoic in the southern

hemisphere and defined three glacial events separated by non-glacial conditions. Glacial I (Frasnian, Famennian and early Tournaisian) and Glacial II (Namurian to earliest Westphalian) were characterized by alpine glaciers of limited extent and thus eustatic change produced by growth and demise of these glaciers is much smaller than what is inferred from cyclothems and/or incised valleys (Crowley and Baum, 1991; Wignall and Maynard, 1996; Miller and Eriksson, 2000; Butts, 2005; Matchen and Kammer, 2006). On the other hand, waxing and waning of Gondwanan ice sheets during Glacial III (Stephanian to Sakmarian, possibly Kungurian) have produced eustatic fluctuations recorded by cyclothems (Heckel, 1977; 1986; 1994; Veevers and Powell, 1987; Isbell et al., 2003). More recently, Fielding et al. (2008) published a highly resolved record of the LPIA from eastern Australia where they identified eight glacial events separated by nonglacial intervals. Their work suggests that the Missourian and Virgilian stages of the Late Pennsylvanian were nonglacial periods indicative of greenhouse conditions. Further, stratigraphic records from Bird Spring Formation in Arrow Canyon, Nevada (Bishop et al., 2010; Martin et al., 2012) corroborate the dominance of greenhouse conditions during the late Pennsylvanian.

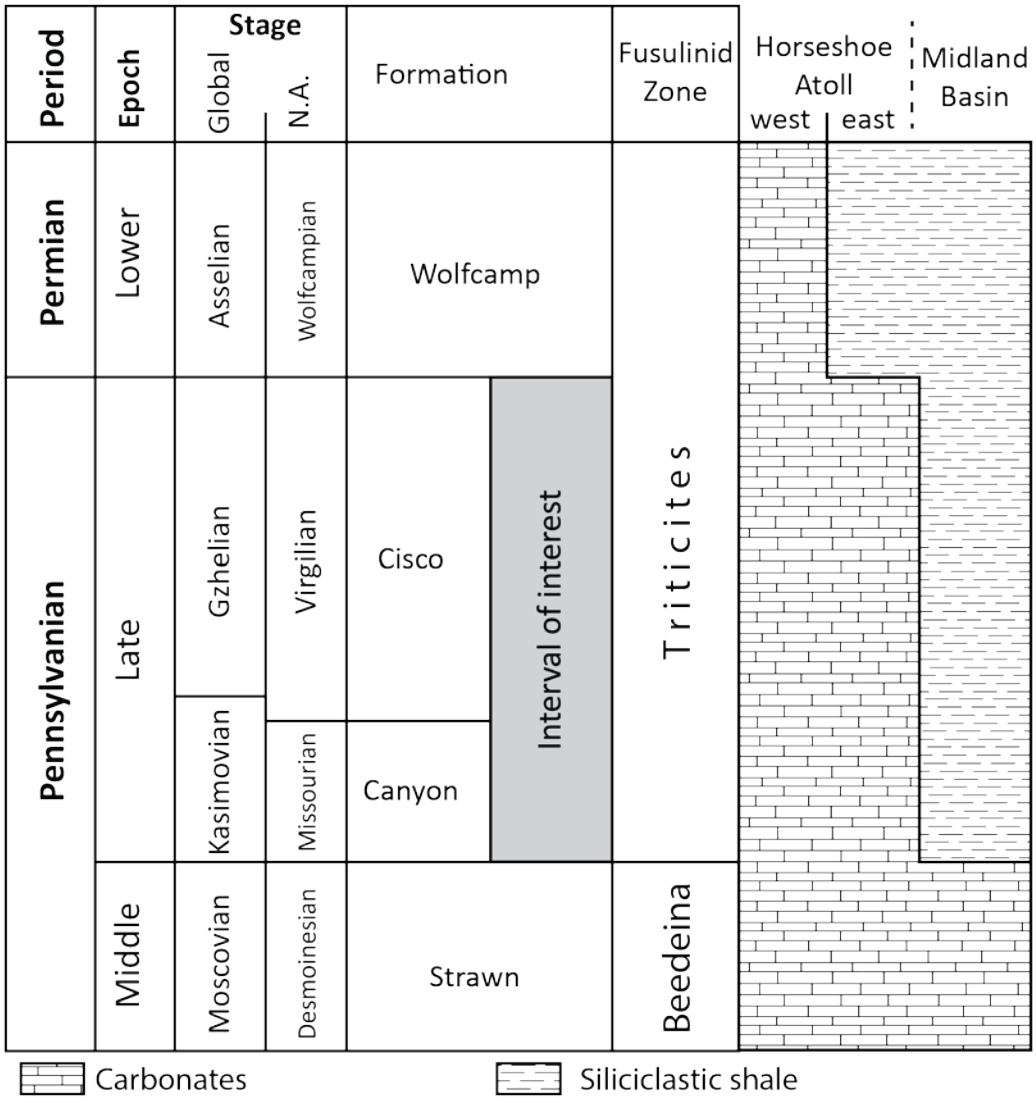


**Fig. 3.1**: Generalized West Texas stratigraphic column showing interval of interest.

In this paper, the Virgilian and the Missourian strata from the SACROC field of the Horseshoe Atoll in the Midland Basin, Texas, USA are examined (Fig. 3.1). The economic importance of the Canyon (Missourian) and the younger Cisco (Virgilian) units, which contain substantial hydrocarbon reserves, makes the study area unique in terms of total available data. An impressive suite of slabbed cores, wireline logs and seismic data from

the SACROC field, including 2,100 m of cores from 12 wells (Fig. 3.2), provides unique insights into this late Pennsylvanian section of the Permian Basin. In addition, the greater subsidence rate at Horseshoe Atoll within the Midland Basin (Fig. 3.3) compared to the other studied regions in the greater Permian Basin allows for a high fidelity stratigraphic record (cf. Waite, 1993; Saller et al., 1994). The combination of abundant subsurface data and greater preservation potential to assess glacioeustasy during the late Pennsylvanian period make the SACROC field a valuable record for this time period. This study helps to further refine the record of glaciation during the LPIA and provides a high-resolution stratigraphic record of how low paleolatitude strata responded to major climate perturbations during icehouse interval.

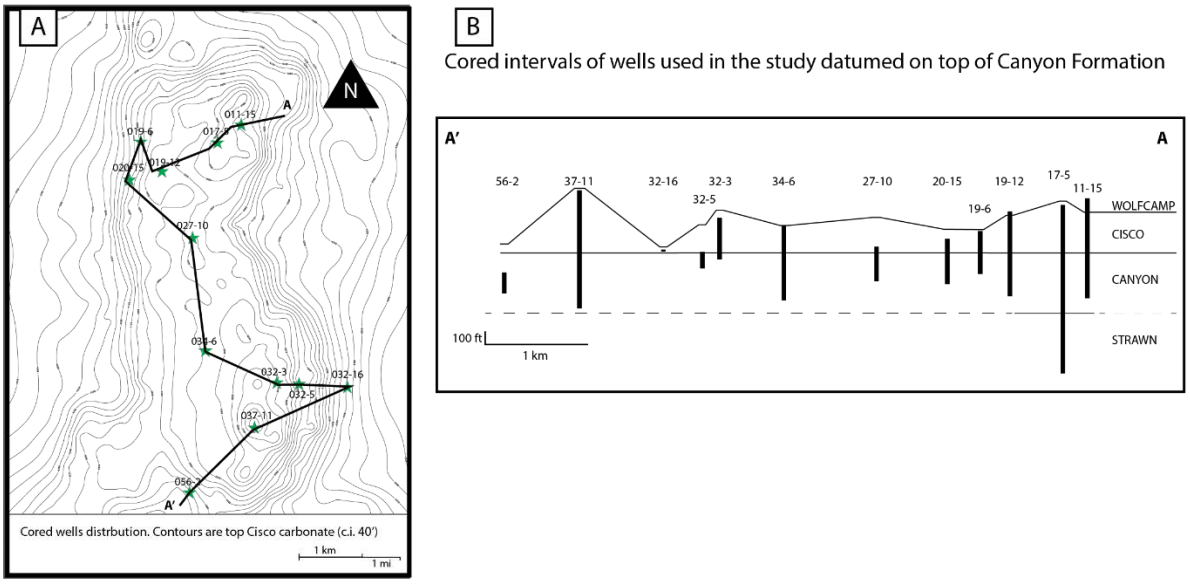


**Fig. 3.2**: A) Structural map of the top Cisco Formation, contour intervals (c.i.) are at 40 ft. B) Cored intervals of wells used in the study.

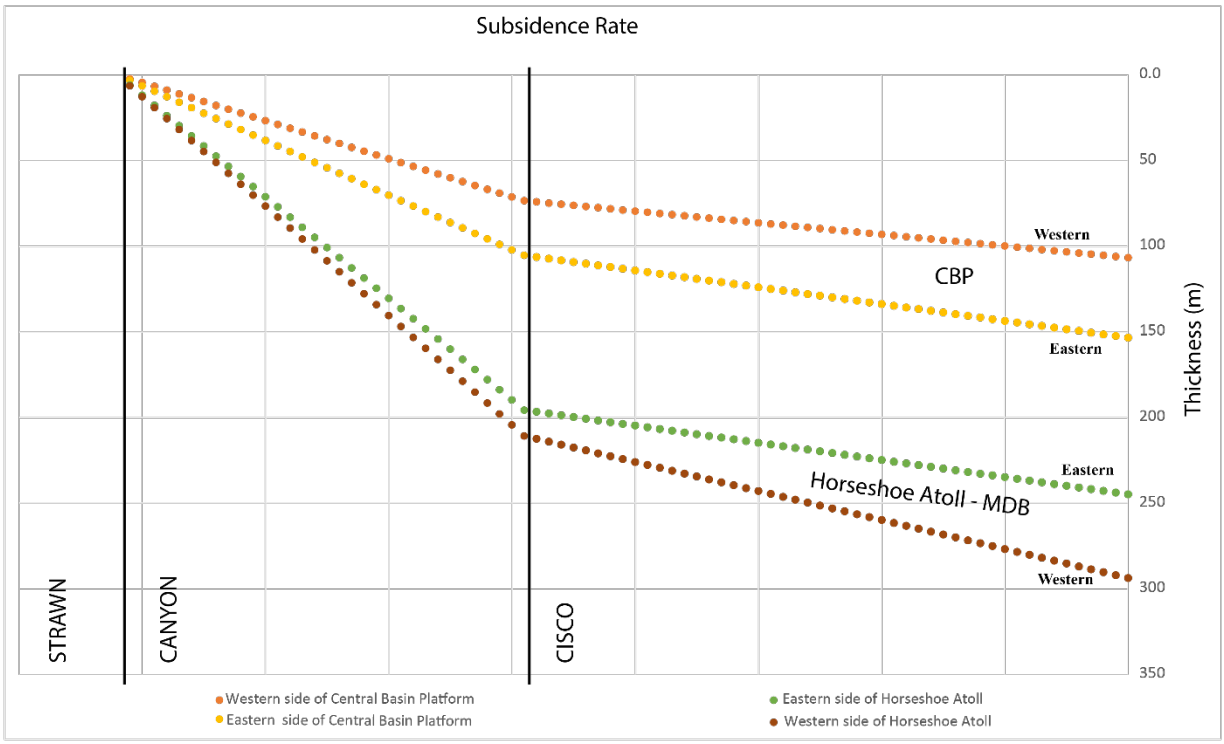


**Fig. 3.3**: Subsidence rate of Central Basin Platform (CBP) and Midland Basin (MDB) during the deposition of Canyon and Cisco. The rate of subsidence was highest during the Canyon, while subsidence continued at slower rates during the Cisco. Increased subsidence in the Midland Basin allowed for a thicker preserved succession of the same age units. Subsidence rates are calculated based on preserved sections with the assumption of constant rate of sedimentation and was not corrected for compaction.

## GEOLOGICAL SETTINGS

The assembly of Pangaea by the collision of Gondwanaland and Laurasia began in the late Devonian. Continent-continent collision occurred during the Pennsylvanian

marking the inception of the Ouachita-Marathon Orogeny (Fig. 3.4) (Lillie et al., 1983; Frazier and Schwimmer, 1987) through the Permian Basin. The dominantly N-S compression imposed by the Ouachita-Marathon thrust system was transformed into E-W compression by strike-slip fault systems (Hills, 1970, 1985). Thrust loading and associated subsidence in the latest Mississippian created the broader Permian Basin depocenter, but transpressive deformation also drove uplift of the Central Basin Platform, a NW trending uplifted basement block, along high-angle reverse faults with an oblique slip component (Fig. 3.4) (Frenzel et al., 1988; Poole et al., 2005). Fault-bounded uplift during the late Pennsylvanian and Early Permian stages produced large carbonate platforms on the western, north and eastern margins of the Permian Basin (Galley, 1958; Frenzel et al., 1988). The Central Basin Platform (CBP) differentiated the twin Delaware and Midland basins (Yang and Dorobek, 1995). The Midland Basin is an asymmetric foreland basin with the deepest part westward against the CBP, which shallows by a gradual rise towards the Eastern Shelf with little evidence of tectonism making the eastern boundary of the Midland Basin somewhat arbitrary (Hills, 1984, 1985).

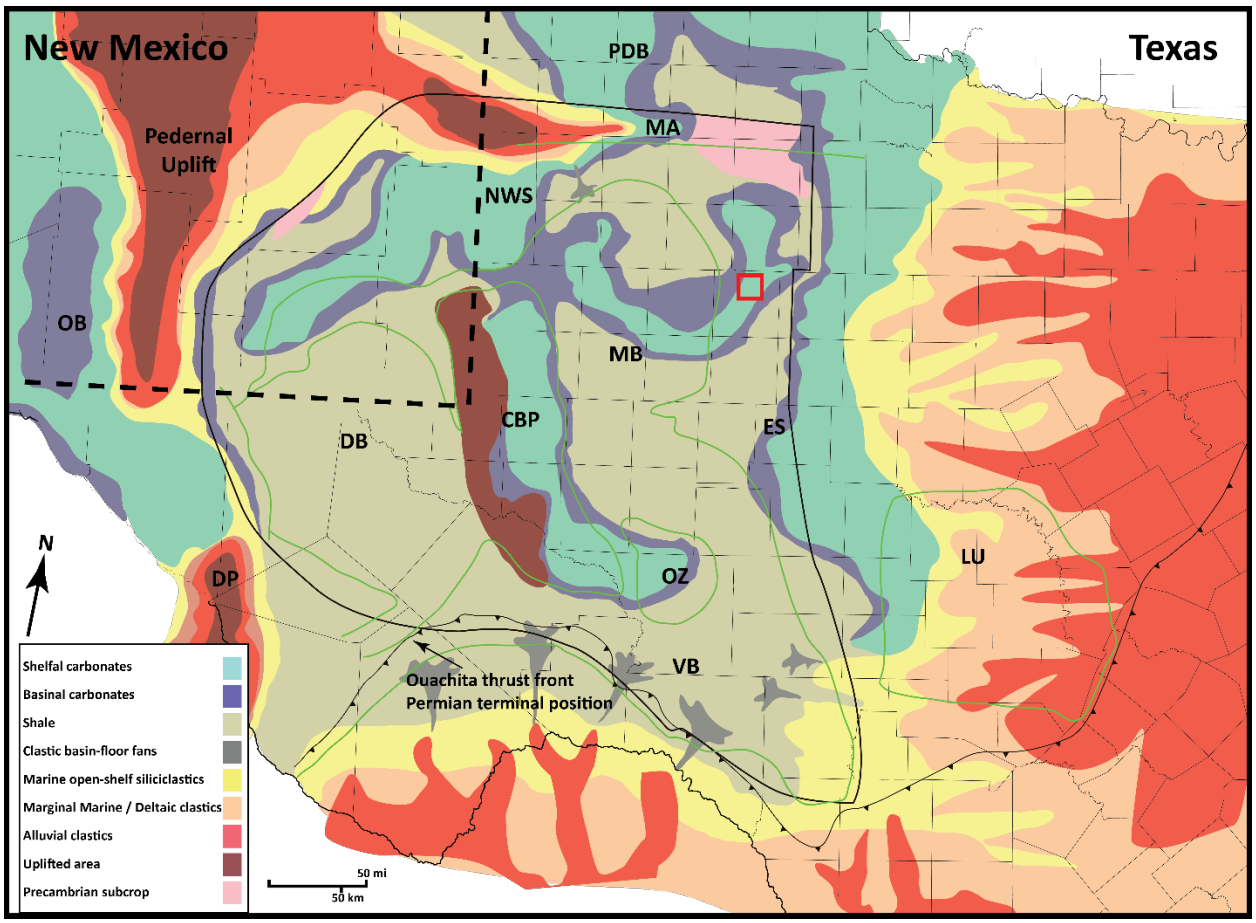


**Fig. 3.4**: Paleodepositional map of the Virgilian regional stage. The black envelope represents the Permian Basin; the green represents structural components differentiating the Permian Basin due to the Ouachita-Marathon Orogeny. Central Basin platform (CBP), Delaware Basin (DB), Diablo platform (DP), Eastern shelf (ES), Fort Worth Basin (FWB), Matador arch/uplift (MA), Midland Basin (MB), Northwest shelf (NWS), Orogrande Basin (OB), Ozona arch (OA), Palo Duro Basin (PDB), and Val Verde Basin (VB). The red square indicates the location of SACROC field on the Horseshoe Atoll. Map modified after Wright (2011).

The Horseshoe Atoll, which includes the SACROC producing unit, was differentiated from the surrounding basin floor in the Desmoinesian time (Strawn Formation) and then took on a classic wedding cake retrogradationally stacked pattern through the Virgilian (Vest, 1970; Waite, 1993). Eventually, the decreasing area of carbonate production, continued subsidence, and possibly clastic contamination led to the drowning of the Atoll in latest Pennsylvanian time with rapid encroachment of Wolfcampian shales (Dutton et al., 2005). Drowning of the larger atoll took place from east to west as easterly sourced turbidites lapped onto and overstepped the Salt Creek, Cogdell and SACROC field. However, producing units on the western side of the Horseshoe Atoll, e.g. Adair, remained shallow through the Wolfcampian (Vest, 1970).

## METHODS

### Sedimentology

SACROC field provides invaluable access to stratigraphic record that extends from the late Desmoinesian (Strawn Formation) all the way to the Virgilian (Cisco Formation). Available subsurface data represents the best place to assess the glacioeustasy during the late Pennsylvanian period in terms of total available data and greater preservation potential.

Twelve cored wells with a total coverage of 2,100 meters were described in detail (scale 1":10').Ten depositional lithofacies were defined using lithology, texture, grain size, sedimentary structures and fossil assemblages. In addition, a total of 146 thin sections were analyzed in detail for lithology, constituents, grain size, cements, porosity and porosity

types to supplement core descriptions. We used 1D sequence stratigraphic analysis to identify high-frequency cycles, cycle sets and high frequency sequences based on changes in depositional facies and stacking patterns (Fig. 3.5). Cored wells were then correlated across the field with the aid of fusulinid biostratigraphy (Schatzinger, 1983) and 800 wireline logs, which enables higher-confidence stratigraphic correlation (Fig. 3.6).

Most high frequency cycles stacking patterns show asymmetric, upward-shallowing trends inferred from (i) upward coarsening coupled with (ii) upward increase in sorting, (iii) grain type, (iv) sedimentary structures, (v) development of exposure horizons and (vi) changes in lithological attributes (Goldhammer et al., 1990; Kerans and Tinker, 1997; Read, 1998). Based on transgressive and regressive stacking, we identified and mapped 23 high frequency cycles in the Missourian Canyon Formation and 14 high frequency cycles in the Virgilian Cisco Formation.

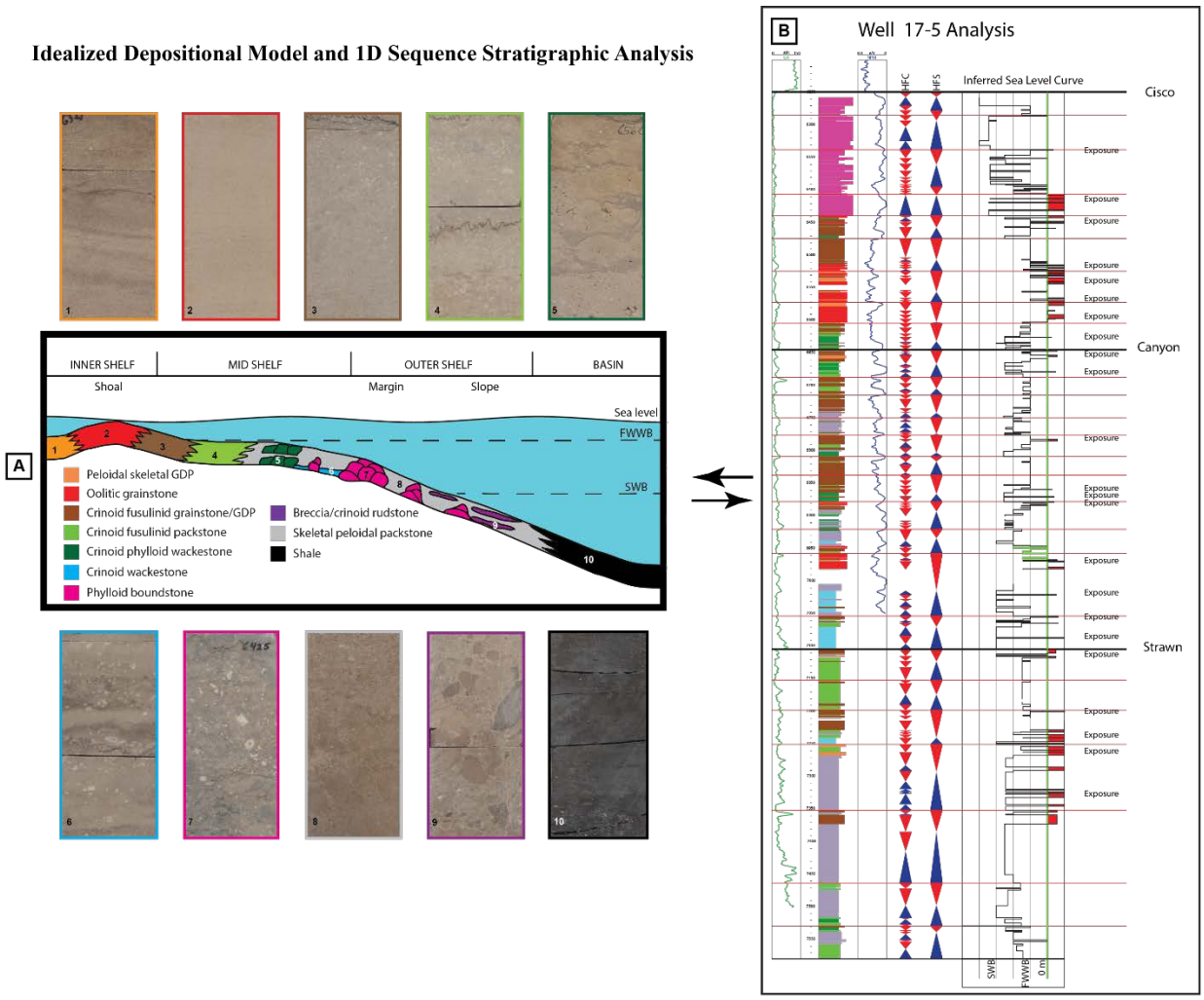


**Fig. 3.5**: A) Idealized depositional model for the Missourian Canyon and the Virgilian Cisco formations. Core photos represent each facies identified. B) 1D sequence stratigraphic analysis of one well (17-5) and inferred sea level curve based on changes of depositional facies through time. Adjustments to the idealized depositional as well as interpretation of depositional facies is an iterative process until the best Walterian model that honors the data is achieved.

**Constructing the Eustatic Curve**

Various workers have employed several methods and approaches in an effort to estimate/reconstruct eustatic curve for the Late Pennsylvanian. These approaches include high-resolution sequence stratigraphic analyses (Goldhammer et al., 1991; Smith and Read, 2001; Bishop et al., 2010; Martin et al., 2012, Dyer and Maloof, 2015), analyses of incised valleys (Howard and Whitaker, 1988; Goldstein, 1988; Rankey et al., 1999; Feldman et al., 2005), analysis of diagenetic fabrics below exposure surfaces (Goldstein, 1988) and stable isotopes geochemistry analyses ($\boldsymbol{\delta}^{18}O$, $\boldsymbol{\delta}^{13}C$ , $\boldsymbol{p}CO_2$) (Adlis, 1988; Joachimski et al., 2006; Montañez et al., 2007; Dyer and Maloof, 2015; Montañez et al., 2016). In order to reconstruct a eustatic curve, we employed the following concept: changes in relative sea level (related to waxing and waning of ice sheets) are associated with changes in lithofacies and stacking patterns (Wanless and Shepard, 1936; Crowell, 1978; Donovan and Jones, 1979). Inferred water depths from depositional lithofacies and development of exposure surfaces were used to estimate eustatic fluctuations from each well. Inferred water depths are estimated based on lithology, texture, sedimentary structures, grain types and fossil assemblage as well as comparing them to modern and ancient analogs. For example, in a single shallowing upward high frequency cycle, eustatic change is estimated as the difference in inferred water depths between the deepest lithofacies at the base of the high frequency cycle and the shallowest lithofacies capping it. If an exposure surface is developed capping the high frequency cycle, we add how far down

the exposure penetrates to the eustatic change. Our approach does not rely on data from 1D, but we utilize all available core data to minimize biased eustatic signals caused by missed beats (Goldhammer et al., 1990).

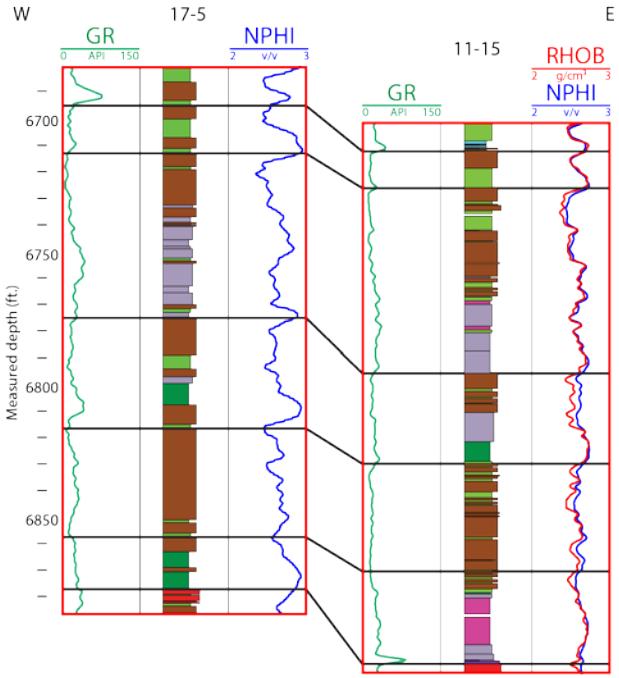


**Fig. 3.6**: Correlation panel illustrating the approach taken in this study to correlate between wells utilizing core and wireline logs. Facies colors are the same as in Fig. 3.5.

Several steps were taken to construct a composite sea level curve for the late Pennsylvanian. First, we construct eustatic curve for each well based on changes of estimated water depths inferred from depositional lithofacies at the base and top of each depositional cycle (Fig. 3.5). Then we use stratigraphic information along with wireline logs to correlate between wells establishing mappable timelines (Fig. 3.7). Missed beats

appear as additional, non-mappable cycles in some of the wells between established timelines between all control points (i.e. cored wells). The composite eustatic curve is created based on average sea level rise or fall calculated as an average value (Fig. 3.7) whereas missed beats are averaged among the wells they are encountered and then are added to as part of the composite curve in their stratigraphic position.

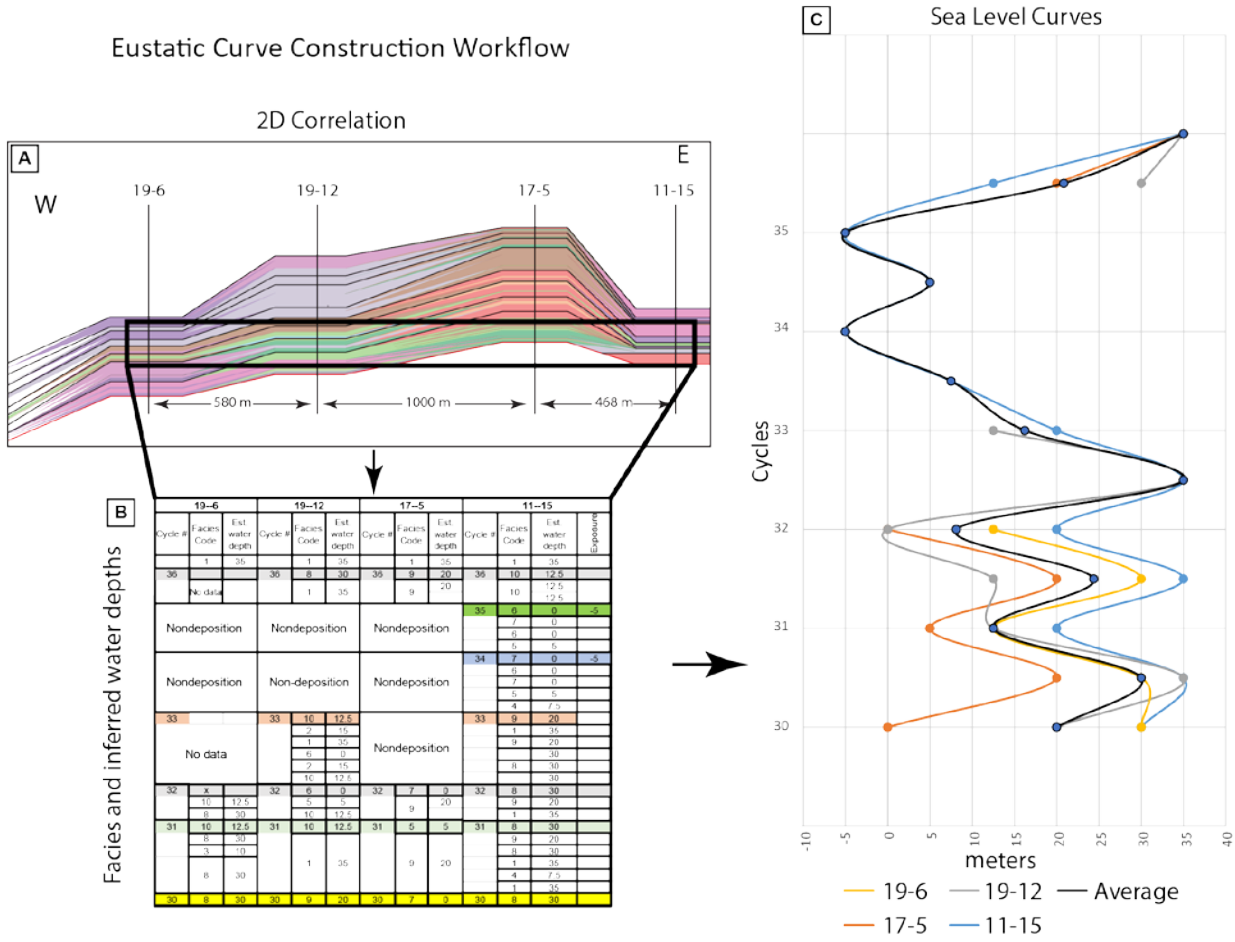

**Fig. 3.7**: Workflow for constructing eustatic curve from 2D approach. (A) 2D seuqence stratigraphic framework is constructed based on correlation of cored wells utilizing wireline logs. (B) Tabulated estimated water depth from depositional facies for each depositional cycle. Blank boxes represent intervals with no recovery (no data) or periods of nondeposition (i.e. missed beats). (C) Constructed composite eustatic curve (black) calculated as an average from different sea level curves constrcuted for individual wells. Missed beats are added to the composite curve based on their stratigraphic position. Negative values represent the depth of penetration of subaerial exposure features below cycle top.

## Depositional Lithofacies

The Missourian Canyon Formation and the Virgilian Cisco Formation are divisible into ten main depositional facies that form five facies associations reflecting depositional environments (Table 3.1). Facies associations include: basin, outer shelf, middle shelf, inner shelf and shoal complex.

## Basin Facies Association

### *Shale*

Shale beds are dark grey to black in color, weakly calcareous in parts (<10%), pyritic in parts, finely laminated and fissile with generally sharp top and basal contacts.

Thickness of shale units, when preserved, ranges from few centimeters to 1.5 meters. Sometimes, shale is interbedded with crinoid-rich beds, especially towards the top of Cisco carbonates. In some instances, the laminations of the shale show horizontal disruption interpreted as cryptic bioturbation. Shale is devoid of carbonate allochems except rare reworked disarticulated brachiopods and crinoid fragments with variable grain-size. Pyrite deposition and limited to absent biodiversity, suggests that shale has been deposited in a stressed, anaerobic and reducing intrashelf basin (Schieber and Baird, 2001). Shale interfingers with buildup flank facies and eventually covers the entire platform. Water depth at which shale was deposited has been assigned arbitrarily to 35 meters as a conservative estimate even though similar shale has been reported to have been deposited between 70 (Tourtelot, 1979; Adlis et al., 1988) and 100 m (Heckel,1977).

| | Facies | Sedimentary Structures | Thickness | Grain size | Sorting | Grain types | | Depositional Environment | Water depth |
|---|---|---|---|---|---|---|---|---|---|
| | | | | | | *Non-skeletal* | *Skeletal* | | |
| Deeping | Shale | Finely laminated, fissile, sharp basal and top contacts, cyptic biotrubation | Few centimeters up to 1.5 m | Mud/silt | | | | Basin | +35 m |
| | Crinoidal Rudstone | | 30 cm - 4 m | fine to granular | Poorly | Peloids | mainly crinoids, minor: brachipodos, bryozoan, fuulinid, agglutinated forams, phylloid plates | Outer shelf/slope apron | +30 m |
| | Phylloid boundstone | Bioturbation | 2 m - 25 m | fine to granular | Poorly to moderately | Peloids | mainly phylloid algal plates, crinoids minor: fusulinids, fenestrate bryozoans, brachiopods, agglutinated foraminifera sponge spicules.rugosan corals, stromatoporoids | Outer shelf/margin | 20-150 |
| | Crinoidal Wackestone | | 1.5 m - 10 m | medium to granular | Poorly | Peloids | mainly crinoid ossicles rare: bivalve, foraminifera, sponge spicules | Middle shelf | 15-25 |
| | Crinoid Phylloid Wackestone | Bioturbation, stylolitization | 30 cm - 6 m | fineto granular | Poorly to moderately | Peloids | mainly phylloid algal plates and crinoids rare: fusulinids, agglutinated foraminifera, sponge spicules | Middle shelf | 5-25 |
| | Skeletal Peloidal Packstone | Bioturbation | 30 cm - 8 m | fine to coarse | Moderate to poorly | Peloids | mainly phylloid algal plates, crinoids, fusulinids. minor: agglutinated foraminifera, sponge spicules | Middle shelf | 5-25 |
| | Crinoid-Fusulinid Packstone | Bioturbation | 30 cm - 6 m | fine to granular | Moderate to poorly | Peloids grapestones | mainly crinoids, fusulinids minor: brachiopods, agglutinated foraminifera | Inner shelf | 5-20 |
| | Crinoid-Fusulinid Grainstone | Cross and parallel stratification, biotrubation oblitrating stratification | 30 cm - 8 m | coarse to very coarse | Moderately sorted | Peloids | mainly crinoid stem segments, fusulinids minor: agglutinated formainifera, algal plates | Inner shelf | 5-15 |
| | Skeletal Peloids Grainstone | Low-angle planar lamination, bioturbation, calichification | 30 cm - 6 m | fine to medium | Well to moderate | Peloids | minor: crinoids, fusulinids, agglutinated foraminifera | Shoal | 0 - 5 |
| | Oolitic Grainstone | Cross stratification, calichification | 30 cm - 12 m | fine to medium | well-sorted | Ooids coated grains | minor: crinoids, bivalves and gastropods | Shoal | 0 - 5 |

**Table 3.1**: Lithofacies of the Late Pennsylvanian in SACROC field.

## Outer shelf Facies Association

### *Slope: Crinoid Rudstone*

Crinoid rudstones consist of units that are between 30 cm and 4 m in thickness with a packstone matrix. Rudstones are almost entirely composed of crinoids with accessory allochems including brachiopods, bryozoans, fusulinids and other agglutinated foraminifera, phylloid plates, and bivalves (Fig. 3.8g). Carbonate mud is common within the rudstones, but sometimes it increases significantly that crinoid grains are floating in a muddy matrix that can be classified as floatstone (Embry and Klovan, 1971). In some cases, intraclasts of algal origin dominate the floatstones within skeletal packstone matrix. Crinoid rudstones are poorly sorted with a grain-size range from fine-grained to granule-sized grains that in some cases show normal grading. The lower contact of the crinoid rudstone dips between $15^{o}$ to $35^{o}$ from horizontal. Crinoid rudstones are first recorded in the wells located on the flanks of the platform especially at the end of the Missourian when phylloid mounds become more abundant. The poor sorting, the normal grading and relatively steeply dipping lower contacts suggest that crinoid rudstones were deposited as slope apron of moderate- to high-energy platform and marginal environments below a storm wave base (Playton et al., 2011).

### *Shelf margin: Phylloid Boundstone*

Phylloid boundstones can be composed of a highly diverse faunal assemblage or, in some instances, can be monospecific phylloid algal plates (Fig. 8f). The matrix of the

boundstone can range from bioturbated wackestone to packstone that may contain up to 20% peloids and up to 15% dolomite. The boundstones are poorly- to moderately-sorted with a grain size that ranges from fine-grained to granule-sized. Aragonitic platy and cup-shaped growth forms of phylloid algae are noted and are identified as Eugonophyllum sp. (Schatzinger, 1988). Crinoids are the second most common biocomponent associated with the phylloid algae. Fusulinids, fenestrate bryozoans, brachiopods, agglutinated foraminifera and sponge spicules are also found in this facies. In rare cases, reworked solitary rugose corals, stromatoporoids and sponges are observed.

The phylloid boundstones have limited lateral continuity with thicknesses that range from 2 to 25 m suggesting biohermal growth pattern (Toomey, 1991). Further, the morphological similarities between Eugonophyllum and modern green algae Halimeda and Udotea (Kirkland et al., 1993) suggests similar depositional environment. Thus, the phylloid buildups are interpreted to have formed within the photic zone at water depths that range from 20 to 150 m (Freile et al., 1995) under moderate energy and good water circulation at and above storm wave base. We used the minimum water depth at which this facies is found, i.e. 20 m, to estimate eustatic change.

**Middle Shelf Facies Association**

***Crinoidal Wackestone***

Beds of crinoidal wackestone consist of crinoid ossicles and rare bivalve, foraminifera, and sponge spicules. The crinoids have various grain sizes commonly range from medium-sized to granule-sized and are sometimes fragmented and abraded (Fig. 8h).

These units range in thickness from 1.5 m and up to 10 meters. Crinoidal wackestones are more common in the Strawn unit and become less important in the Canyon/Cisco formations. The muddy matrix of the crinoidal wackestone suggests low energy settings with episodic events bringing reworked crinoid fragments into the site of deposition. These are interpreted to form at the leeside of phylloid algal mounds where minimum energy conditions predominate (Gischler, 1995; Smithers and Larcombe, 2003).

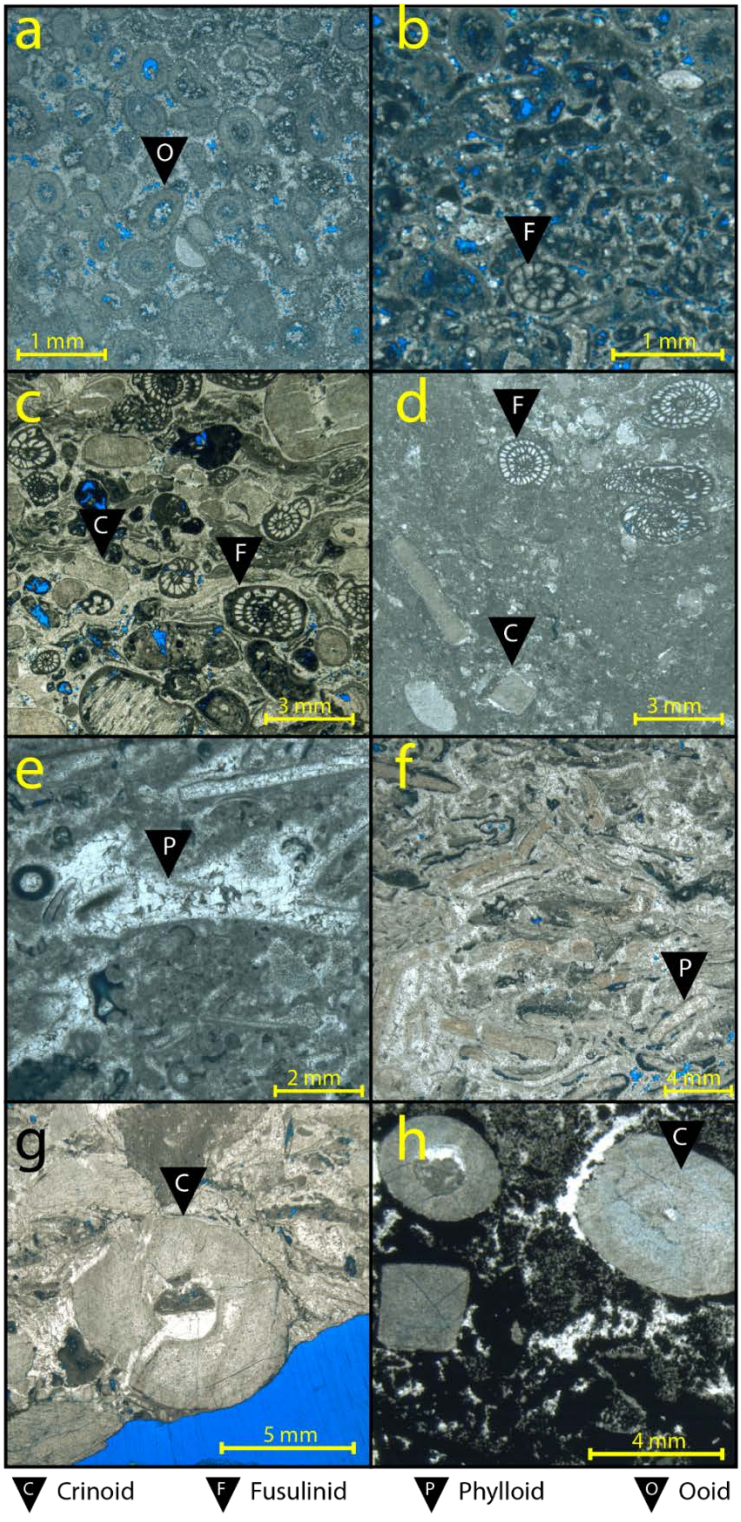
a
O
1 mm
b
F
1 mm
c
C
F
3 mm
d
F
C
3 mm
e
P
2 mm
f
P
4 mm
g
C
5 mm
h
C
4 mm
C Crinoid
F Fusulinid
P Phylloid
O Ooid

**Fig 3.8**: photomicrographs of depositional facies within the SACROC. The facies include: a) ooid grainstone, b) peloid-skeletal grainstone, c) fusulinid-crinoid grainstone, d) fusulinid-crinoid packstone, e) peloid-skeletal packstone, f) phylloid boundstone, g) crinoid rudstone, and h) crinoid wackestone. Abbreviations: (C) Crinoid, (F) Fusulinid, (P) Phylloid, and (O) ooids.

### *Crinoid Phylloid Wackestone*

Crinoid phylloid wackestone to packstones form 30 cm to 6 m thick units and consist of muddy peloidal matrix in which dispersed algal plates and crinoid columnals constitute up to 60% of the biocomponents. Other skeletal allochems include fusulinids, agglutinated foraminifera and sponge spicules. Bioturbation and stylolites are the main sedimentary structure observed in the crinoid phylloid wackestone. Although, the texture and composition are comparable to the phylloid boundstone, the crinoid phylloid wackestones do not appear to form higher relief boundstones but rather biostromal deposits. Crinoid phylloid wackestones may represent incipient mound facies or small skeletal banks formed in intermound areas. The muddy texture of these wackestones suggests deposition under low- to moderate-energy settings, above storm wave base, and the presence of crinoids suggests normal marine conditions.

### *Skeletal Peloidal Packstone*

Skeletal peloidal packstones consist of a mixture of non-skeletal grains, mainly peloids, and skeletal allochems. The skeletal allochems are predominantly phylloid algal plates, crinoids and fusulinids with minor assemblages of agglutinated foraminifera and sponge spicules (Fig. 3.8e). In general, these packstones are bioturbated, fine- to coarse-grained, moderately- to poorly-sorted and form units that range in thickness between 1 and 12 meters. During the Viriglian, when phylloid mounds become more dominant, skeletal peloidal packstones become much more abundant which suggests their association with phylloid buildup growth. The packstone texture suggest moderate energy conditions

allowing the winnowing of muddy and finer particles and thus were deposited above storm-wave base. Skeletal peloidal packstone is interpreted to represent “algal meadows” in intermound areas (Schatzinger, 1988). The term “algal meadows” (Orme et al., 1978; Drew and Abel, 1985) is used to describe dense patches of Halimeda at depths greater than 20 m in lagoons and on slope break.

## Inner Shelf Facies Association

### *Crinoid-Fusulinid Packstone*

Crinoid-fusulinid packstones consist of units that are 30 cm to 6 m thick and are composed mainly of crinoids and fusulinids that make up to 30 to 40% of this facies’ volume (Fig. 8d). Minor constituents include brachiopods, agglutinated foraminifera, peloids and grapestones. Crinoid-fusulinid packstones are moderately- to poorly-sorted with grain size range from fine-grained to granule-sized. Sedimentary structures include low angle planar stratification that is commonly obliterated by burrows. Texture and sedimentary structures suggest that this facies was deposited in relatively high-energy settings removing much of the finer material, but yet not high enough to impede burrowing organisms by burial or constant agitation. Thus, this facies is interpreted to have formed below fairweather wave base and above storm wave base.

### *Crinoid-Fusulinid Grainstone*

Crinoid fusulinid grainstone and grain-dominated packstone are composed primarily of crinoid stem segments and fusulinids (Fig. 3.8c) with accessory allochems including peloids, agglutinated foraminifera and reworked phylloid plates. In general, grainstone units show well-preserved cross stratification and parallel lamination; however, bioturbation may obscure stratification causing units to appear massive. Grainstones are moderately sorted, generally coarse- to very coarse-grained with unit thicknesses ranging from 30 cm to 8 meters. The texture, sorting, grain-size trends and stratifications indicate that the crinoid fusulinid grainstones were deposited at high-energy energy settings at or near fairweather wave base.

## Shoal Facies Association

### *Skeletal Peloids Grainstone*

Skeletal peloidal grainstones and grain-dominated packstones consist of 30 cm to 6 m thick units of well- to moderately-sorted, fine- to medium-grained peloids, occasionally with larger skeletal allochems (Fig. 3.8b). Skeletal allochems can constitute as much as 30% of the total volume of this facies and include crinoids, fusulinids and agglutinated foraminifera. The grainstones sometimes show low angle planar lamination and can be homogenized as a result of extensive burrowing activity. These grainstones are

interpreted to be deposited under shallow, high-energy conditions at the leeside flank of ooid shoals.

### *Ooid Grainstone*

Ooid grainstones consist mainly of well-sorted, fine- to medium-grained ooids and coated grains (Fig. 3.8a) that range between 30 cm and 12 m in thickness. Accessory skeletal allochems can constitute up to 20% of the total volume of this facies and include crinoids, bivalves and gastropods. Oolitic grainstones are generally cross-stratified and show well-preserved calichification resulting from subaerial exposure. Thus, ooid grainstones are interpreted to had deposited in shallow-water, high energy shoals. Analogous to modern carbonate depositional environments, the oolitic shoal deposits occur in water depths that are less than 5 m and can build up to sea level.

## DISCUSSION: LATE PENNSYLVANIAN GLACIATION

### Late Pennsylvanian Eustatic Curve

Shallow water carbonates are one of the better proxies for estimating shallowing or deepening trends of relative sea level (Osleger and Read, 1991) as fairly precise water depths can be inferred from depositional facies. The principle assumption is that accommodation space created with each sea level rise is completely filled and thus the cycle thickness is a measure of relative sea level change (Fischer, 1964; Read and Goldhammer 1988). This means it is possible to reconstruct past relative sea level curves

based on the change in inferred water depth from lithofacies at the base and top of each high frequency cycle. Nonetheless, the assumption that accommodation space is completely filled is not entirely correct (Boss and Rasmussen, 1995), as there is more time in hiatus intervals of the stratigraphic record compared to intervals with rock recorded. In addition, 'missed beats" bring about further complication and they can be caused by: (i) unfilled available accommodation space, (ii) sea level fluctuations below the platform top and away from control points, or (iii) a combination of the two. Unfilled accommodation space creates uneven depositional topography which produces depositional cycles with variable thicknesses that may be enhanced by different sedimentation rates as well as erosional profiles created by energy regime and distribution across the platform. According to carbonate production data from the Holocene in Florida Bay, carbonate sediment produced can fill 1.5 to 3 times the available space, however, off bank transportation of sediment, controlled by energy distribution across the platform, results in unfilled accommodation space (Eberli, 2013). The stratigraphic record from shallow water carbonates is prone to 'missed beats' when sea level falls and fluctuates below the platform top which results in depositional cycles that are not recorded on the platform (Goldhammer et al., 1990). Additionally, uncertainties associated with estimating water depth from depositional facies are minimal for shallow water, high-energy carbonates, whereas uncertainties for all other depositional facies can be large (Eberli, 2013). For example, phylloid algae, which are related to modern green algae Halimeda and Udotea (Kirkland et al., 1993), could exist in water depths that range from 20 m and up to 150 m (Freile et al., 1995). A further complexity arises from the assumption that the stratigraphic section and

cycle thickness did not experience any removal. Nonetheless, during lowstands of sea level when the platform top is subaerially exposed, extensive meteoric diagenesis may occur, including karstification and calichification, which may cause the removal of significant section of the depositional cycle. Likewise, removal of stratigraphic section may also occur during transgression. Due to the aforementioned reasons, several uncertainties may be encountered and should be considered when reconstructing past relative sea level curve from 1D measured section. To minimize these uncertainties, we used a 2D approach where several data points, for the same interval, are used to reconstruct a composite eustatic curve (cf. Bishop et al., 2010) for the late Pennsylvanian (Fig. 3.9).

The reconstructed sea level curve for the late Pennsylvanian from the SACROC data (Fig. 3.9f) supports the dominance of high-frequency, high amplitude sea level fluctuations that typify icehouse settings during the Missourian and Virgilian stages (Read, 1995). Based on depositional lithofacies, the minimum eustatic amplitude inferred from high frequency sequences is 37 m, whereas higher order cycles within the high frequency cycles suggest a minimum amplitude of 15 m. Cycles are defined as genetically related strata bounded at the base and the top by unconformable surfaces or their landward and basinward correlative conformities (Van Wagoner et al., 1990). Cycles are defined utilizing sequence stratigraphic analyses (Kerans and Tinker, 1997). These analyses include: a) recognition of subaerial exposure surfaces (mostly marked by calichification), b) lithofacies tract offset c) cycle symmetry, and d) changes in cycle thickness and lithofacies proportions. The Missourian Canyon Formation consists of 23 high-frequency, high-amplitude, grainstone-capped cycles. These cycles are dominated by aggradational to

progradational stacking patterns, many of which show well-developed, exposure-related features defining their upper surfaces. Marginal wells and wells located in low topographic position on the platform show lowstand packages that would have been otherwise “missed-beats” if limited data points were considered on the platform top. The duration of the Missourian is estimated to last about 2.3 Ma (Gradstein et al., 2012) which suggests that the average period of the high frequency cycles is 100 ka implying the dominance of short-term eccentricity signals that typify icehouse conditions (Goldhammer et al., 1990; Wright, 1992; Read, 1995).

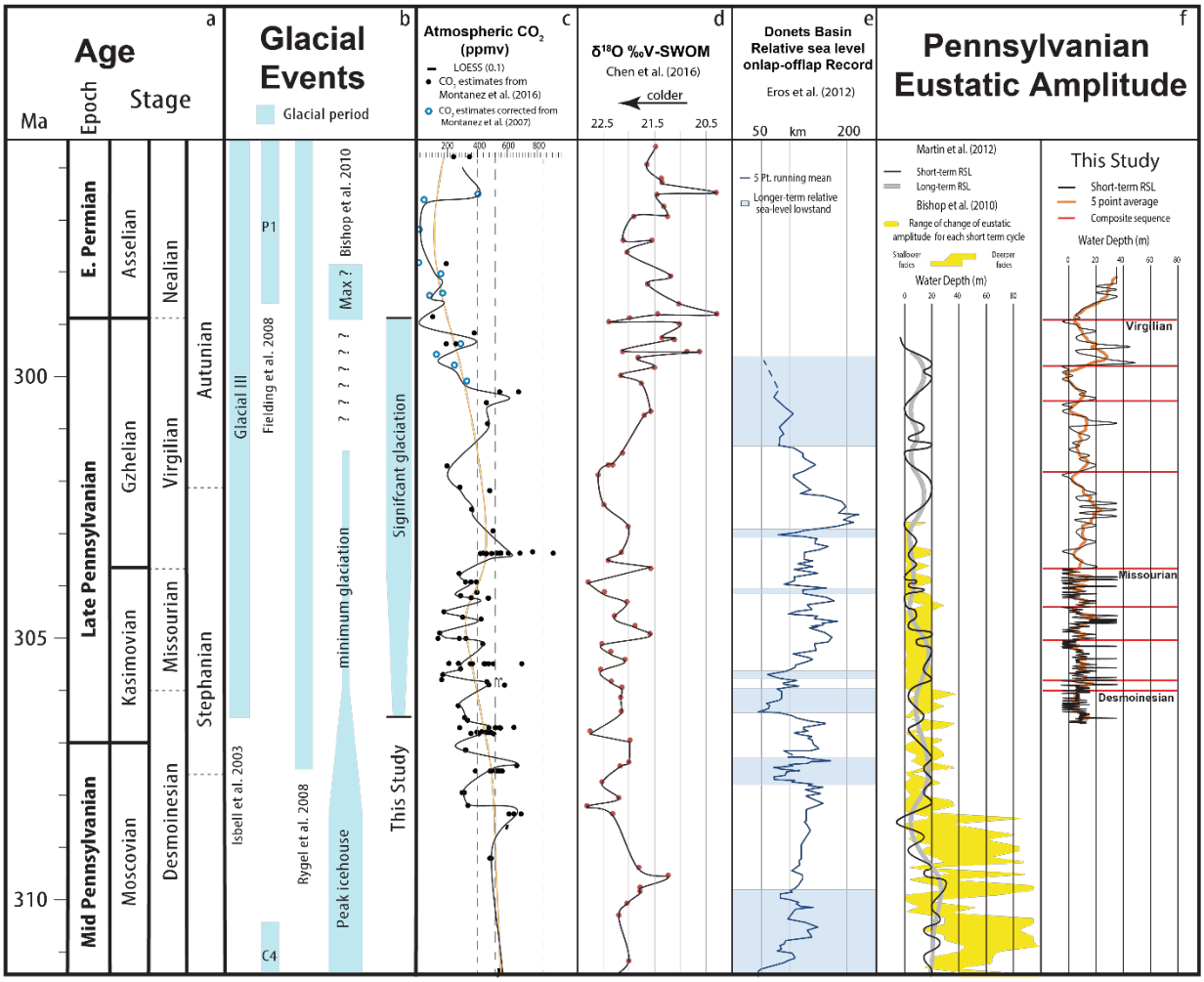

**Fig. 3.9**: Synthesis diagram of the late Pennsylvanian. (b) Recognized glacial events by different authors. The limit of our data, black lines, suggests a glacial events extending from the Missourian to the latest Virgilian. This glacial period is recognized by several authors. (c) Estimated $pCO_2$ (averaged) for the late Pennsylvanian (Montanez et al., 2016); dashed lines are $pCO_2$ 420, 560 and 840 ppm (right to left) and represent glaciation threshold; $pCO_2$ < 420 ppm = stable glaciation + glacial advance; $pCO_2$ <560 ppm=interglacial; $pCO_2$ >840=ice-free conditions (Horton et al., 2012). Most of the record suggests a dominance of glaciations. Previously published data (Montanez et al., 2007) of $pCO_2$ (blue circles) were corrected and thus suggest a cooler settings that initially predicted. (d) $\delta^{18}O$ curve from Naqing section, south China shows enrichment of about 1‰ in $\delta^{18}O$ during the Missourian and Virgilian which suggest significant glaciation that can be as big as the Pleistocene (e) The Donets Basin coastal onlap curve (Eros et al., 2012) where long-term sea level lowstands (shaded blue) coincide with increased glaciation resulting in the drawdown of sea level. (f) Our composite eustatic curve for the Late Pennsylvanian (black) using high-frequency cycles; orange curve represents 5-point moving average of the composite eustatic curve; red lines represent composite sequences. Water depths on the horizontal axis are assigned based on the inferred water depth for each depositional facies. The Missourian is characterized by high-frequency (short-term eccentricity), high amplitude eustatic fluctuations. The Virgilian

shows a lower frequency (long-term eccentricity) and a larger amplitude captured only by lateral juxtaposition of shallower and deeper facies. Our eustatic curved shows high frequency, high amplitude eustatic fluctuation during late Pennsylvanian is compared to eustatic curve from Bird Spring Formation (Bishop et al., 2010; Martin et al., 2012). Time-scale after Gradstein et al., 2012.

The Virgilian Cisco Formation is composed of 14 high frequency cycles that show a general retrogradational stacking patterns. Strong eustatic fluctuations caused the carbonate factory to be shut down and only shallower parts of the platforms were able to reestablish carbonate sedimentation. High sea level rise resulted in several cycles recorded only at shallower, specifically crestal, areas as well as non-sedimentation and/or non-resolvable cycles in the deeper parts of the carbonate shelf/basin. The cycles developed on the shelf interior at this time are referred to as "catch-up" (Kendall and Schlager, 1981) cycles, where phylloid mounds grew in the shelf interior during the early stage of platform drowning. In addition, strong sea level fall may have no record at one location but may be recorded in another (Fig. 3.7). Thus, facies juxtaposition and using the 2D approach to estimate eustatic amplitude is a better approach than the 1D approach. The 1D from only one well (17-5) may suggest a pulsed sea level rise, but including another well (11-15) we realize, the sea level rise was followed by a significant sea level fall that would never have never been recognized if traditional 1D approach is used. As phylloid boundstone stepped back into platform interior during to catch-up, they reached a thickness of 25 meters

indicating significant sea level rise. This was followed by a remarkable sea level fall where highly calichified shoal complex grainstones were lapping out onto the base of the backstepped phylloid mound. If we assume that the phylloid mound formed at minimum water depth ~ 20 m, the onlapping shoal facies found at the base of the phylloid mound formed at sea level, this implies a minimum eustatic fluctuation of 45 m. This is not considering the exposure develop within the shoal complex grainstones, where fall may have been as much as 50 m considering the depth of exposure related calichification. Hence, we infer a much stronger eustatic amplitude during the Virgilian compared to the Missourian. The average duration of each HFC during the Virgilian is estimated around 343 ka which proposes the dominance of long-term eccentricity.

## Comparison to other datasets

### *Sedimentology*

The early view considering the Late Paleozoic Ice Age (LPIA) as one, protracted glaciation event (e.g. Veevers and Powell, 1987; Frakes et al., 1992; Crowell, 1999) has changed significantly in recent years. Isbell et al. (2003) compiled and reviewed global datasets from across Gondwana and determined that the LPIA can be divided into three glacial periods separated by non-glacial conditions. Based on these records, the latest Pennsylvanian was dominated by glacial terrestrial, glaciolacustrine and glaciomarine deposits which indicates extensive glaciation. Fielding et al. (2008) claimed that these intervals can be further resolved into eight discrete glacial events (four in the Carboniferous

and four in the Permian) separated by non-glacial conditions. Nonetheless, they described the latest Carboniferous (Late Moscovian to Pennsylvanian-Permian boundary) as non-glacial period dominated by greenhouse conditions. This claim was based on data from Joe Joe Group (mid-Desmoinesian- latest Gzhelian) in Galilee Basin of eastern Australia (Jones and Fielding, 2004; 2008). They argued that the Joe Joe Group was composed of thick fluvial and lacustrine facies with no evidence of glacial influence during the Late Pennsylvanian (Jones and Fielding, 2004). However, several authors have noted that the Jochmus Formation of the Late Pennsylvanian is composed of fluvial and lacustrine deposits that show strong glacial influence (Días et al., 1983; Hambrey, 1981). Additionally, our results, from SACROC field, shows that the Late Pennsylvanian (latest Desmoinesian – Virgilian) was a time of extensive glaciation resulted in high-frequency, high-amplitude eustatic fluctuations. Our estimated minimum amplitude (37 to more than 45 m) of eustatic change, advocates that the late Pennsylvanian represents icehouse conditions. Our results agree with early workers supporting glacial conditions of the late Pennsylvanian (Heckel, 1977, 1994; Goldstein, 1988; Adlis et al., 1988; Crowley and Baum, 1991; Raatz and Simo, 1998; Soreghan and Giles, 1999; Isbell et al., 2003; Feldman et al., 2005; Bates and Lyons, 2006; Joachimski et al., 2006) but contradicts with the conclusion that the late Pennsylvanian was a non-glacial interval (Table 3.2) (Fielding et al., 2008; Bishop et al., 2010; Martin et al., 2012).

The earliest studies of mid-Desmoinesian to Virgilian Midcontinent cyclothems showed exposure surfaces juxtaposed with phosphatic black shales suggesting a minimum of 100 m sea level change (Heckel, 1977, 1986, 1994). Klein (1994) used Midcontinent

cyclothems from Heckel's work and corrected for compaction and subsidence and estimated glacioeustatic magnitude of 48 to 147 m for the Missourian and 21 to 71 m for the Virgilian. The transgressive system tracts of the Beeman Formation (Missourian-Early Virgilian) of Dry Canyon (Raatz and Simo, 1998) shows exposure surfaces overlain by transgressive lags and thin transgressive carbonates followed by offshore shale. The highstand system tracts show thick, restricted carbonates deposits punctuated by numerous subaerial exposure surfaces. The high-frequency sequence development observed in the Beeman Formation is interpreted to be the result of high-amplitude, high-frequency glacioeustatic sea level variations with absolute sea level ranging between 70 and 170 m. Further, preserved relief on ancient subaerial exposure surfaces of large algal bioherms in the Virgilian Panther Seep Formation in western Orogrande Basin suggest that the minimum amplitude of eustatic change was ~80 m and probably exceeded 100 meters (Soreghan and Giles, 1999).

Glacioeustatic sea level variations for the Late Pennsylvanian have, also, been inferred from erosional relief during lowstands of sea level (i.e. incised valleys) preserved in the rock record. The Hardinville paleovalleys of Carboniferous age formed along the LaSalle Anticline in Illinois recorded a maximum of 60 m of incision (Howard and Whitaker, 1988) and were attributed to falling sea level (Rygel et al., 2008). The late Desmoinesian paleovalley between the Danville coal and West Franklin Limestone in Illinois Basin shows at least 60 m of incision driven primarily by glacioeustasy (Heckel et al., 1998). Feldman et al. (2005) showed several high-frequency sequences from the Missourian-Virgilian US Midcontinent cyclothems where incised valley fill developed

during lowstands of sea level. The earliest Missourian shows 10 m of incision while the mid-Missourian to mid-Virgilian shows between 20-40 m of incised valley fill overlain by deeper water shales suggesting that sea level amplitude was at least 40 m. Erosional relief estimates from the Holder Formation in Sacramento Mountains suggest that glacioeustatic fluctuation ranged between 30s and up to 50 m (Goldstein, 1988).

When our data are compared to onlap-offlap data from the Donets Basin (Eros et al., 2012) they show a consensus of long-term stepwise rise through the early Virgilian upon which shorter term lowstands are superimposed (Fig. 3.9e). Significant lowstand appears to have existed in the late Pennsylvanian in the Donets Basin coinciding with significant shallow water and deep water facies juxtapositions observed in the SACROC, indicating a significant glaciation and drawdown of sea level. The advantage of our data is that it provides a wide range of control points from shelf to basin (cf. Bishop et al., 2010) across a narrow shelf (cf. Martin et al., 2012). In shelfal areas, large sea level falls may or may not be associated with the development of exposure-related features. If exposure features were developed during sea level fall, assessment of how far sea level fell can only be arbitrary unless time-equivalent depositional records were available in slope and basinal positions. When assessing climatic signal from high-frequency stratigraphic record, missed beats recorded off the shelf and precise correlation between wells utilizing wireline logs give longer and high-fidelity eustatic record than widely spread and/or confined records to shelfal areas.

**Summary of studies and methods used to estimate the glacioeustatic amplitude in the Late Carboniferous**

| Author | Year | Area | Sedimentology | | | Diagenesis | Geochemistry | Computer Modeling | Amplitude of SL fluctuations |
|---|---|---|---|---|---|---|---|---|---|
| | | | 3D | 2D | 1D | | | | |
| Heckel | 1977 | Midcontinent cyclothems | | | | | | | ~100 m |
| Goldstein | 1988 | Holder Formation, Sacramento Mountains | | | | | | | 30-50 m |
| Adlis et al. | 1988 | Necessity Shale, CBP/Fort Worth Basin | | | | | $\delta^{18}O$ | | 70 m |
| Crowley & Baum | 1991 | Global distrbution of glacigenic deposits | | | | | | ICE | 60±15 m<br>105±15 m<br>170±20 m |
| Heckel | 1994 | Midcontinent cyclothems | | | | | | | ~100 m |
| Goldhammer et al. | 1994 | Paradox and Honker Trail Formations, Utah | | | | | | Mr. Sediment | 25-33 m |
| Raatz & Simo | 1998 | Beeman and Holder, Sacramento Mountains | | | | | | | 70 - 170 m |
| Heckel et al. | 1998 | Danville coal and West Franklin Limestone | | Paleovalleys | | | | | ~100 m |
| Soreghan and Giles | 1999 | Panther Seep, Orogrande Basin | | | | | | | 80-100 m |
| Rankey et al. | 1999 | Holder Formation, Sacramento Mountains | | +Palcovalleys | | | | | 3 - 32 m |
| Isbell et al. | 2003 | Global distrbution of glacigenic deposits | | | | | | updated ICE | 50.6 to 86 m<br>67.5 to 114.6 m |
| Feldman et al. | 2005 | Midcontinent cyclothems | | Paleovalleys | | | | | 2-41 m |
| Bates and Lyons | 2006 | Midcontinent cyclothems | | | | | $\delta^{18}O$ | | 55-155 m |
| Joachimski et al. | 2006 | Midcontinent cyclothems | | | | | $\delta^{18}O$ | | +120 m |
| Fielding et al. | 2008 | Eastern Australia, distribution of glaciogenic deposits | | | | | | | <30 m |
| Bishop et al. | 2010 | Arrow Canyon, Nevada | | | | | | | 5-20 m |
| Martin et al. | 2012 | Spring Formation | | | | | | | < 20 m |
| This study | | Canyon and Cisco, Midland Basin | | | | | | | +37 m |

Greenhouse (RSL ≤ 10 m) Transitional (10 m ≤ RSL ≤ 40 m) Icehouse (RSL ≥ 40 m)

**Table 3.2**: Summary of different studies (arranged in chronological order) aimed to pin point the amplitude of eustatic fluctuation in the Late Pennsylvanian. Colored boxes reflect climate settings interpreted for the Late Pennsylvanian by different authors. Different studies utilized different approaches including sedimentology, diagenesis, geochemistry, and computer models (name of modeling software in box) sedimentology are mainly 1D (vertical analysis of stacked facies) and 2D (vertical and lateral facies stacking including incision by paleovalleys). Geochemistry-based estimates utilized oxygen isotopes as a proxy for glaciation.

### *Stable isotopes*

Stable isotopes analyses have long been used in several paleoclimate studies in which oxygen isotopes ($\boldsymbol{\delta}^{18}O$) and concentration of atmospheric carbon dioxide ($\boldsymbol{p}CO_2$) are among the most used proxies (Cheng et al., 2009; Zachos et al., 2001; Joachimski et al., 2006 ; Chen et al., 2016). Oxygen isotopes have been used primarily as a proxy for paleotemperatures (Urey, 1947; Epstein et al., 1953; Emiliani, 1955). Oxygen ($\boldsymbol{\delta}^{18}O$) values are a function of salinity, temperature as well as ice sheet growth and demise. Higher $\boldsymbol{\delta}^{18}O$ values may reflect higher salinity, lower temperature, ice sheet growth (where lighter $\boldsymbol{\delta}^{16}O$ is locked in ice sheet), or a combination of the three. Since organisms, e.g.

brachiopods, foraminifera, etc., grow in equilibrium with seawater, measured values of $\boldsymbol{\delta}^{18}O$ from pristine, unaltered samples (assuming minimal/insignificant kinetic fractionation related to evaporation and/or influx of fresh, lighter water) provide a proxy to assess paleoclimate.

Our understanding of the last 800 ka is that glacial-interglacial periods were driven by orbital forcing (Mudelsee and Stattegger, 1997). Milankovitch cycles refers to long term variations in the earth's orbit around the sun (eccentricity), axial tilt (obliquity), and wobble (precession). These cycles will dictate the amount of solar insolation received by the earth. Higher isolation may cause ice sheets to melt, which in effect reduces reflectivity (albedo effect) resulting in more energy absorbed by earth. Warmer climate will be associated with warmer and better-mixed ocean (Sigman and Boyle, 2000) where $CO_2$ and $H_2O_{vapor}$, which are greenhouse gases, are released to atmosphere driving the climate to be warmer. This positive feedback loop could have led to glacial terminations (Broecker et al., 1985; Crowley, 1992). Glacial terminations were associated with a rise of about 5 °C (Shackleton, 1967; Emilian and Ericson, 1991) and were preceded by global warming that precedes the initial rise in $CO_2$ (Shakun et al., 2012) which may suggest that $\boldsymbol{p}CO_2$ did not trigger deglaciation, but rather acted as a catalyst that amplified the climatic signal.

When we look at our eustatic curve constructed based on sedimentology and compare it with $\boldsymbol{\delta}^{18}O$ from Naqing section (Chen et al., 2016) and $\boldsymbol{p}CO_2$ (Montañez et al., 2016) we observe interesting trends. The top of the Missourian Canyon and the Virgilian Cisco are coincident with significant $\boldsymbol{\delta}^{18}O$ excursions of 1.2 and 2.1‰ respectively (Fig. 3.9d) which were associated with platform-wide exposure. In addition, several composite

sequences recognized in core appear to coincident smaller scale $\boldsymbol{\delta}^{18}O$ excursions. Although, we understand that not every event will be recorded due to sampling bias (missed beats) and/or preservation potential (diagenetic alteration, erosion, etc.), platform-wide exposures appear to be inherent to a global signal. In addition, the late Pennsylvanian $\boldsymbol{p}CO_2$ record (Montañez et al., 2016) persisted under mostly under 420 ppm, reached 560 ppm and remained under 840 ppm (Fig. 3.9c). According to climate simulation models, any value of $\boldsymbol{p}CO_2$ under 420 ppm suggests stable glaciation conditions, whereas $\boldsymbol{p}CO_2$ values that reach up to 560 ppm suggest glacial-interglacial conditions (Horton et al., 2012). There are no $\boldsymbol{p}CO_2$ records above 840 ppm in the late Pennsylvanian (Montañez et al., 2016) which supports the absence of any ice-free conditions during that period.

The top Missourian Formation shows $\boldsymbol{\delta}^{18}O$ value that is comparable to the late Eocene $\boldsymbol{\delta}^{18}O$ values (~1.25‰) where 25% (~0.2‰) is ascribed to cooling, based on Mg/Ca paleotemperatures, whereas the rest of the signal (~1‰) is attributed to Antarctic ice sheet growth (Lear et al., 2000). In addition, the top of the Virgilian $\boldsymbol{\delta}^{18}O$ excursion is comparable to the Last Glacial Maximum (LGM) ~1.8 ‰ (Shackleton and Matthews, 1977; Schrag et al., 2002; Lea et al., 2002) which was responsible for lowering sea level ~120 m of present day (Peltier and Fairbanks, 2006). The atmospheric $\boldsymbol{p}CO_2$ curve shows "in-sync" as well as "out-of-sync" correspondences to observed cyclicity in the SACROC. Most of the "in-sync" response occurred during platform-wide exposure events, and the absolute $\boldsymbol{p}CO_2$ during the late Pennsylvanian (Virgilian) fell below 190 ppm which is the lowest concentration of atmospheric $CO_2$ reported during the LGM (Bouttes et al., 2011). Overall, the atmospheric $\boldsymbol{p}CO_2$ remained below a threshold (<560 ppm) where continental

ice sheets are stable and may grow (Horton et al., 2010). The higher $\boldsymbol{\delta}^{18}O$ excursion and lower $\boldsymbol{p}CO_2$ during the Virgilian imply a larger ice volume compared to the Missourian. Although, based on sedimentologic evidence we report a minimum eustatic amplitude variation of 37 m (Missourian) and 40-45m (Virgilian), our best estimates were likely subdued as a result of being confined in an intracratonic basin several hundreds of kilometers from the open ocean. Large eustatic changes may not reflect the absolute amplitude of sea level change due to variations in paleotopographic configuration and/or active uplift and subsidence. During significant glaciation and associated global sea level draw down, eustatic amplitude recorded in intracratonic areas will be the same as the one observed globally as long as intracratonic seas are connected to open oceans. However, if uneven topography existed in the intracratonic basin, the eustatic amplitude will be a fair proxy, but factors such as uplift and subsidence are needed to decipher the absolute global amplitude.

A global synthesis of Pennsylvanian/Permian boundary documents that this boundary represented by a major exposure surfaces, erosional unconformity, disconformity or hiatus (Koch and Frank, 2011; Melvin et al., 2010). This global marker is consistent with a significant widespread glaciation through the latest Pennsylvanian (Veevers and Powell, 1987; Isbell et al., 2003). In the U.S. Midcontinent and the Russian platform, the Pennsylvanian/Permian boundary shows regression as suggested by apparent basinward shift in facies (West et al., 1997; Olszewski and Patzkowsky, 2001, 2003). The basinward shift in facies may be explained partly as a result of apparent eustatic fall caused by tectonic uplift and cratonic warping, however, subsidence rates alone were not high enough

(Watney, 1984) to produce the observed high-frequency ($4^{th}$ order) cycles with period of 400 ky (Heckel, 1986). Thus, these high-frequency cycles are more consistent with Milankovitch eccentricity signal (Read, 1995). This further supports the paradigm that the late Pennsylvanian was a time of significant glaciation, rather than the dominance of greenhouse conditions (cf. Fielding et al., 2008; Bishop et al., 2010; Martin et al., 2012).

**High-frequency cycle periodicity**

The average period of high-frequency cycles can be calculated by dividing the duration of the section by the number of the cycles contained within the section. The estimated period is based on the assumption that thickness equals time, which was probably not the case. The number of mapped cycles is likely incomplete due to variety of reasons including deposition away from control points (during sea level rise or fall), erosion and non-preservation, non-deposition and inability to decrypt cycles at condensed intervals. We identified 23 high frequency cycles for the Missourian Canyon (period ~100 ka) and 14 high frequency cycles for the Virgilian Cisco (period ~343 ka) formations. As these values are considered to be minima, the calculation will reveal an average period estimated for the high frequency cycle. Harland et al. (1982) estimated the average period of Late Pennsylvanian cycles to range between 216 ka to 422 ka (in Goldhammer et al., 1991). Similarly, Heckel (1986) had a range between 235 ka to 393 ka as an average cycle period which he suggested corresponds to long term eccentricity. In addition, Bishop et al. (2010) had similar estimates from the Bird Spring Formation with an average period of ~100 ka

for the Missourian and ~400 ka for the Virgilian stage. However, Martin et al. (2012) had slightly different periods for the Bird Spring with a longer average period for the Missourian (358±180 ka) and a comparable period (398±133 ka) for the Virgilian to the other studies. Goldstein (1988) estimated a period of 300 ka for the Virgilian Holder Formation. Algeo and Wilkinson (1988) estimated a period of 400 ka for depositional high frequency cycles from the late Mississippian to the late Pennsylvanian.

Hays et al. (1976) used spectral analysis of Quaternary ice ages from two deep-sea sediment core from southern Indian Ocean suggesting that solar insolation changes are probably driven by Milankovitch orbital cycles. The overall consensus in cycle periodicity estimated for high frequency cycles for the Canyon and the Cisco in the Midland Basin leads to the inference that short- and long-term eccentricity were instrumental in controlling ice volume and, hence, eustatic oscillation. However, correlation does not necessarily prove causation as there are obvious discrepancies in periods estimation. These discrepancies may be attributed to missing time in the rock record (non-deposition/no preservation), limitation of control points (introducing missed beats), absolute age of units, different orbital forcing (Milankovitch) components (in-sync or out-of-sync), tectonic influence, changes in $pCO_2$ or a combination of all.

## CONCLUSIONS

1. The Missourian Canyon Formation consists of 23 grainstone-capped high frequency cycles dominated by aggradational to progradational stacking patterns with a minimum amplitude of 37 m and an average period of 100 ka.

2. The Virgilian Cisco Formation is composed of 14 high frequency cycles that show retrogradational stacking pattern and suggesting an increased amplitude compared to the Missourian. This hypothesis is supported by exposed shallow water facies juxtaposed next to and at the base of deep water facies proposing a eustatic rise of at least 40 m followed by 45 m of sea level fall during an average period of 343 ka.
3. Our composite eustatic curve suggests that the Late Pennsylvanian was a time of extensive glaciation characterized by high-frequency, high-amplitude sea level fluctuations. The minimum amplitude of sea level change estimated from vertically stacked facies in high frequency cycle is >37 meters.
4. Our findings support earlier work emphasizing the dominance of icehouse conditions during the late Pennsylvanian with an increasing eustatic amplitude from the Missourian to the Virgilian.

# CHAPTER 4: GEOMODELING OF A COMPLEX ICEHOUSE ISOLATED PLATFORM, SACROC FIELD, WEST TEXAS


## ABSTRACT

The SACROC Field is an isolated carbonate platform that was deposited during peak icehouse conditions (Missourian-Virgilian) characterized by high-frequency, high-amplitude eustatic fluctuations resulting in complex facies architecture. Facies modeling of such complex systems using geostatistical methods based on probability functions alone are insufficient to capture the system's heterogeneity and its complex geological features. We compare the results of three geostatistical methods used for lithofacies modeling: Multiple-Point Statistics (MPS), Sequential Indicator Simulation (SIS), and Truncated Gaussian Simulation (TGS) to represent complex reservoir architecture in the subsurface. MPS method uses conceptual model-based training images incorporating spatial data from outcrop and/or, modern analogs to aid the modeling algorithms to reproduce and capture complex reservoir architecture in the subsurface. MPS geostatistical method distributed lithofacies distribution was most the closely comparable to conceptual models and outcrop-based observations. Other modeling methods when conditioned by training images and facies probability cubes produced improved and comparable results to the MPS models, yet inconsistencies are still present. The MPS lithofacies model produced what we consider geologically the most reasonable model, retaining lateral and vertical facies changes across and off the carbonate platform, due to variations of the environment of deposition and gradual lateral shift of the facies belts with time. Thus, this model was used to condition

porosity and permeability distributions within the petrophysical property model. Multiple-point statistics method preserved the distribution of geomorphologically-controlled facies, including basin and slope, and shallow-water platform top facies distribution with grainier windward (eastern) side.

## INTRODUCTION

3D reservoir geological models have been used to guide the development of oil and gas fields (Zhang et al., 2006; Arslan et al., 2008; Chenghua et al., 2016; Haque et al., 2018). These models are built by the integration of subsurface data including 2D/3D seismic data, borehole data, and information derived from core descriptions. However, subsurface data alone, without the benefit of geologic concepts/understanding are generally insufficient to establish sound three-dimensional models of the subsurface. Thus, outcrop and modern analogs represent an invaluable resource to incorporate spatial data into the modeling efforts.

The SACROC Field (Fig. 4.1) is an isolated carbonate platform that was deposited during peak icehouse conditions characterized by high-amplitude, high-frequency glacioeustatic fluctuations during the Late Pennsylvanian (Fig. 4.2) (Schatzinger, 1988; Kerans, 2001; Alnazghah and Kerans, 2018). Icehouse glacioeustasy, with its high-frequency high-amplitude sea-level fluctuations, drives the development of complex depositional facies architectures whereby depositional topography created during a high-frequency sea level rise is typically not totally infilled and annealed prior to the sea-level fall, and thus the subsequent rise inherits a starting surface with significant local topography and thus facies variability. This nonequilibrium condition (i.e. accommodation space created during one cycle is not flattened or "equilibrated" prior to the ensuing transgression) drives a complex facies architecture with juxtaposed deep- and shallow-water facies punctuated by multiple exposure surfaces, diastems, and unconformities comparable to the modern Bahamian isolated platforms (Eberli and Ginsburg, 1989; Wanless and Dravis, 1989; Aurell et al., 1995) and to the Late Pennsylvanian Beeman and Holder formations in the Sacramento Mountains (Goldstein, 1988; Raatz and Simo, 1998; Rankey et al., 1999; Janson and Madriz, 2012). These outcrop analogs provide insight on how depositional facies are arranged, both vertically and laterally.

One of the characteristic depositional heterogeneities of icehouse carbonate reservoirs is the presence of carbonate mounds or reef structures. These mounds are commonly generated either on the flanks of platforms or across the platform tops associated with the high-amplitude-high-frequency sea-level rises that generate significant accommodation across the platforms. Carbonate mounds are a common component of

many Carboniferous icehouse hydrocarbon reservoirs, including the giant Aneth Field of the Paradox Basin (Peterson, 1992), Korolev Field (Putney et al., 2008), and the Tengiz Field (Weber et al., 2003; Collins et al., 2006) and Kashagan Field (Ronchi et al., 2010) of the Precaspian Basin. Because these mounds can represent high reservoir quality intervals and have complex three-dimensional distributions, building a model that captures the internal complexity of carbonate mound systems in subsurface reservoir targets is of primary importance. A close approximation of mound distribution will positively affect reservoir models ability to predict porosity and permeability distribution and thus reservoir behavior. Currently only few studies on geomodeling carbonate mounds in general have been published (Adams et al., 2005; Galli et al., 2006) and icehouse carbonate mounds in particular (Janson and Madriz, 2012). The combination of extensive core control, dense well-log control, and a 3D seismic volume with 40 Hz dominant frequency make the northern platform portion of the SACROC field an excellent case study of this style of reservoir heterogeneity and a good case example of the application of different subsurface facies modeling approaches.

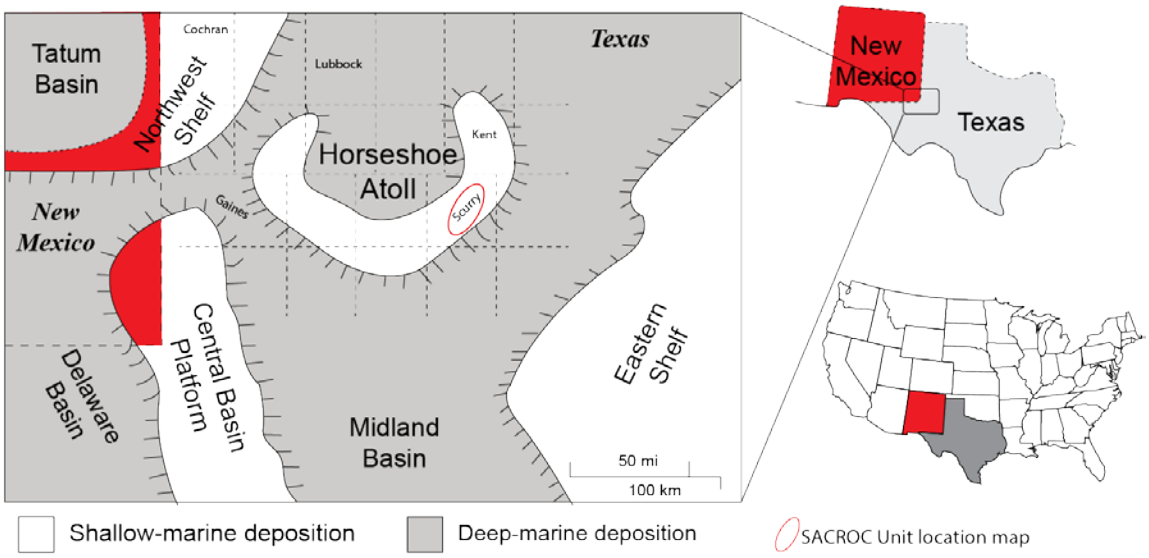


**Fig. 4.1**: Location map of the study area (SACROC) showing basins and structural elements (modified from Saller et al., 1994).

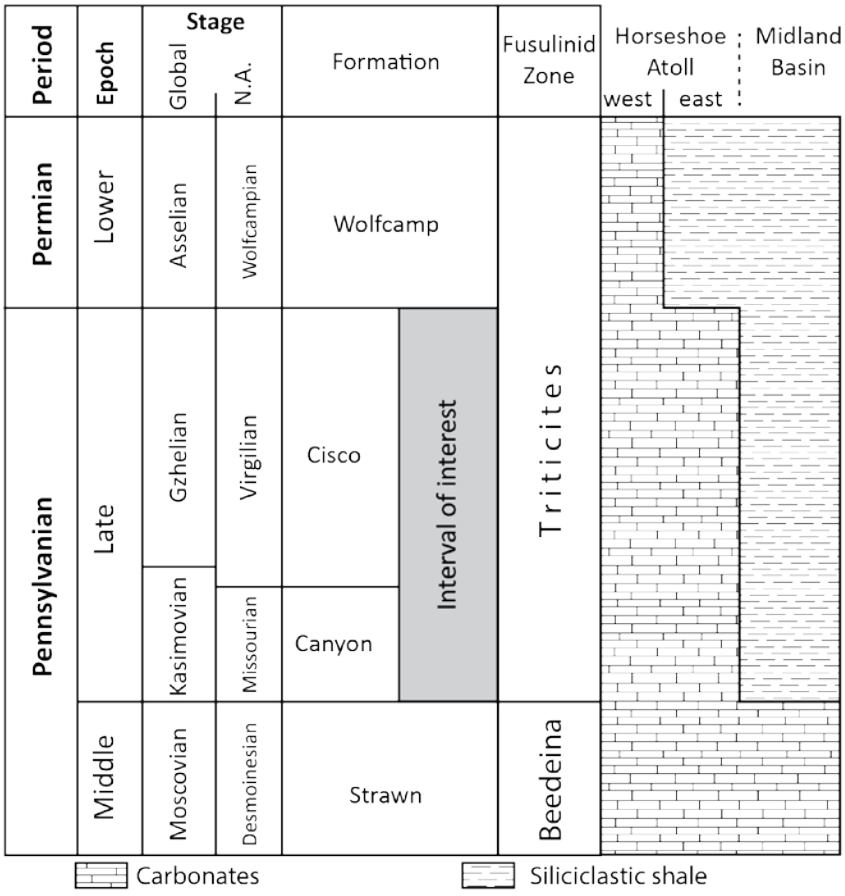


**Fig. 4.2**: Generalized West Texas stratigraphic column showing the interval of interest.

This study establishes a 3D model incorporating well-constrained facies architecture in addition to petrophysical properties of the Late Pennsylvanian strata in the SACROC Field. We illustrate the importance of incorporating "soft data" in terms of conceptual models and geological understanding in building complex geological models to effectively capture depositional facies heterogeneity and petrophysical properties. In this paper, several pixel-based modeling algorithms were tested. Standard workflow starts with the construction of high-resolution sequence stratigraphic framework utilizing core, wireline logs, and 3D seismic to map stratigraphic cycles and sequences at the scale of 2 –

20 m (Chapter 2). Combining sedimentological (1D) and stratigraphic (1D & 2D) contexts with outcrop and modern carbonate analogs are used to develop conceptual models that were later converted into training images (TI) used to guide the modeling software to distribute lithofacies in 3D geological models. Training images and cored wells represent deterministic components of the 3D lithofacies model, whereas uncertain lithofacies generated away from control data are parts of residual stochastic components. Lithofacies modeling using Multiple-Point Statistics (MPS) offers an alternative to conventional variogram-based methods using two-point statistics for lithofacies modeling. MPS can be used to model complex reservoir architecture through the use of TI that captures lithofacies geometrical characters. It can also impose stationarity conditions related to platform's geomorphology while honoring hard data from cored wells. As a follow-on, alternative pixel-based modeling algorithms including truncated Gaussian simulation (TGS) and sequential indicator simulation (SIS) that depend primarily on two-point statistics were tested first and then later conditioned by TIs. The results of the different modeling methods are compared and discussed to determine the most suitable approach to model the complexity of icehouse carbonates systems and to capture the heterogeneity of their depositional facies and petrophysical properties.

## STRATIGRAPHIC ARCHITECTURE

### SACROC lithofacies

The Late Pennsylvanian Canyon and Cisco formations as described from the north platform of the SACROC unit and are characterized by ten lithofacies (Table 4.1) based on mineralogy, texture, sedimentary structures, and main grain types (Alnazghah and Kerans,

2018). The Canyon and Cisco successions represent an isolated carbonate platform similar to modern isolated platforms in the Bahamian Archipelago. These lithofacies are clustered into five facies associations related to broader depositional environments. Facies associations reflect the lateral facies juxtaposition controlled by several factors including hydraulic energy, light penetration, nutrient supply, oxygen levels, salinity, water temperature, and suspended sediment (James and Jones, 2016). The generally recognized facies patterns are that high-energy ooid and peloid grainstones, fusulinid-crinoid grainstones, and phylloid boundstones form on stabilized paleotopographic highs facing the prevailing wind (Fig. 4.3) (Chapter 2). The central portions of the shoals are dominated by ooids and peloids, followed basinward by fusulinid-crinoid grainstones and packstones, and are replaced finally by slope and basin deposits, being shales and carbonate mudstones. Shoal centers form a stabilized substrate where phylloid mounds nucleate, both directly above and flanking the shoal bodies. Phylloid boundstone core facies pass laterally into flank facies that make up most of the platform top deposits during deposition of the Cisco unit (*cf*. Janson and Madriz, 2012; Chapter 2). The abundance of skeletal and non-skeletal grainstones and packstones decreases towards the basin, replaced by carbonate mud. Mud-dominated slope facies include gravity-driven crinoid rudstone turbidites, concentrated density flows, and slope-failure debris flows. The basinal facies association consists of siliciclastic shale interbedded with carbonate mudstones.

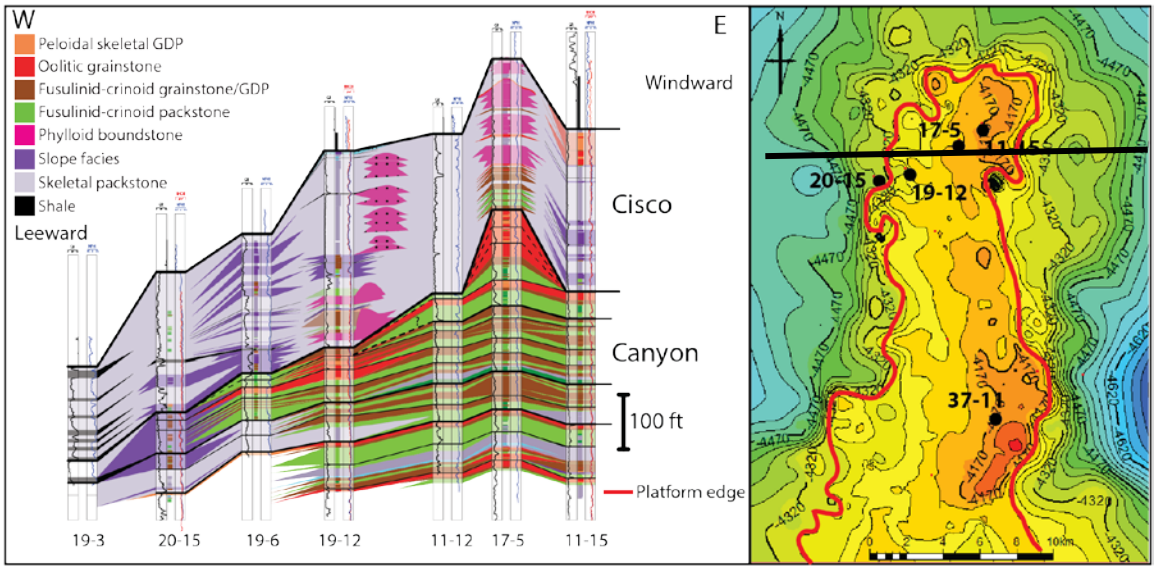


**Fig. 4.3**: Stratigraphic cross section showing the dominance of high-energy depositional facies on the windward side and the abundant offplatform deposits on the leeward side. Black line on the top of Canyon structure map on the right shows the cross section location

| | Facies | Sedimentary Structures | Thickness | Grain size | Sorting | Grain types | | Depositional Environment | Water depth |
|---|---|---|---|---|---|---|---|---|---|
| | | | | | | *Non-skeletal* | *Skeletal* | | |
| Deeping | Shale | Finely laminated, fissile, sharp basal and top contacts, cyptic biotrubation | Few centimeters up to 1.5 m | Mud/silt | | | | Basin | +35 m |
| | Crinoidal Rudstone | | 30 cm - 4 m | fine to granular | Poorly | Peloids | mainly crinoids, minor: brachipodos, bryozoan, fuulinid, agglutinated forams, phylloid plates | Outer shelf/slope apron | +30 m |
| | Phylloid boundstone | Bioturbation | 2 m - 25 m | fine to granular | Poorly to moderately | Peloids | mainly phylloid algal plates, crinoids minor: fusulinids, fenestrate bryozoans, brachiopods, agglutinated foraminifera sponge spicules.rugosan corals, stromatoporoids | Outer shelf/margin | 20-150 |
| | Crinoidal Wackestone | | 1.5 m - 10 m | medium to granular | Poorly | Peloids | mainly crinoid ossicles rare: bivalve, foraminifera, sponge spicules | Middle shelf | 15-25 |
| | Crinoid Phylloid Wackestone | Bioturbation, stylolitization | 30 cm - 6 m | fineto granular | Poorly to moderately | Peloids | mainly phylloid algal plates and crinoids rare: fusulinids, agglutinated foraminifera, sponge spicules | Middle shelf | 5-25 |
| | Skeletal Peloidal Packstone | Bioturbation | 30 cm - 8 m | fine to coarse | Moderate to poorly | Peloids | mainly phylloid algal plates, crinoids, fusulinids. minor: agglutinated foraminifera, sponge spicules | Middle shelf | 5-25 |
| | Crinoid-Fusulinid Packstone | Bioturbation | 30 cm - 6 m | fine to granular | Moderate to poorly | Peloids grapestones | mainly crinoids, fusulinids minor: brachiopods, agglutinated foraminifera | Inner shelf | 5-20 |
| | Crinoid-Fusulinid Grainstone | Cross and parallel stratification, biotrubation oblitrating stratification | 30 cm - 8 m | coarse to very coarse | Moderately sorted | Peloids | mainly crinoid stem segments, fusulinids minor: agglutinated formainifera, algal plates | Inner shelf | 5-15 |
| | Skeletal Peloids Grainstone | Low-angle planar lamination, bioturbation, calichification | 30 cm - 6 m | fine to medium | Well to moderate | Peloids | minor: crinoids, fusulinids, agglutinated foraminifera | Shoal | 0 - 5 |
| | Oolitic Grainstone | Cross stratification, calichification | 30 cm - 12 m | fine to medium | well-sorted | Ooids coated grains | minor: crinoids, bivalves and gastropods | Shoal | 0 - 5 |

**Table 4.1**: Lithofacies of the Late Pennsylvanian in SACROC field.

**Cyclicity and Sequence Stratigraphy**

The Late Pennsylvanian sequence stratigraphic framework of the SACROC field was constructed using eleven cored wells as a guide while integrating 650 wireline logs within the field, for an average data spacing of 500 m (Fig. 4.4). Meter-scale cycles are recognized through documentation of lithofacies successions. In the Canyon Formation, each meter-scale cycle consists of a transgressive and regressive hemicycle (Fig. 4.5) separated by turnaround points representing maximum flood surface (transgression) and cycle top (regression). The transgressive part of cycles is characterized by mud-dominated packstone and wackestone lithofacies, whereas the regressive part consists of grain-dominated packstones and grainstones. The packstones and grainstones that are found at the top of cycles contain interparticle pore space ranging from 10 to 20%, in contrast to the mud-dominated lithofacies at the base of cycles, where porosity values of 3-6% are more common. The positive correlation between lithofacies and neutron log was utilized to correlate wells and populate well tops from cored to uncored wells across the field.

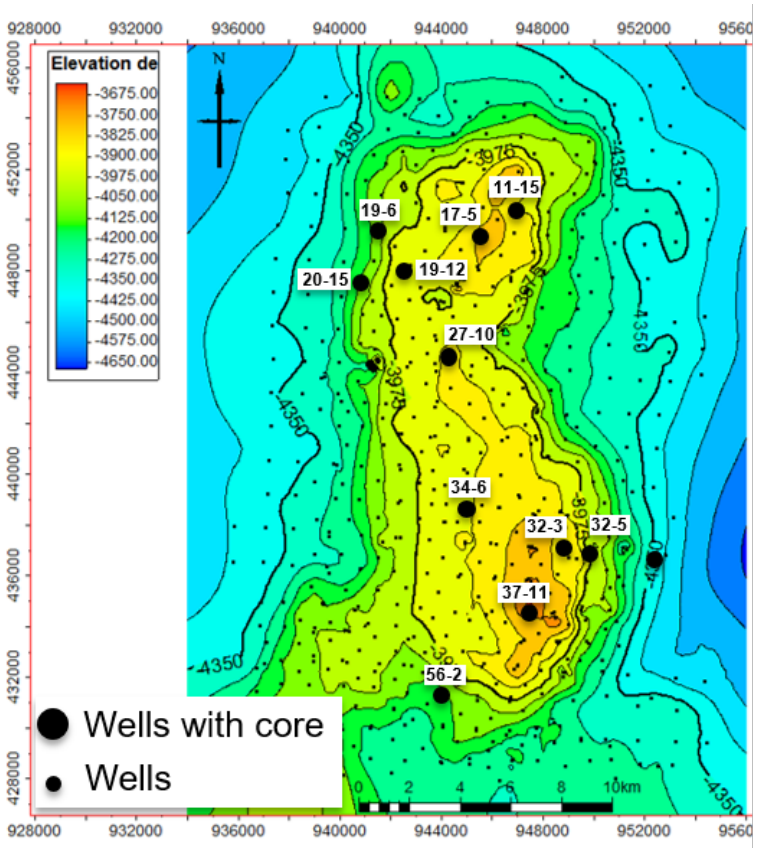


**Fig. 4.4:** Map of the top Cisco structure with the location of cored wells and wells with wireline logs.

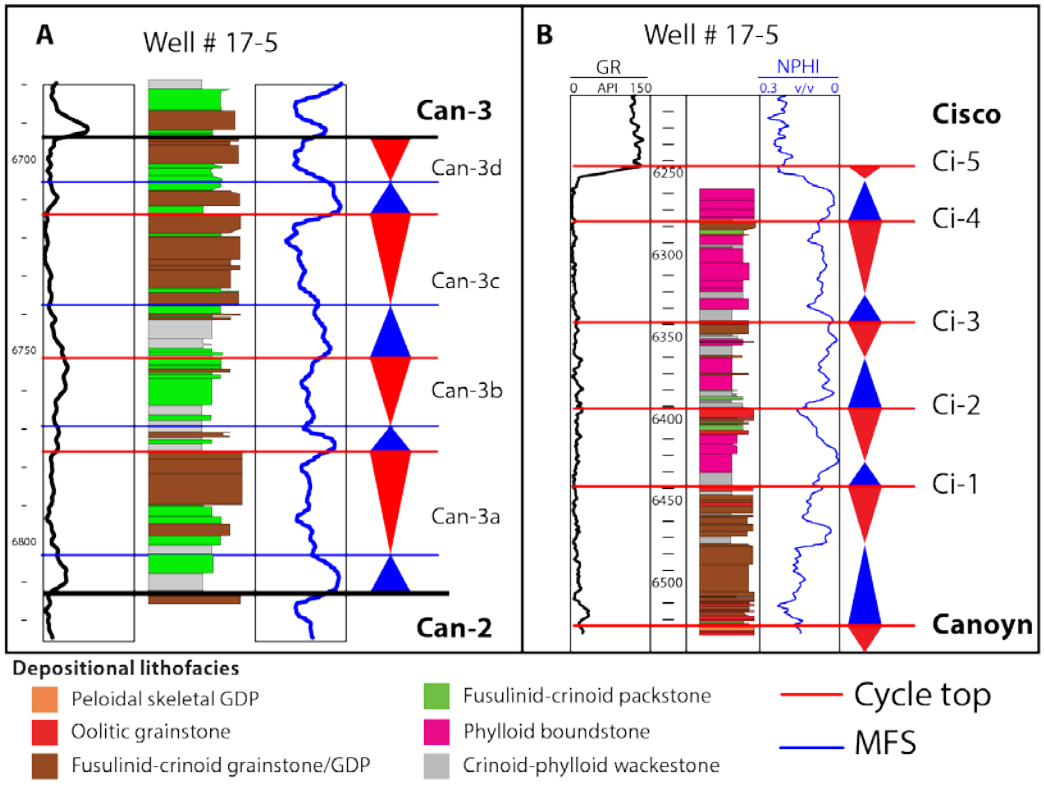


**Fig. 4.5**: An example illustrating the good correlation between maximum flooding surface and cycle top from core to low and high neutron porosity readings in the Canyon Formation. This correlation was exploited to populate stratigraphic picks across the field. In the Cisco Formation, trends were inconsistent and correlation across the field was much more challenging compared to the more ordered Canyon Formation. GDP = grain-dominated packstone.

The Virgilian Cisco Formation was deposited during a time of increased glacioeustatic fluctuations (+40 m) (Veevers and Powell, 1987; Isbell et al., 2003; Rygel et al., 2008; Alnazghah and Kerans, 2018), a favorable condition for biohermal growth of phylloid algae (Toomey, 1980; Soreghan and Giles, 1999). The stronger glacioeustatic

fluctuations, related to waxing and waning of ice sheets, drove a less ordered succession with abrupt vertical and lateral changes in depositional lithofacies, growth of phylloid bioherms with limited lateral continuity (Janson and Kerans, 2007; Janson and Madriz, 2012), and abundant subaerial and meteoric diagenesis features. In the Cisco Formation, five upward-shallowing cycles separated by significant facies offset and/or exposure-related features are recognized (Chapter 2). Extending the Cisco's cycles was much more challenging, and only four cycles were correlated across the field with moderate confidence especially in complicated zones.

## GEOLOGICAL MODELING

The modeling workflow employed here to build 3D geologic models of the SACROC isolated icehouse carbonate platform includes first structural modeling, followed by facies modeling, and finally petrophysical modeling.

### Structural modeling

Structural modeling is the process of mapping the stratigraphy and faults of the reservoir in 3D. The gridded structural surfaces were tied to mapped stratigraphic markers and were checked for any overlap. In complex geologic settings, the structural model is the center-piece of the project as it represents the container that can be filled with various discrete and continuous variables. Structural modeling involves the following steps:

a) Data input: 3D seismic and wireline logs including neutron porosity, gamma ray, bulk density, calculated permeability, and digitized lithofacies logs

b) Correlation: Stratigraphic picks (maximum flooding surface and cycle tops) were generated as well tops in every cored well and then were populated across the field using wireline logs correlation.

c) Surface generation: Surfaces were generated using a combination of well tops and reference surfaces (Canyon- and Cisco-top) generated from seismic as a trend to control surface shape away from control points.

d) Zonation and layering: cell grid dimension is dictated by the optimum horizontal cell size and the minimum thickness of features that can be resolved vertically and hence was set to 250 x 250 x 0.15 m generating a 3D grid that have more than 9 million cells. Zonation is the process of creating different zones of the reservoir using the mappable stratigraphic units which generated 31 zones. The lower 27 zones are within the Canyon Formation and represent transgressive or regressive hemicycle. On the other hand, the upper 4 zones are in the Cisco Formation and represent mostly regressive cycles.

Each zone is then divided into a number of layers that are linked to the zone's thickness and internal variability. Fine-scale layering is required to ensure a sufficient number of layers to capture important details and heterogeneities that are critical for petrophysical modeling. Several styles of layering schemes were tested including: a) follow top layering where layers curvature will parallel a top reference grid and are truncated towards the base grid, b) follow base layering where layers curvature will parallel a base reference grid and are truncated towards the top grid,

and c) proportional layering where the sum of layers is constant in the entire zone independent of its thickness.

**Facies Modeling**

Two modeling techniques that utilize geostatistics to distribute lithofacies spatially and temporally by means of interpolating data away from control points were considered: two-point and multiple-point statistics. In both modeling techniques, lithofacies predictions are conditioned to the intrinsic structure, sampling quantity, and geometric pattern. A total of five geological models were built, with several realizations, to assess the feasibility of building complex geometries and facies architecture with currently available modeling tools.

In the multiple-point statistics approach of lithofacies modeling, a conceptual model that provides an idealized map-pattern facies distribution with accurate lateral scales and lateral transitions as well as aerial geometries is required as input to run multipoint statistics (MPS). For the software to use the conceptual model, it first needs to be converted into a training image (TI) (Fig. 4.6), which then can be used as an input along with other input data to generate facies model. The quality of the MPS-generated 3D lithofacies model will be dependent on how reliable the initial conceptual model is. Our conceptual model is based on two sets of data including outcrop and modern analogs. We utilized age-equivalent Holder Formation (Virgilian, New Mexico) as an outcrop analog (Janson and Madriz, 2012) for mound dimensions and facies proportions (mound versus flank). In addition, we used modern Bahamian platforms (Grammer et al., 1993; Crevello and Schlager, 1980) as well as outcrop analogs including the upper Devonian Great Barrier

Reef in the Canning Basin (Playford, 1980), the Middle Triassic Latemár of northern Italy (Egenhoff et al., 1999), and the Upper Cretaceous Apulian platform (Sanders, 1996) to distribute lithofacies associations controlled by platform's geomorphology and prevailing wind direction (Mullins and Cook, 1986; Walker et al., 1995; Golonka, 2011; Chapter 2).

Three conceptual models, converted into training images, (Fig. 4.6) were used to guide MPS lithofacies models for the Late Pennsylvanian Canyon and Cisco formations. Two training images correspond to transgressive and regressive hemicycles in the Canyon Formation, while the other training image corresponds to the entire Cisco succession.

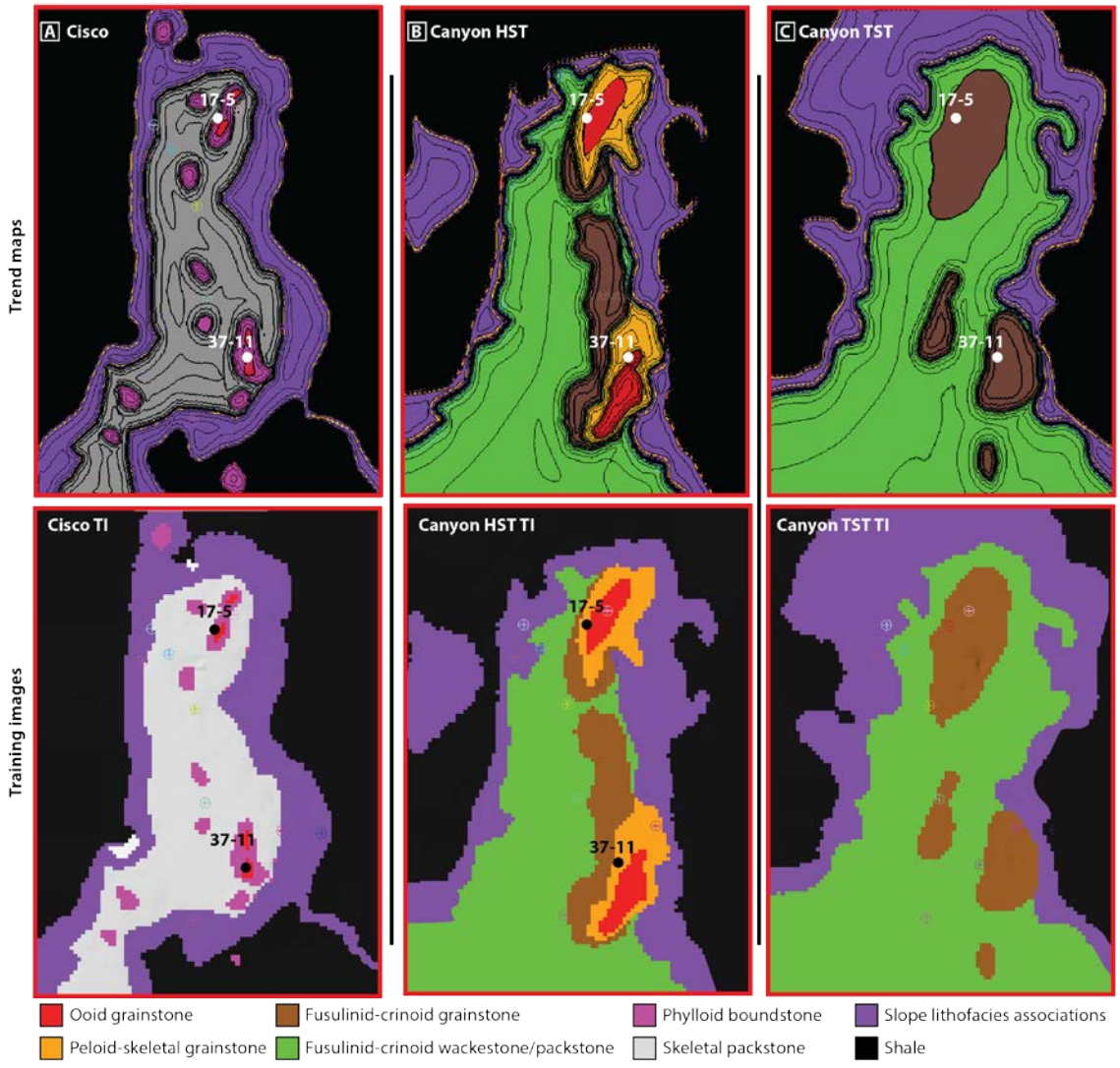


**Fig. 4.6**: Three facies trend maps based on conceptual model used to create training images: A) Cisco trend map, B) Canyon regressive trend, and C) Canyon transgressive trend.

Conventional two-point statistics modeling techniques rely on repeated sampling from input facies proportions and spatial parameters (variograms) to generate mapped distributions of a given property, in this case facies (Pyrcz and Deutsch 2014). Truncated

Gaussian Simulation (TGS) and Sequential Indicator Simulation (SIS) were used to generate lithofacies models. TGS is based on ordered facies proportions and relationships and their spatial distribution which then can be used to generate different realizations. The generated lithofacies model is based on geostatistics from lithofacies logs in cored wells and conceptual lateral facies relationships. Experimental variograms used in TGS assume the same spatial continuity (ordering) of all lithofacies and imply the same anisotropy and correlation distance. On the other hand, SIS has a major problem as it handles and models each facies separately where their spatial position is not considered as a constraint. SIS requires creating variograms for each facies for each zone which can be a time-consuming and is a distinctly arbitrary process.

SIS and TGS models were later conditioned by the same TIs and lithofacies probability function used in MPS model. A facies probability function expresses the relationship between the facies log and TIs and becomes important as a source of conditioning away from hard data points. Generated models where then compared with the original stratigraphic section by taking a slice from the facies model at the same location of the stratigraphic section.

**Petrophysical Modeling**

Porosity and calculated permeability logs were upscaled and conditioned to facies to fill grid cells with petrophysical properties. Permeability was calculated for all wells using the global transform equation (Lucia, 1995):

$$K = 10^{\wedge} \{[9.7982 - 12.0838 * \mathrm{Log}_{10}(rf)] + [8.6711 - 8.2965 * \mathrm{Log}_{10}(rf)] * \mathrm{Log}_{10}(\phi)\}$$

where “rf” is the rock fabric number and “ϕ” is interparticle porosity. A major assumption in permeability calculation is that total neutron porosity from borehole measurements equals interparticle porosity. This assumption is inaccurate but is the only viable method to calculate permeability given the lack of acoustic logs, which makes it difficult to calculate separate vug porosity. Porosity measurements from plugs show a differentiation in porosity ranges based on primary fabric (Fig. 4.7). In general, grainier facies tend to have higher porosity, whereas muddier facies to have lower porosity (Fig. 4.7). Thus, porosity model was conditioned to predicated depositional fabric predicted.

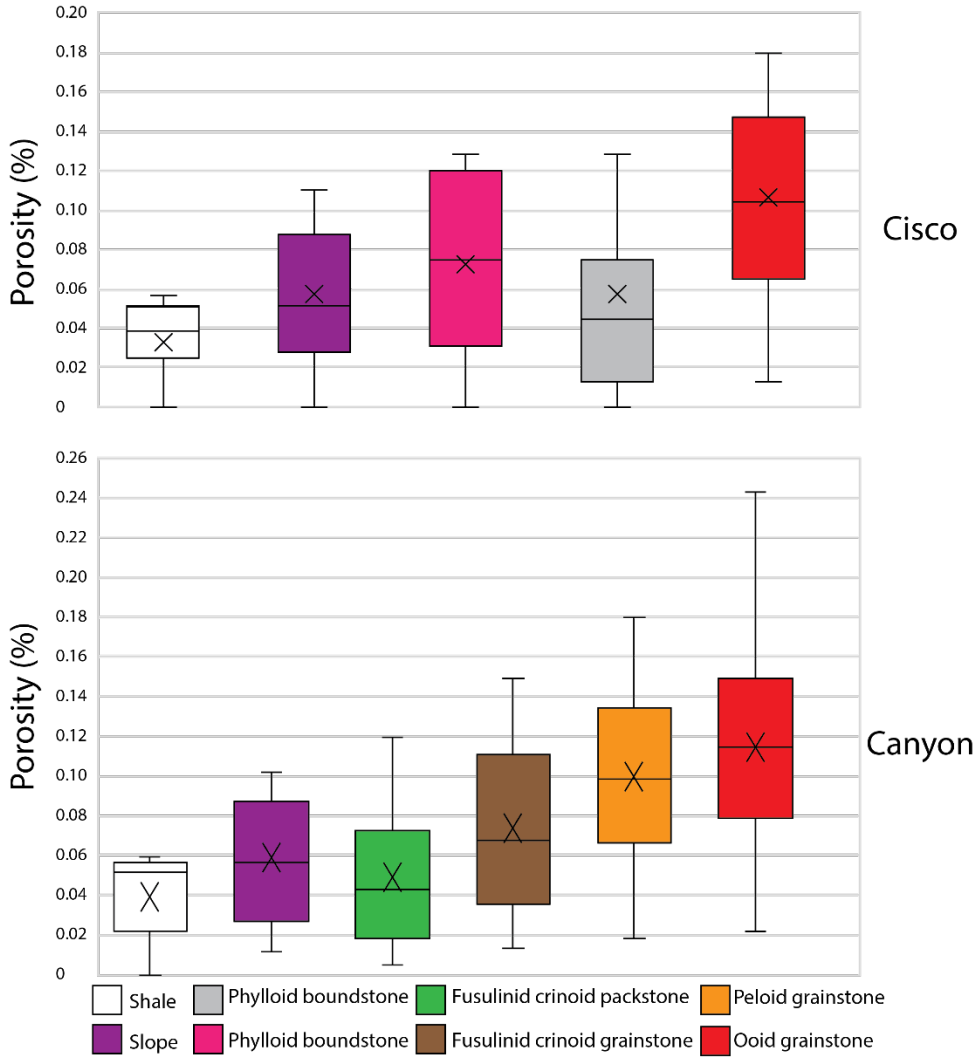


**Fig. 4.7**: Porosity measurements from plugs categorized by primary fabric for both the Canyon and the Cisco formations.

When modeling petrophysical properties, algorithms handle porosity and permeability as continuous variables, unlike lithofacies modeling where lithofacies are handled as discrete variables. For porosity modeling, we employed Sequential Gaussian Simulation (SGS) procedure which is widely used for data-conditioned stochastic models of spatial phenomena utilizing Gaussian Random Functions (e.g., Hadi et al., 2005;

Schepers et al., 2009). The SGS is a univariate, kriging-based analysis used in petrophysical modeling for stochastic characterization of continuous variables which simulates nodes sequentially and uses simulated values as conditioning data in the following nodes (Ringrose and Bentley, 2014; Pyrcz and Deutsch 2014). The success of kriging algorithm to reproduce reliable results depends on the number of control points used for interpolation and their spatial proximity to control data. A bivariate analysis using SGS algorithm collocated with cokriging is used to model permeability within the 3D MPS lithofacies model. In this procedure, the modeled porosity using the SGS is used as a secondary data for modeling permeability.

## RESULTS

### MPS Model

The MPS model produced most of the facies trends expected (Fig. 4.8) when compared to the stratigraphic and depositional model derived from core descriptions, log correlation, and links to seismic data (Fig. 4.3) and the proposed conceptual models. For example, ooid and peloid-skeletal grainstones are only found at the platform top and along its windward side. In addition, basinal shale is only present in off platform areas. That said, in the first iterations of the 3D model, the lithofacies transitioning boundaries were sharp due to the limited TIs used, the limited control points at the location of facies boundaries, and probability cubes of geomorphologically-controlled lithofacies. Preliminary lithofacies probability cubes were generated based on the presence or absence for specific lithofacies which resulted in the generation of a discrete lithofacies proportional model where probability of a certain lithofacies jumps from 0% to 100%. Later iterations adjusted the lithofacies proportional models into continuous, instead

discrete resulting in improved lithofacies boundaries. Further, the results can be improved substantially if a training image is produced for each zone as well as if more core data is acquired and incorporated. Nonetheless, in this exercise we only used the three most representative conceptual models for the Canyon and Cisco successions, which resulted in stacked facies trends, thus yielding localized blocky and unnaturally sharp boundaries.

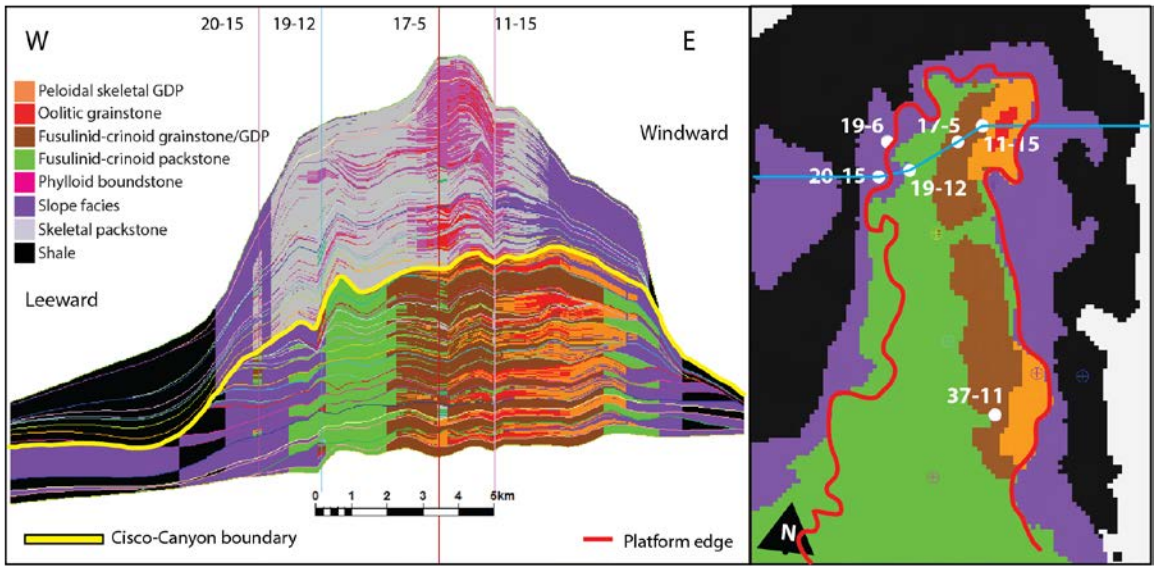


**Fig. 4.8**: An east-west slice of 3D facies models and map view at the top of the Canyon generated by Multipoint Statistics (MPS) consistent with conceptual model.

SIS and TGS models were later conditioned by the same training images and facies probability function used in MPS model. Facies probability function expresses the relationship between facies log and TIs and becomes important away from hard data points. Generated models where then compared with the original stratigraphic section by taking a slice from the facies model at the same location of the stratigraphic section.

**Sequential Indicator Simulation**

Several realizations of the 3D facies model were generated using SIS and were all somewhat similar with randomly distributed lithofacies without following controls such as water-depth sensitivity or windward-leeward effect (Fig. 4.9). Although SIS-generated lithofacies models are statistically possible, they are geologically improbable. For example, basinal and slope deposits were distributed across the platform top, and similarly shallow-water lithofacies were distributed in basinal position. Several trials of adjusting variograms and generating models using SIS failed to produce acceptable results.

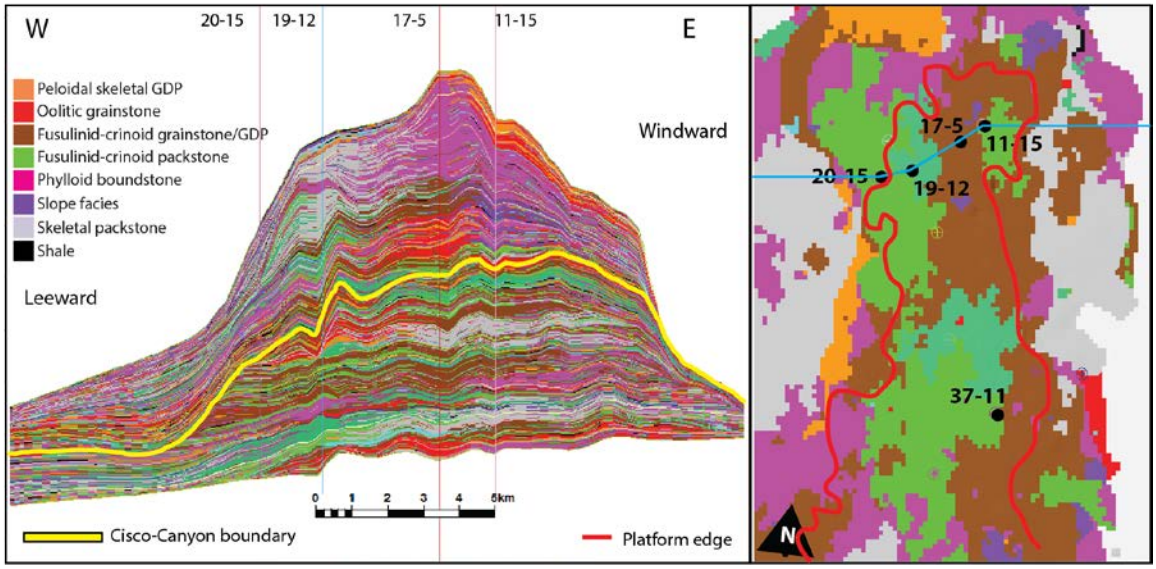


**Fig. 4.9**: An east-west slice of 3D facies models and map view at the top of the Canyon generated by Sequential Indicator Simulation. Facies distribution is unrealistic where platform top facies are distributed in in the basin whereas basinal facies are almost absent.

Sequential Indicator Simulation with Trends is a variation of the simple SIS methods which allows the use of TIs and locally variable proportional model (Daly and Verly, 1994; Sweet et al., 1996). SIS with Trends produced a more acceptable facies model (Fig. 4.10) that captured stratigraphic trends and reservoir heterogeneity similar to the MPS-generated lithofacies model. Although a geologically probable lithofacies distribution and trends were observed when training images and facies probability functions were introduced to the SIS as a secondary input, improbable facies distribution are still present, e.g., slope deposits on platform top with sharp facies boundaries (Fig. 4.10). Nonetheless, facies outliers may be improved by adjusting the weights of lithofacies probability cube in the software algorithm.

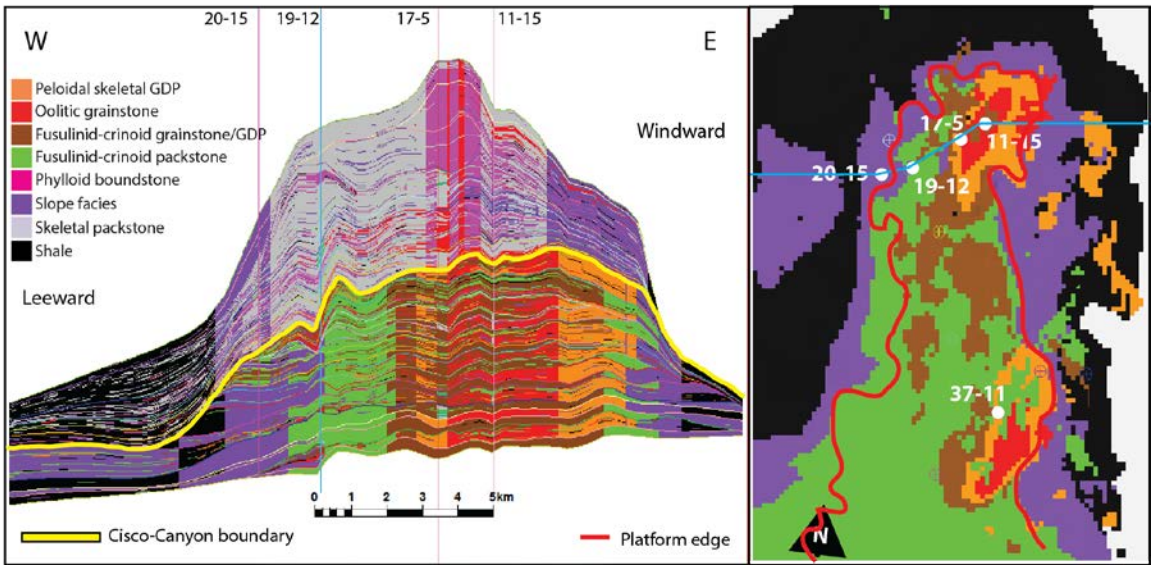


**Fig. 4.10**: An east-west slice of 3D facies models and map view at the top of the Canyon generated by Sequential Indicator Simulation with Trend. Overall, facies distribution is comparable to conceptual model but inconsistencies still exist. Platform top facies were distributed in basinal positions.

**Truncated Gaussian Simulation**

TGS produced unreasonable 3D facies model where deep-water, low-energy depositional facies were distributed across the platform top where shallow-water, high energy depositional facies are expected (Fig. 4.11). When training images and facies probability functions were incorporated in the TGS, a more geologically-sound facies model was produced (Fig. 4.12). However, unconditioned TGS shows better facies boundaries with gradual facies transitioning compared to sharp and poorly handled facies boundaries in TI-incorporated TGS. The sharp facies truncation at facies boundaries supports the earlier notion that this artifact is a result of overly generalized TIs. In addition,

the weight of lithofacies probability cubes functions were set high to force facies distribution to follow training images trends.

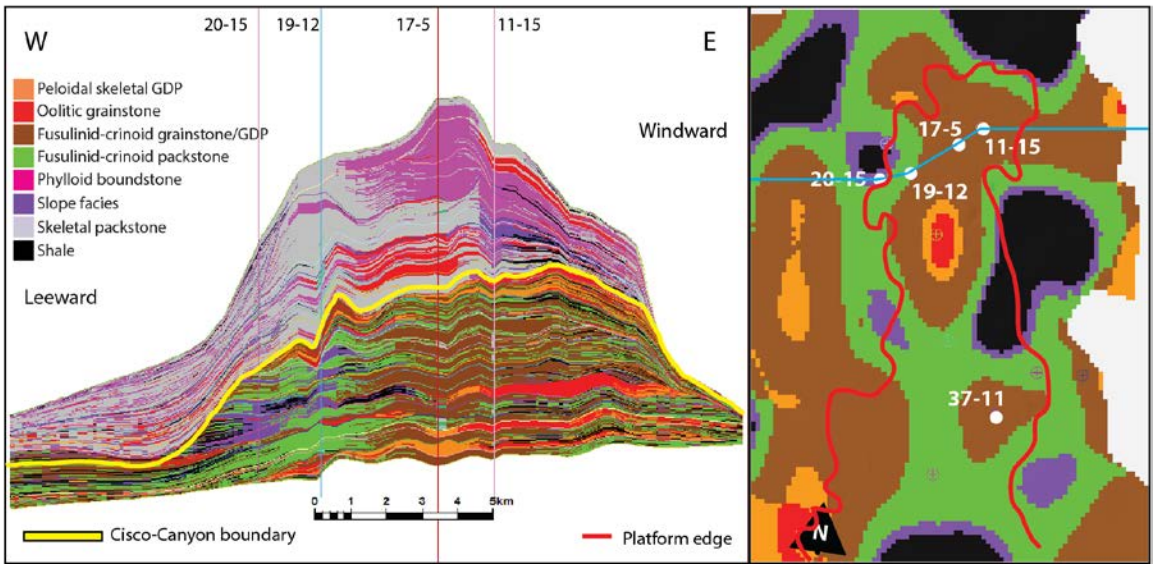


**Fig. 4.11**: An east-west slice of 3D facies models and map view at the top of the Canyon generated by Truncated Gaussian Simulation. TGS generated models in which facies distribution was unreasonable. Platform top facies were distributed in basinal positions whereas basinal facies were distributed on platform top.

Examining the different models and comparing them to the core-based stratigraphic section (Fig. 4.3) indicate that MPS is the best modeling method that produced the most robust geological model for the complex architecture of the SACROC platform. Improving the results of MPS will require incorporating more data from the subsurface and outcrop analogs and producing a single training image for each modeled zone.

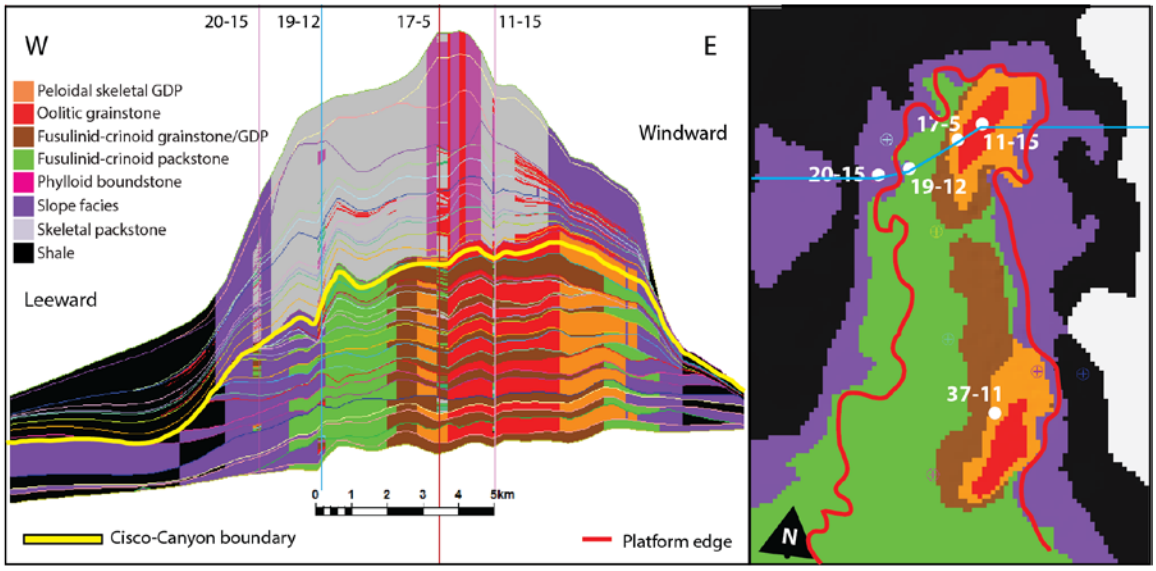


**Fig. 4.12**: An east-west slice of 3D facies models and map view at the top of the Canyon generated by Truncated Gaussian Simulation with training images and facies probability functions. Discrete facies probability cube resulted in sharp facies boundaries.

**Petrophysical Analysis and modeling**

Correlation between depositional lithofacies and porosity reflects that original fabric governs porosity distribution. Analysis of plug-measured and log-derived porosity data and calculated permeability show that the best reservoir units are within the shoal lithofacies associations (Fig. 4.7) (up to 28% porosity, average 14%; up to 250 mD permeability, average 20 mD), and to a lesser extent phylloid boundstone (Fig. 4.7) (up to 30% porosity, average 11%; up to 200 mD, average 8 mD). Further, the slope facies association (Fig. 4.7) has heterogeneous petrophysical properties that can range from good to very poor.

Both porosity and calculated permeability logs were conditioned to facies and then were upscaled using arithmetic and geometric averaging respectively. Facies conditioning

was based on MPS deterministic facies model because specific facies association, e.g., shoal facies association, have better reservoir potential than others (*cf.* slope facies association).

Several model realizations of porosity distributions were generated using Sequential Gaussian Simulation (SGS) and these showed consistent porosity patterns with high porosities in grain-dominated lithofacies (Fig. 4.13). Similarly, permeability modeling showed the best result using SGS collocated cokriging within the porosity cube since permeability is highly correlated with porosity in this dataset (Fig. 4.14). Models show that the eastern (windward) side of the platform top shows the best reservoir potential within the grainstones of shoal and middle shelf facies associations in the Canyon and healthy phylloid mound association in the Cisco. In addition, the western (leeward) side of the platform shows good reservoir potential in localized areas off the platform. These correlate well with concentrated density flows grainstones and coarse-grained turbidites of the slope facies association and may have potential similar to slope deposits of the Cretaceous Poza

Rica field (Enos, 1985).

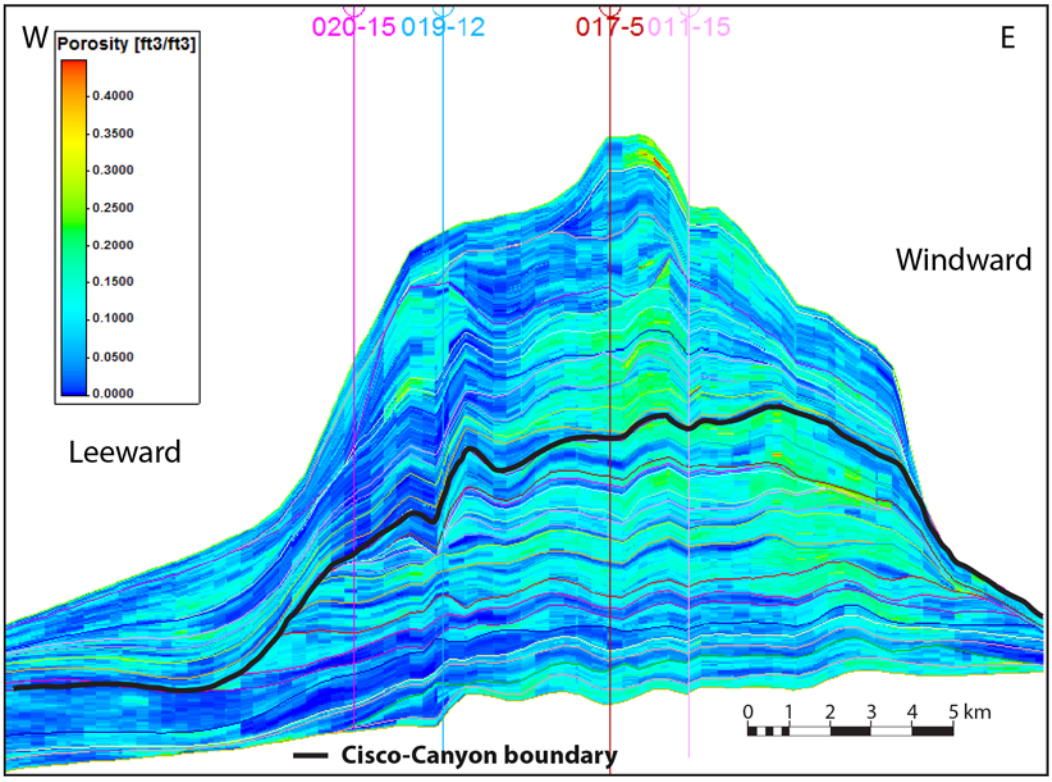


**Fig. 4.13**: Petrophysical model showing the distribution of porosity using Sequential Gaussian Simulation. Transgressive hemi-cycles in the Canyon tend to be tighter and less permeable compared to their regressive counterparts. Model is consistent with expected facies distribution where the windward side will potentially be a site of high-energy, porous grainstones.

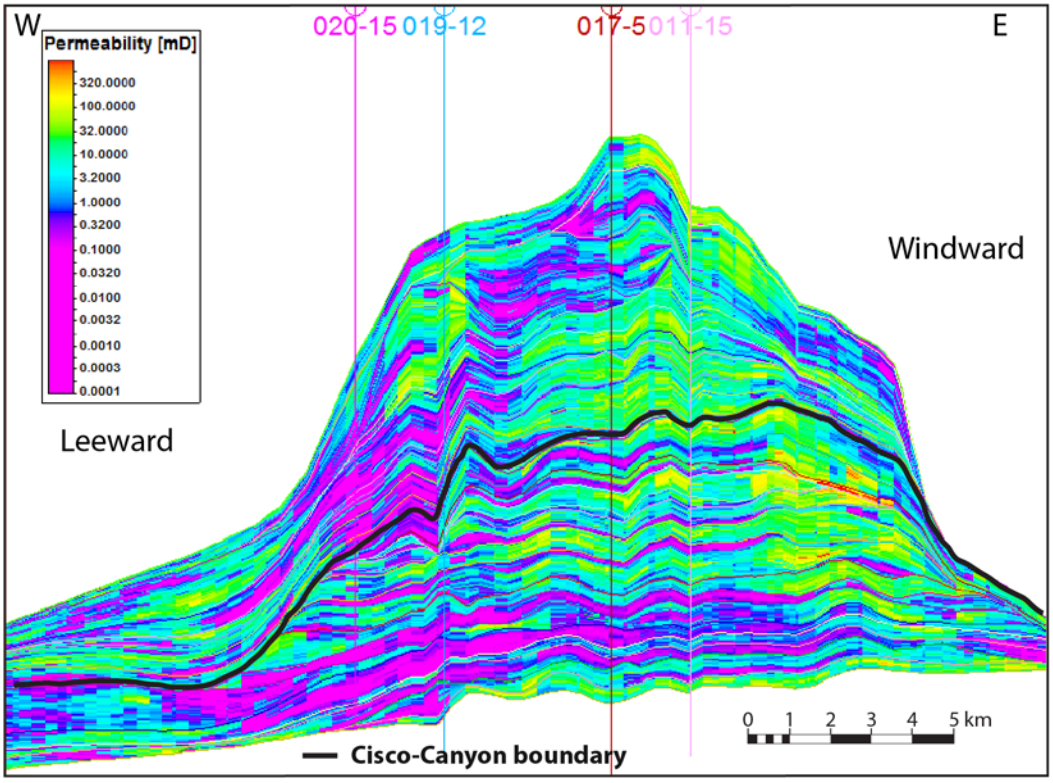


**Fig. 4.14**: Petrophysical model showing permeability distribution using collocated cokriging where permeability field was conditioned to facies-conditioned porosity model. Model suggest that windward is more permeable compared to the leeward side.

A comparison between the 3D facies and petrophysical models demonstrates the complex facies architecture and heterogeneous nature of the reservoir. The heterogeneity may be attributed to two factors. First, the primary control is the complicated distribution of the depositional lithofacies controlled by icehouse climate conditions, especially at peak icehouse during deposition of Cisco facies. The second control is the diagenetic history in response to high-amplitude glacioeustatic fluctuations which can be discordant to stratigraphic surfaces.

The modeling exercises illustrate the importance of having outcrop or modern analogs in constructing geological models. Although the high-resolution sequence stratigraphic framework and well-constrained 3D geological models form the basis for populating reservoir flow units, it is not without flaws. Conceptual models may only qualitatively relate diagenetic fabrics to the stratigraphic framework without quantitative spatial data to accurately populate flow units.

## CONCLUSIONS

Modeling complex icehouse carbonate platforms successfully requires integrating spatial data from outcrop and modern analogs to available subsurface data. Pure stochastic methods are based on inherently poor sampling of the subsurface and therefore produced geologically unreasonable models. A geological understanding, be it an outcrop of modern analog, is a necessary piece to construct conceptual models. These conceptual models can later be converted in TIs that help the modeling software in distributing facies in a geological model in a manner that honors facies relationships. Deterministic MPS modeling approach generated the best-desired results that honor data and facies relationships. Nonetheless, one drawback of this approach is that it can be time-consuming as one TI is required for each stratigraphic zone to produce the best results. Alternatively, when facies models were generated stochastically, facies models failed to distribute facies accurately and failed to honor facies relationships. However, stochastic models produced much more acceptable and comparable results to the deterministic MPS when TIs and facies probability cubes where incorporated to guide the software. Conditioning

petrophysical properties modeling to MPS-generated facies revealed a good correlation between the two. Hence, MPS is the better method for modeling complicated carbonate reservoirs.

# CHAPTER 5: CONCLUSIONS

The stratigraphic record archived in Canyon and Cisco formations of the SACROC field reveals that the Missourian and Virgilian stages of the Late Pennsylvanian are characterized by high-frequency, high-amplitude eustatic fluctuations typifying icehouse settings. The Missourian Canyon Formation consists of 23 grainstone-capped high-frequency cycles dominated by aggradational to progradational stacking patterns, whereas the Virgilian Cisco Formation is composed of 14 high-frequency cycles dominated by retrogradational stacking. The minimum glacioeustatic amplitude estimated for the Canyon is 37 m with an average period of 100 k.y. On the other hand, the Cisco has a minimum glacioeustatic amplitude of 40 m with an average period of 343 k.y.

High-resolution sequence stratigraphic framework of the upper Pennsylvanian Canyon and Cisco units in the SACROC Field was established by integrating core, wireline logs, and 3D seismic data. Four aggradational to progradational, high-frequency sequences composed of several layer-cake, transgressive-regressive cycles characterize the Canyon Formation. Transgressive hemicycles are composed predominantly of fusulinid-crinoid wackestones and packstones, whereas regressive lithofacies are composed of fusulinid-crinoid and ooid grainstones punctuated by several subaerial exposure horizons. Conversely, complex internal stratigraphic architecture characterizes the Cisco succession

with highly juxtaposed shallow- and deep-water facies with multiple subaerial emergence features. Five high-frequency sequences are recognized from 1-D stratigraphic analysis from two cored crestal wells. Establishing correlative timelines between wells is extremely challenging and highly uncertain. The windward margin is net-aggradational owing to on-platform sediment transport, whereas the leeward margin is net-progradational because of the dominant off-platform sediment transport. Different modes of sediment transport controlled the platform's asymmetric morphology and resulted in the development of an accretionary windward margin with steeper upper slopes compared to the leeward margin. This asymmetry is enhanced by early cementation and stabilization of the windward margin.

The wealth of data from SACROC field presented an opportunity to model complex, icehouse carbonate subsurface reservoirs. Several modeling techniques were used to populate 3D facies models. Truncated Gaussian Simulation and Sequential Indicator Simulation produced facies models based on geostatistics from limited data points resulting in improbable geological models. Alternatively, multiple-point statistics algorithm guided by conceptual models that were converted into training images produced geologically sound facies model. Similarly, when TGS and SIS models were conditioned by training images and facies probability cubes, the resulting facies models were comparable but inferior to the one produced by multiple-point statistics method. The most accepted facies model realization produced by the MPS approach was selected for distributing petrophysical properties of the reservoir. It showed a matching consistency between facies and petrophysical properties. The best reservoir quality was present within

the grain-dominated lithofacies throughout the entire succession, especially in the windward side, as well as within phylloid boundstones in the Cisco Formation. This work demonstrates how integrating outcrop and modern analogs data as well as sequence stratigraphic principles is crucial in constructing geologically sound reservoir models.

## References


Adams, E. W., Grotzinger, J. P., Watters, W. A., Schroder, S., McCormick, D. S., and Al-Siyabi, H. A., 2005, Digital characterization of thrombolite-stromatolite reef distribution in a carbonate ramp system (terminal Proterozoic, Nama Group, Namibia): AAPG Bulletin, v. 89, no. 10, p. 1293-1318.

Adlis, D. S., Grossman, E. L., Yancey, T. E., and McLerran, R. D., 1988, Isotope stratigraphy and paleodepth changes of Pennsylvanian cyclical sedimentary deposits: Palaios, p. 487-506.

Aigner, T., Braun, S., Palermo, D., and Blendinger, W., 2007, 3D geological modelling of a carbonate shoal complex: reservoir analogue study using outcrop data: First Break, v. 25, no. 8, p. 65-72.

Algeo, T. J., and Wilkinson, B. H., 1988, Periodicity of mesoscale Phanerozoic sedimentary cycles and the role of Milankovitch orbital modulation: The Journal of Geology, v. 96, no. 3, p. 313-322.

Alnazghah, M., and Kerans, C., 2018, Late Pennsylvanian glaciation: Evidence of icehouse conditions from Canyon and cisco units, Midland Basin, Texas: Marine and Petroleum Geology, v. 94, p. 198-211.

Bachtel, S. L., Kissling, R. D., Martono, D., Rahardjanto, S. P., Dunn, P. A., and MacDonald, B. A., 2004, Seismic Stratigraphic Evolution of the MiocenePliocene Segitiga Platform, East Natuna Sea, Indonesia: The Origin, Growth, and Demise of an Isolated Carbonate Platform, *in* Eberli, G. P., Masafero, J. L., and Sarg, J. F., eds., Seismic Imaging of Carbonate Reservoirs and Systems, AAPG Memoir, 81, p. 291–308.

Bates, S. M., and Lyons, T. W., A Coupled Oxygen Isotope and Trace Metal Record of Glacioeustatic Sea Level Variation and Enhanced Water Column Productivity, *in* Proceedings 2006 Philadelphia Annual Meeting2006, Volume 38 (7), Geological Society of America Abstracts with Programs, p. 183.

Boardman, D. R., and Heckel, P. H., 1989, Glacial-eustatic sea-level curve for early Late Pennsylvanian sequence in north-central Texas and biostratigraphic correlation with curve for midcontinent North America: Geology, v. 17, no. 9, p. 802-805.

Bosellini, A., 1984, Progradation geometries of carbonate platforms: examples from the Triassic of the Dolomites, northern Italy: Sedimentology, v. 31, no. 1, p. 1-24.

Boss, S. K., and Rasmussen, K. A., 1995, Misuse of Fischer plots as sea-level curves: Geology, v. 23, no. 3, p. 221-224.

Bouttes, N., Paillard, D., Roche, D. M., Brovkin, V., and Bopp, L., 2011, Last Glacial Maximum CO2 and δ13C successfully reconciled: Geophysical Research Letters, v. 38, no. 2.

Broecker, W. S., Peteet, D. M., and Rind, D., 1985, Does the ocean–atmosphere system have more than one stable mode of operation?: Nature, v. 315, no. 6014, p. 21.

Butts, S. H., 2005, Latest Chesterian (Carboniferous) initiation of Gondwanan glaciation recorded in facies stacking patterns and brachiopod paleocommunities of the Antler foreland basin, Idaho: Palaeogeography, Palaeoclimatology, Palaeoecology, v. 223, no. 3-4, p. 275-289.

Chen, B., Joachimski, M. M., Wang, X.-d., Shen, S.-z., Qi, Y.-p., and Qie, W.-k., 2016, Ice volume and paleoclimate history of the Late Paleozoic Ice Age from conodont apatite oxygen isotopes from Naqing (Guizhou, China): Palaeogeography, Palaeoclimatology, Palaeoecology, v. 448, p. 151-161.

Cheng, H., Edwards, R. L., Broecker, W. S., Denton, G. H., Kong, X., Wang, Y., Zhang, R., and Wang, X., 2009, Ice age terminations: science, v. 326, no. 5950, p. 248-252.

Collins, J. F., Kenter, J. A., Harris, P. M., Kuanysheva, G., and Steffen, D. F. K., 2006, Facies and reservoir-quality variations in the late Visean to Bashkirian outer platform, rim, and flank of the Tengiz buildup, Precaspian Basin, Kazakhstan, *in* Harris, P. M., and Weber, L. J., eds., Giant hydrocarbon reservoirs of the world: From rocks to reservoir chacracterization and modeling, AAPG Memoir 88, p. 55-95.

Coniglio, M. I., and Dix, G. R., 1992, Carbonate Slopes, *in* Walker, R. G., and James, N. P., eds., Facies Models: Response to Sea Level Change, Geological Association of Canada, p. 349-373.

Crevello, P. D., and Schlager, W., 1980, Carbonate debris sheets and turbidites, Exuma Sound, Bahamas: Journal of Sedimentary Research, v. 50, no. 4.

Crowell, J., 1978, Gondwanan glaciation, cyclothems, continental positioning, and climate change: American Journal of Science, v. 278, no. 10, p. 1345-1372.

Crowell, J. C., 1999, Pre-Mesozoic ice ages: their bearing on understanding the climate system, Geological Society of America.

Crowley, T. J., 1992, North Atlantic deep water cools the Southern Hemisphere: Paleoceanography, v. 7, no. 4, p. 489-497.

Crowley, T. J., and Baum, S. K., 1991, Estimating Carboniferous sea-level fluctuations from Gondwanan ice extent: Geology, v. 19, no. 10, p. 975-977.

Cumings, E. R., 1932, Reefs or bioherms?: Bulletin of the Geological Society of America, v. 43, no. 1, p. 331-352.

Della Porta, G., Kenter, J. A., and Bahamonde, J. R., 2004, Depositional facies and stratal geometry of an Upper Carboniferous prograding and aggrading high-relief carbonate platform (Cantabrian Mountains, N Spain): Sedimentology, v. 51, no. 2, p. 267-295.

DeLong, E. F., Preston, C. M., Mincer, T., Rich, V., Hallam, S. J., Frigaard, N.U., Martinez, A., Sullivan, M. B., Edwards, R., Brito, B. R., Chisholm, S. W., and

Karl, D. M., 2006, Community Genomics Among Stratified Microbial Assemblages in the Ocean's Interior, Science, v. 311(5760), p. 496-503

Donovan, D., and Jones, E., 1979, Causes of world-wide changes in sea level: Journal of the Geological Society, v. 136, no. 2, p. 187-192.

Drew, E. E., and Abel, K. K., Biology, sedimentology and geography of the vast inter-reefal {Halimeda} meadows within the Great Barrier Reef Province, *in* Proceedings Proceedings of the 5th International Coral Reef Congress, Tahiti, 27 May-1 June 1985-pages: 5: 15-201985.

Dutton, S. P., Kim, E. M., Broadhead, R. F., Raatz, W. D., Breton, C. L., Ruppel, S. C., and Kerans, C., 2005, Play analysis and leading-edge oil-reservoir development methods in the Permian basin: Increased recovery through advanced technologies: AAPG Bulletin, v. 89, no. 5, p. 553-576.

Dyer, B., and Maloof, A. C., 2015, Physical and chemical stratigraphy suggest small or absent glacioeustatic variation during formation of the Paradox Basin cyclothems: Earth and Planetary Science Letters, v. 419, p. 63-70.

Eberli, G., and Grammer, G., Unfilled accommodation space—a fundamental problem for cyclostratigraphy, *in* Proceedings Am. Assoc. Petrol. Geol. Annual Convention, San Antonio, TX1999, Volume 36.

Eberli, G. P., 2013, The uncertainties involved in extracting amplitude and frequency of orbitally driven sea -level fluctuations fror Sedimentology, v. 60, no. 1, p. 64-84.

Eberli, G. P., and Ginsburg, R. N., 1989, Cenozoic Progradation of Northwestern Great Bahama Bank, a Record of Lateral Platform Growth and Sea-Level Fluctuations, *in* Crevello, P. D., Wilson, J. L., Sarg, J. F., and Read, J. F., eds., Controls on Carbonate Platform and Basin Development, Soc. Econ. Paleontol. Mineral. Spec. Publ., 44, p. 339-351.

Egenhoff, S. O., Peterhänsel, A., Bechstädt, T., Zühlke, R., and Grötsch, J., 1999, Facies architecture of an isolated carbonate platform: tracing the cycles of the Latemar (Middle Triassic, northern Italy): Sedimentology, v. 46, no. 5, p. 893-912.

Embry III, A. F., and Klovan, J. E., 1971, A late Devonian reef tract on northeastern Banks Island, NWT: Bulletin of Canadian Petroleum Geology, v. 19, no. 4, p. 730-781.

Emiliani, C., 1955, Pleistocene temperatures: The Journal of Geology, v. 63, no. 6, p. 538-578.

Emiliani, C., and Ericson, D. B., 1991, The glacial/interglacial temperature range of the surface water of the oceans at low latitudes: Stable Isotope Geochemistry: A Tribute to Samuel Epstein. Geochem Soc Spec Publ, v. 3, p. 223-228.

Enos, P., 1985, Cretaceous debris reservoirs, Poza Rica Field, Veracruz, México, *in* Roehl, P. O., and Choquette, P. W., eds., Carbonate Petroleum Reservoirs, Springer, p. 455-469.

Epstein, S., Buchsbaum, R., Lowenstam, H. A., and Urey, H. C., 1953, Revised carbonate-water isotopic temperature scale: Geological Society of America Bulletin, v. 64, no. 11, p. 1315-1326.

Eros, J., Montañez, I., Osleger, D., Davydov, V., Nemyrovska, T., Poletaev, V., and Zhykalyak, M., 2012, Sequence stratigraphy and onlap history of the Donets Basin, Ukraine: insight into Carboniferous icehouse dynamics: Palaeogeography, Palaeoclimatology, Palaeoecology, v. 313, p. 1-25.

Fairbanks, R. G., 1989, A 17,000-year glacio-eustatic sea level record: influence of glacial melting rates on the Younger Dryas event and deep-ocean circulation: Nature, v. 342, p. 637.

Feldman, H. R., Franseen, E. K., Joeckel, R., and Heckel, P. H., 2005, Impact of longer-term modest climate shifts on architecture of high-frequency sequences (cyclothems), Pennsylvanian of Midcontinent USA: Journal of Sedimentary Research, v. 75, no. 3, p. 350-368.

Fielding, C. R., Frank, T. D., Birgenheier, L. P., Rygel, M. C., Jones, A. T., and Roberts, J., 2008, Stratigraphic imprint of the Late Palaeozoic Ice Age in eastern Australia: a record of alternating glacial and nonglacial climate regime: Journal of the Geological Society, v. 165, no. 1, p. 129-140.

Fisher, A., 1964, The Lofer cyclothems of the alpine Triassic: Bulletin Kansas Geological Survey, v. 169, p. 107-149.

Flügel, E., 2004, Microfacies of Carbonate Rocks: Analysis, Interpretation and Application, Springer, 1006 p.:

Frakes, L. A., Francis, J. E., and Syktus, J. I., 2005, Climate modes of the Phanerozoic, Cambridge University Press.

Frazier, W. J., and Schwimmer, D. R., 1987, Regional Stratigraphy of North America, Plenum Press New York and London.

Freile, D., Milliman, J., and Hillis, L., 1995, Leeward bank margin Halimeda meadows and draperies and their sedimentary importance on the western Great Bahama Bank slope: Coral Reefs, v. 14, no. 1, p. 27-33.

Frenzel, H., Bloomer, R., Cline, R., Cys, J., Galley, J., Gibson, W., Hills, J., King, W., Seager, W., and Kottlowski, F., 1988, The Permian basin region: Sedimentary cover—North American craton: US: Boulder, Colorado, Geological Society of America, The Geology of North America, v. 2, p. 261-306.

Galley, J. E., 1958, Oil and geology in the Permian basin of Texas and New Mexico: North America, *in* Weeks, L. G., ed., Habitat of oil: a symposium, American Association of Petroleum Geologists.

Galli, A., Le Loch, G., Geffroy, F., and Eschard, R., 2006, An application of the truncated pluri-gaussian method for modeling geology, *in* Coburn, T. C., Yarus, J. M., and Chambers, R. L., eds., Stochastic modeling and geostatistics: Principles, methods, and case studies, volume II, AAPG Computer Applications in Geology (No. 5), p. 102-122.

Galloway, W., Ewing, T., Garrett, C., Tyler, N., and Bebout, D., 1983, Atlas of major Texas oil reservoirs, The University of Texas at Austin, Bureau of Economic Geology Atlas 139 p.:

Gischler, E., 1995, Current and wind induced facies patterns in a Devonian atoll: Iberg Reef, Harz Mts., Germany: Palaios, p. 180-189.

Goldhammer, R., Dunn, P., and Hardie, L., 1990, Depositional cycles, composite sea-level changes, cycle stacking patterns, and the hierarchy of stratigraphic forcing: examples from Alpine Triassic platform carbonates: Geological Society of America Bulletin, v. 102, no. 5, p. 535-562.
Goldhammer, R., Oswald, E., and Dunn, P., 1991, Hierarchy of stratigraphic forcing: Example from Middle Pennsylvanian shelf carbonates of the Paradox Basin: Sedimentary Modeling: Computer Simulations and Methods for Improved Parameter Definition: Kansas Geological Survey, Bulletin, v. 233, p. 361-413.
Goldstein, R. H., 1988, Cement stratigraphy of Pennsylvanian Holder Formation, Sacramento Mountains, New Mexico: AAPG Bulletin, v. 72, no. 4, p. 425-438.
Golonka, J., 2011, Phanerozoic palaeoenvironment and palaeolithofacies maps of the Arctic region: Geological Society, London, Memoirs, v. 35, no. 1, p. 79-129.
Gradstein, F. M., Ogg, J. G., Schmitz, M., and Ogg, G., 2012, The geologic time scale 2012, elsevier.
Grammer, G. M., and Ginsburg, R. N., 1992, Highstand versus lowstand deposition on carbonate platform margins: insight from Quaternary foreslopes in the Bahamas: Marine Geology, v. 103, no. 1-3, p. 125-136.
Grammer, G. M., Ginsburg, R. N., Swart, P. K., McNeill, D. F., Jull, A. T., and Prezbindowski, D. R., 1993, Rapid growth rates of syndepositional marine aragonite cements in steep marginal slope deposits, Bahamas and Belize: Journal of Sedimentary Research, v. 63, no. 5.
Grötsch, J., and Mercadier, C., 1999, Integrated 3-D reservoir modeling based on 3-D seismic: the Tertiary Malampaya and Camago buildups, offshore Palawan, Philippines: AAPG Bulletin, v. 83, no. 11, p. 1703-1728.
Grotzinger, J., 1986, Upward shallowing platform cycles: A response to 2.2 billion years of low
vacuole), high-frequency (Milanko
Paleoceanography, v. 1, no. 4, p. 403-416.
Hadi, J., Harrison, C., Keller, J., and Rejeki, S., Overview of Darajat reservoir characterization: a volcanic hosted reservoir, *in* Proceedings Antalya, Turkey, Proceedings of the World Geothermal Congress2005, p. 11.
Hambrey, M. J., 1981, Late Palaeozoic Glacigenic Sediments in the Galilee and Bowen Basins, Queensland, *in* Hambrey, M. J., and Harland, W. B., eds., Earth's Pre-Pleistocene Glacial Record, Cambridge University Press, p. 474-475.
Harland, W., Cox, A., Llewellyn, P., Pickton, C., Smith, A., and Walters, R., 1982, 1982 A geologic time scale, Cambridge, England, Cambridge University Press.
Harris, P. M. M., and Vlaswinkel, B. M., 2008, Quantifying facies attributes of the Caicos platform: AAPG, Search and Discovery Article # 50079, p. 8.
Hawkins, J. T., Benvegnu, A. J., Wingate, T. P., McKamie, J. D., Pickard, C. D., and Altum, J. T., 1996, SACROC Unit CO2 Flood: Multidisciplinary Team Improves Reservoir Management and Decreases Operating Costs: SPE Reservoir Engineering, p. 141-148.
Hays, J. D., Imbrie, J., and Shackleton, N. J., Variations in the Earth's orbit: pacemaker of the ice ages1976, American Association for the Advancement of Science Washington, DC.

Heckel, P. H., 1977, Origin of phosphatic black shale facies in Pennsylvanian cyclothems of mid-continent North America: AAPG Bulletin, v. 61, no. 7, p. 1045-1068.
-, 1986, Sea-level curve for Pennsylvanian eustatic marine transgressive-regressive depositional cycles along midcontinent outcrop belt, North America: Geology, v. 14, no. 4, p. 330-334.
Heckel, P. H., Dennison, J., and Ettensohn, F., 1994, Evaluation of evidence for glacio-eustatic control over marine Pennsylvanian cyclothems in North America and consideration of possible tectonic effects: Tectonic and Eustatic Controls on Sedimentary Cycles: SEPM, Concepts in Sedimentology and Paleontology, v. 4, p. 65-87.
Heckel, P. H., Gibling, M. R., and King, N. R., 1998, Stratigraphic model for glacial-eustatic Pennsylvanian cyclothems in highstand nearshore detrital regimes: The Journal of Geology, v. 106, no. 4, p. 373-384.
Hills, J. M., 1970, Late Paleozoic structural directions in southern Permian basin, west Texas and southeastern New Mexico: AAPG Bulletin, v. 54, no. 10, p. 1809-1827.
-, 1984, Sedimentation, tectonism, and hydrocarbon generation in Delaware basin, west Texas and southeastern New Mexico: AAPG Bulletin, v. 68, no. 3, p. 250-267.
-, 1985, Structural evolution of the Permian basin of west Texas and New Mexico: Structure and tectonics of trans-Pecos Texas: West Texas Geological Society Publication, p. 85-81.
Horak, R. L., 1985, Trans-Pecos tectonism and its affects on the Permian Basin: Structure and Tectonics of Trans-Pecos Texas: Midland, Texas, West Texas Geological Society, p. 81-87.
Horton, D. E., Poulsen, C. J., Montañez, I. P., and DiMichele, W. A., 2012, Eccentricity-paced late Paleozoic climate change: Palaeogeography, Palaeoclimatology, Palaeoecology, v. 331, p. 150-161.
Howard, R. H., and Whitaker, S. T., 1988, Hydrocarbon accumulation in a paleovalley at Mississippian-Pennsylvanian unconformity near Hardinville, Crawford County, Illinois: a model paleogeomorphic trap: Illinois petroleum no. 129.
Isbell, J. L., Miller, M. F., Wolfe, K. L., and Lenaker, P. A., 2003, Timing of late Paleozoic glaciation in Gondwana: Was glaciation responsible for the development of Northern Hemisphere cyclothems?: Special papers-geological society of America, p. 5-24.
James, N. P., and Jones, B., 2015, Origin of Carbonate Rocks, John Wiley & Sons, 467 p.:
James, N. P., and Mountjoy, E. W., 1983, Shelf-Slope Break in Fossil Carbonate Platforms: An Overview, *in* Stanley, D. J., and Moore, G. T., eds., The Shelf-Break:Critical Interface on Continental Margins, Volume 33, Soc. Econ. Paleontol. Miner. Spec. Publ., p. 189-206.
Janson, X., 2007, Day 3: Late Carboniferous (Virgilian) Ice-house cycle architecture and phylloid algae mound development, *in* Kerans, C., Janson, X., and Bellian, J., eds., Linking depositional, diagenetic, facies, stratal geometries and cycle architecture: examples for Paleozoic carbonate systems of West Texas and

southern New Mexico, The University of Texas at Austin, Bureau of Economic Geology, RCRL Spring Field Course Guide, p. 63-110.
Janson, X., and Kerans, C., 2007, Day 4: Deeper water mud mounds and crinoidal turbidites-Mississippian Lake Valley Formation, Sacramento Mountains-analog for Cisco reservoir in SACROC and Cogdell, *in* Kerans, C., Janson, X., and Bellian, J., eds., LinkLinking depositional, diagenetic, facies, stratal geometries and cycle architecture: examples for Paleozoic carbonate systems of West Texas and southern New Mexico, The University of Texas at Austin, Bureau of Economic Geology, RCRL Spring Field Course Guide, p. 111–161.
Janson, X., and Madriz, D. D., 2012, Geomodelling of carbonate mounds using two-point and multipoint statistics: Geological Society, London, Special Publications, v. 370, no. 1, p. 229-246.
Joachimski, M. M., von Bitter, P. H., and Buggisch, W., 2006, Constraints on Pennsylvanian glacioeustatic sea-level changes using oxygen isotopes of conodont apatite: Geology, v. 34, no. 4, p. 277-280.
Jones, A. T., and Fielding, C. R., 2004, Sedimentological record of the late Paleozoic glaciation in Queensland, Australia: Geology, v. 32, no. 2, p. 153-156.
-, 2008, Sedimentary facies of a glacially influenced continental succession in the Pennsylvanian Jericho Formation, Galilee Basin, Australia: Sedimentology, v. 55, no. 3, p. 531-556.
Kendall, C. G. S. C., and Schlager, W., 1981, Carbonates and relative changes in sea level: Marine geology, v. 44, no. 1-2, p. 181-212.
Kenter, J. A., 1990, Carbonate Platform Flanks: Slope Angle and Sediment Fabric: Sedimentology, v. 37, no. 5, p. 777-794.
Kenter, J. A., Harris, P. M. M., and Della Porta, G., 2005, Steep microbial boundstone-dominated platform margins—examples and implications: Sedimentary Geology, v. 178, no. 1-2, p. 5-30.
Kerans, C., 1995, Use of one-and two-dimensional cycle analysis in establishing high-frequency sequence frameworks, *in* Read, J. F., Kerans, C., Weber, L. J., Sarg, J. F., and Wright, F. M., eds., Milankovitch Sea-Level Changes, Cycles, and Reservoirs on Carbonate Platforms in Greenhouse and Ice-House Worlds, Volume 35, Part 2, SEPM, p. 1-20.
-, 2001, Stratigraphic and diagenetic controls on reservoir architecture of a non-reefal icehouse isolated platform—Sacroc unit: Horseshoe atoll, Texas (abs.): AAPG Bulletin, v. 85, p. 386-387.
Kerans, C., and Fitchen, W. M., 1995, Sequence hierarchy and facies architecture of a carbonate-ramp system: San Andres Formation of Algerita Escarpment and western Guadalupe Mountains, West Texas and New Mexico, Bureau of Economic Geology, University of Texas at Austin, Report of Investigations, 86 p.:
Kerans, C., and Tinker, S. W., 1997, Sequence stratigraphy and characterization of carbonate reservoirs, SEPM, Short Course, 130 p.:
Kidder, D. L., and Worsley, T. R., 2012, A human-induced hothouse climate: GSA Today, v. 22, no. 2, p. 4-11.

Kirkland, B., Moore Jr, C., and Dickson, J., 1993, Well preserved, aragonitic phylloid algae (Eugonophyllum, Udoteaceae) from the Pennsylvanian Holder Formation, Sacramento Mountains, New Mexico: Palaios, p. 111-120.

Klein, G. D., 1996, Depth determination and quantitative distinction of the influence of tectonic subsidence and climate on changing sea level during deposition of Midcontinent Pennsylvanian cyclothems, Models for Carbonate Stratigraphy from Miocene Reef Complexes of Mediterranean Regions, Soc. Econ. Paleontol. Mineral. Spec. Publ., Concepts of Sedimentology and Paleontology # 4
p. 35-50.

Kluth, C. F., 1986, Plate tectonics of the Ancestral Rocky Mountains: Part III. Middle Rocky Mountains, *in* Peterson, J. A., ed., Paleotectonics and Sedimentation in the Rocky Mountain Region, United States, AAPG Memoir, 41, p. 353-369.

Koch, J. T., and Frank, T. D., 2011, The Pennsylvanian–Permian transition in the low-latitude carbonate record and the onset of major Gondwanan glaciation: Palaeogeography, Palaeoclimatology, Palaeoecology, v. 308, no. 3-4, p. 362-372.

Kraft, M. T., and Sangree, J., Seismic Stratigraphy in Carbonate Rocks: Depositional History of the Natuna D-Alpha Block (L-Structure): Stage II, *in* Proceedings Indonesian Petroleum Association, 11th Annual Convention1982, p. 299–321.

Lea, D. W., Martin, P. A., Pak, D. K., and Spero, H. J., 2002, Reconstructing a 350 ky history of sea level using planktonic Mg/Ca and oxygen isotope records from a Cocos Ridge core: Quaternary Science Reviews, v. 21, no. 1-3, p. 283-293.

Lear, C., Elderfield, H., and Wilson, P., 2000, Cenozoic deep-sea temperatures and global ice volumes from Mg/Ca in benthic foraminiferal calcite: Science, v. 287, no. 5451, p. 269-272.

Lehrmann, D. J., and Goldhammer, R. K., 1999, Secular variation in parasequence and facies stacking patterns of platform carbonates: a guide to application of stacking-patterns analysis in strata of diverse ages and settings, Advances in Carbonate Sequence Stratigraphy: Application to Reservoirs, Outcrops and Models, Volume 63, Soc. Econ. Paleontol. Mineral. Spec. Publ., p. 187-225.

Lillie, R. J., Nelson, K. D., De Voogd, B., Brewer, J. A., Oliver, J. E., Brown, L. D., Kaufman, S., and Viele, G. W., 1983, Crustal structure of Ouachita Mountains, Arkansas: a model based on integration of COCORP reflection profiles and regional geophysical data: AAPG Bulletin, v. 67, no. 6, p. 907-931.

Loreau, J.-P., and Purser, B., 1973, Distribution and ultrastructure of Holocene ooids in the Persian Gulf, The Persian Gulf, Springer, p. 279-328.

Lucia, F. J., 1995, Rock-fabric/petrophysical classification of carbonate pore space for reservoir characterization: AAPG Bulletin, v. 79, no. 9, p. 1275-1300.

Martin, L. G., Montañez, I. P., and Bishop, J. W., 2012, A paleotropical carbonate-dominated archive of Carboniferous icehouse dynamics, Bird Spring Fm., Southern Great Basin, USA: Palaeogeography, Palaeoclimatology, Palaeoecology, v. 329, p. 64-82.

Matchen, D. L., and Kammer, T. W., 2006, Incised valley fill interpretation for Mississippian Black Hand Sandstone, Appalachian Basin, USA: Implications for

glacial eustasy at Kinderhookian–Osagean (Tn2–Tn3) boundary: Sedimentary Geology, v. 191, no. 1-2, p. 89-113.
McIlreath, I., and James, N., 1978, Facies models 13. Carbonate slopes: Geoscience Canada, v. 5, no. 4.
Melvin, J., Sprague, R. A., and Heine, C. J., 2010, From bergs to ergs: The late Paleozoic Gondwanan glaciation and its aftermath in Saudi Arabia: Late Paleozoic glacial events and postglacial transgressions in Gondwana: Geological Society of America Special Paper, v. 468, p. 37-80.
Miller, D. J., and Eriksson, K. A., 2000, Sequence stratigraphy of Upper Mississippian strata in the central Appalachians: a record of glacioeustasy and tectonoeustasy in a foreland basin setting: AAPG Bulletin, v. 84, no. 2, p. 210-233.
Montañez, I. P., McElwain, J. C., Poulsen, C. J., White, J. D., DiMichele, W. A., Wilson, J. P., Griggs, G., and Hren, M. T., 2016, Climate, p CO 2 and terrestrial carbon cycle linkages during late Palaeozoic glacial–interglacial cycles: Nature Geoscience, v. 9, no. 11, p. 824.
Montañez, I. P., and Poulsen, C. J., 2013, The Late Paleozoic ice age: an evolving paradigm: Annual Review of Earth and Planetary Sciences, v. 41, p. 629-656.
Montañez, I. P., Tabor, N. J., Niemeier, D., DiMichele, W. A., Frank, T. D., Fielding, C. R., Isbell, J. L., Birgenheier, L. P., and Rygel, M. C., 2007, CO2-forced climate and vegetation instability during Late Paleozoic deglaciation: Science, v. 315, no. 5808, p. 87-91.
Morin, J., Desrochers, A., and Beauchamp, B., 1994, Facies Analysis of Lower Permian Platform Carbonates, Sverdrup Basin, Canadian Arctic Archipelago: Facies, v. 31, no. 1, p. 105-130.
Mudelsee, M., and Stattegger, K., 1997, Exploring the structure of the mid-Pleistocene revolution with advanced methods of time-series analysis: Geologische Rundschau, v. 86, no. 2, p. 499-511.
Mulder, T., and Alexander, J., 2001, The Physical Character of Subaqueous Sedimentary Density Flows and Their Deposits: Sedimentology, v. 48, no. 2, p. 269-299.
Mullins, H. T., 1983, Modern Carbonate Slopes and Basins of the Bahamas, *in* Cook, H. E., Hine, A. C., and Mullins, H. T., eds., Platform Margin and Deep Water Carbonates, SEPM Short Course, 12, p. 1-138.
Mullins, H. T., and Cook, H. E., 1986, Carbonate apron models: alternatives to the submarine fan model for paleoenvironmental analysis and hydrocarbon exploration: Sedimentary geology, v. 48, no. 1-2, p. 37-79.
Olszewski, T. D., and Patzkowsky, M. E., 2001, Evaluating taxonomic turnover: Pennsylvanian–Permian brachiopods and bivalves of the North American Midcontinent: Paleobiology, v. 27, no. 4, p. 646-668.
Orme, G., Flood, P. G., and Sargent, G., 1978, Sedimentation trends in the lee of outer (ribbon) reefs, northern region of the Great Barrier Reef province: Phil. Trans. R. Soc. Lond. A, v. 291, no. 1378, p. 85-99.
Osleger, D., and Read, J. F., 1991, Relation of eustasy to stacking patterns of meter-scale carbonate cycles, Late Cambrian, USA: Journal of Sedimentary Research, v. 61, no. 7.

Peltier, W., and Fairbanks, R. G., 2006, Global glacial ice volume and Last Glacial Maximum duration from an extended Barbados sea level record: Quaternary Science Reviews, v. 25, no. 23-24, p. 3322-3337.

Peterson, J. A., 1966, Stratigraphic vs. structural controls on carbonate-mound hydrocarbon accumulation, Aneth area, Paradox Basin: AAPG Bulletin, v. 50, no. 10, p. 2068-2081.

-, 1992, Aneth Field--USA Paradox Basin, Utah, *in* Foster, N. H., and Beaumont, E. A., eds., Stratigraphic Traps III, AAPG Treatise of Petroleum Geology-Atlas of Oil and Gas Field.

Playford, P. E., 1980, Devonian "Great Barrier Reef" of Canning Basin: Western Australia: AAPG Bulletin, v. 64, no. 6, p. 814-840.

Playton, T. E., Janson, X., and Kerans, C., 2010, Carbonate Slopes, *in* James, N. P., and Dalrymple, R. W., eds., Facies Models 4, Geological Association of Canada, p. 449-476.

Playton, T. E., and Kerans, C., 2015, Late Devonian Carbonate Margins and Foreslopes of the Lennard Shelf, Canning Basin, Western Australia, Part A: Development During Backstepping and the Aggradation-To-Progradation Transition: Journal of Sedimentary Research, v. 85, no. 11, p. 1334-1361.

Poole, F. G., Perry, W. J., Madrid, R. J., and Amaya-Martínez, R., 2005, Tectonic synthesis of the Ouachita-Marathon-Sonora orogenic margin of southern Laurentia: Stratigraphic and structural implications for timing of deformational events and plate-tectonic model: Geological Society of America Special Papers, v. 393, p. 543-596.

Raatz, W. D., and Simo, J., 1998, The Beeman Formation (Upper Pennsylvanian) of the Sacramento Mountains, New Mexico—guide to the Dry Canyon area with discussion on shelf and basin responses to eustasy, tectonics, and climate: Las Cruces country II: New Mexico Geological Society, Guidebook, v. 49, p. 161-176.

Rankey, E. C., Bachtel, S. L., and Kaufman, J., 1999, Controls on Stratigraphic Architecture of Icehouse Mixed Carbonate-Siliciclastic Systems: A Case Study From the Holder Formation (Pennsylvanian, Virgillan), Sacramento Mountains, New Mexico, *in* Harris, P. M. M., Saller, A. H., and Simo, J. A. T., eds., Advances in carbonate sequence stratigraphy : application to reservoirs, outcrops and models, Soc. Econ. Paleontol. Mineral. Spec. Publ., 63.

Read, J., 1995, Overview of carbonate platform sequences, cycle stratigraphy and reservoirs in greenhouse and icehouse worlds, *in* Read, J. F., Kerans, C., Weber, L. J., Sarg, J. F., and Wright, F. M., eds., Milankovitch Sea-Level Changes, Cycles, and Reservoirs on Carbonate Platforms in Greenhouse and Ice-House Worlds, Volume 35, Part 1, SEPM, p. 102.

Read, J., and Goldhammer, R., 1988, Use of Fischer plots to define third-order sea-level curves in Ordovician peritidal cyclic carbonates, Appalachians: Geology, v. 16, no. 10, p. 895-899.

Read, J. F., 1985, Carbonate Platform Facies Models: AAPG Bulletin, v. 69, no. 1, p. 1-21.

-, 1998, Phanerozoic carbonate ramps from greenhouse, transitional and ice-house worlds: clues from field and modelling studies: Geological Society, London, Special Publications, v. 149, no. 1, p. 107-135.
Read, J. F., Osleger, D., Elrick, M., Franseen, E., Watney, W., Kendall, C., and Ross, W., 1991, Two-dimensional modeling of carbonate ramp sequences and component cycles: Sedimentary modeling: Computer simulations and methods for improved parameter definition: Kansas Geological Survey Bulletin, v. 233, p. 473-488.
Reid, A., and Reid, S. T., 1991, The Cogdell field study, Kent and Scurry counties, Texas: A post-mortem: Permian Basin Plays, Tomorrow's Technology Today: Midland, Texas, West Texas Geological Society, Publication, p. 89-91.
Roberts, J., 1983, Australia, *in* Díaz, C. M., Wagner, R. H., Prins, C. F. W., and Granados, L. F., eds., The Carboniferous of the World, Volume 20, Instituto Geologico y Minero de Espana, p. 9-146.
Ronchi, P., Ortenzi, A., Borromeo, O., Claps, M., and Zempolich, W. G., 2010, Depositional setting and diagenetic processes and their impact on the reservoir quality in the late Visean–Bashkirian Kashagan carbonate platform (Pre-Caspian Basin, Kazakhstan): AAPG Bulletin, v. 94, no. 9, p. 1313-1348.
Rygel, M. C., Fielding, C. R., Frank, T. D., and Birgenheier, L. P., 2008, The magnitude of Late Paleozoic glacioeustatic fluctuations: a synthesis: Journal of Sedimentary Research, v. 78, no. 8, p. 500-511.
Saller, A. H., Dickson, J., and Boyd, S. A., 1994, Cycle stratigraphy and porosity in Pennsylvanian and Lower Permian shelf limestones, eastern Central Basin Platform, Texas: AAPG Bulletin, v. 78, no. 12, p. 1820-1842.
Saller, A. H., Dickson, J., and Matsuda, F., 1999, Evolution and distribution of porosity associated with subaerial exposure in upper Paleozoic platform limestones, west Texas: AAPG bulletin, v. 83, no. 11, p. 1835-1854.
Sanders, D., 1996, Rudist biostromes on the margin of an isolated carbonate platform: the Upper Cretaceous of Montagna della Maiella, Italy: Eclogae Geologicae Helvetiae, v. 89, no. 2, p. 845-871.
Schatzinger, R. A., 1983, Phylloid algal and sponge-bryozoan mound-to-basin transition: A late Paleozoic facies tract from the Kelly-Snyder field, West Texas, *in* Harris, P. M., ed., Carbonate Buildups-A Core Workshop, SEPM Core Workshop Notes, 4, p. 244-303.
-, 1988, Changes in facies and depositional environments along and across the trend of Horseshoe Atoll, Scurry and Kent Counties, Texas: Permian and Pennsylvanian Stratigraphy Midland Basin, West Texas: Studies to Aid Hydrocarbon Exploration: Permian Basin Section, Society for Economic Paleontologists and Mineralogists Publication, p. 28-88.
Schepers, K. C., Gonzalez, R. J., Koperna, G. J., and Oudinot, A. Y., Reservoir modeling in support of shale gas exploration, *in* Proceedings Latin American and Caribbean Petroleum Engineering Conference2009, Society of Petroleum Engineers.
Schieber, J. r., and Baird, G., 2001, On the origin and significance of pyrite spheres in Devonian black shales of North America: Journal of Sedimentary Research, v. 71, no. 1, p. 155-166.

Schlager, W., and Camber, O., 1986, Submarine slope angles, drowning unconformities, and self-erosion of limestone escarpments: Geology, v. 14, no. 9, p. 762-765.
Schlager, W., and Chermak, A., 1979, Sediment facies of platform-basin transition, Tongue of the Ocean, Bahamas: Soc. Econ. Paleontol. Mineral. Spec. Publ., v. 27, p. 193-208.
Schrag, D. P., Adkins, J. F., McIntyre, K., Alexander, J. L., Hodell, D. A., Charles, C. D., and McManus, J. F., 2002, The oxygen isotopic composition of seawater during the Last Glacial Maximum: Quaternary Science Reviews, v. 21, no. 1-3, p. 331-342.
Shackleton, N., 1967, Oxygen isotope analyses and Pleistocene temperatures re-assessed: Nature, v. 215, no. 5096, p. 15.
Shackleton, N., and Matthews, R., 1977, Oxygen isotope stratigraphy of Late Pleistocene coral terraces in Barbados: Nature, v. 268, no. 5621, p. 618.
Shakun, J. D., Clark, P. U., He, F., Marcott, S. A., Mix, A. C., Liu, Z., Otto-Bliesner, B., Schmittner, A., and Bard, E., 2012, Global warming preceded by increasing carbon dioxide concentrations during the last deglaciation: Nature, v. 484, no. 7392, p. 49.
Sigman, D. M., and Boyle, E. A., 2000, Glacial/interglacial variations in atmospheric carbon dioxide: Nature, v. 407, no. 6806, p. 859.
Smith, J. C., 2010, Kelly-Snyder Oilfield, Handbook of Texas Online, accessed August 07, 2018, http://www.tshaonline.org/handbook/online/articles/doksu.
Smith Jr, L. B., and Read, J. F., 2001, Discrimination of local and global effects on Upper Mississippian stratigraphy, Illinois Basin, USA: Journal of sedimentary Research, v. 71, no. 6, p. 985-1002.
Smithers, S., and Larcombe, P., 2003, Late Holocene initiation and growth of a nearshore turbid-zone coral reef: Paluma Shoals, central Great Barrier Reef, Australia: Coral Reefs, v. 22, no. 4, p. 499-505.
Soreghan, G. S., and Giles, K. A., 1999, Amplitudes of late Pennsylvanian glacioeustasy: Geology, v. 27, no. 3, p. 255-258.
Tinker, S. W., 1998, Shelf-to-basin facies distributions and sequence stratigraphy of a steep-rimmed carbonate margin: Capitan depositional system, McKittrick Canyon, New Mexico and Texas: Journal of Sedimentary Research, v. 68, no. 6.
Toomey, D. F., and Barker, J., Late Pennsylvanian phylloid-algal bioherms, Orogrande basin, south-central New Mexico and West Texas, *in* Proceedings Geology of the Sierra Blanca, Sacramento and Capitan Ranges. New Mexico Geological Society, 42nd Annual Field Conference, Albuquerque1991, p. 213-220.
Tourtelot, H. A., 1979, Black shale; its deposition and diagenesis: Clays and Clay Minerals, v. 27, no. 5, p. 313-321.
Tucker, M. E., and Wright, V. P., 2009, Carbonate Sedimentology, John Wiley & Sons, 496 p.:
Urey, H. C., 1947, The thermodynamic properties of isotopic substances: Journal of the Chemical Society (Resumed), p. 562-581.

Van Wagoner, J. C., Mitchum, R., Campion, K., and Rahmanian, V., 1990, Siliciclastic sequence stratigraphy in well logs, cores, and outcrops: concepts for high-resolution correlation of time and facies, AAPG, Methods in Exploration (No. 7).

VEEVERS, J. t., and Powell, C. M., 1987, Late Paleozoic glacial episodes in Gondwanaland reflected in transgressive-regressive depositional sequences in Euramerica: Geological Society of America Bulletin, v. 98, no. 4, p. 475-487.

Vest Jr, E., 1970, Oil fields of Pennsylvanian-Permian Horseshoe Atoll, West Texas, *in* Halbouty, M. T., ed., Geology of Giant Petroleum Fields, AAPG Memoir, 14, p. 185-203.

Wahlman, G. P., 2002, Upper Carboniferous-Lower Permian (Bashkirian-Kungarian) Mounds and Reefs, *in* Kiessling, W., Flügel, E., and Golonka, J., eds., Phanerozoic Reef Patterns, Soc. Econ. Paleontol. Mineral. Spec. Publ., 72, p. 271-338.

Wahlman, G. P., and Tasker, D. R., 2013, Lower Permian (Wolfcampian) Carbonate Shelf-Margin and Slope Facies, Central Basin Platform and Hueco Mountains, Permian Basin, west Texas, USA, *in* Verwer, K., Playton, T., and Harris, P., eds., Deposits, architecture and controls of carbonate margin, slope, and basinal settings, Volume 105, SEPM Special Publication, p. 305-333.

Waite, L. E., 1993, Upper Pennsylvanian Seismic Sequences and Facies of the Eastern and Southern Horseshoe Atoll, Midland Basin, West Texas: Chapter 8, *in* Loucks, R. G., and Sarg, J. F., eds., Carbonate Sequence Stratigraphy: Recent Developments and Applications, AAPG Memoir, 57, p. 213-240.

Walker, D., Golonka, J., Reid, A., and Reid, S., 1995, The effects of paleolatitude and paleogeography on carbonate sedimentation in the late Paleozoic, *in* Huc, A.-Y., ed., Paleogeography, Paleoclimate, and Source Rocks, AAPG Studies in Geology, 40 p. 133-155.

Wanless, H. R., and Dravis, J., 2008, Role of storms and prevailing energy in defining sediment body geometry, composition, and texture on Caicos Platform: Developing Models and Analogs for Isolated Carbonate Platforms—Holocene and Pleistocene Carbonates of Caicos Platform, British West Indies, p. 13-20.

Wanless, H. R., and Shepard, F. P., 1936, Sea level and climatic changes related to late Paleozoic cycles: Bulletin of the Geological Society of America, v. 47, no. 8, p. 1177-1206.

Watney, W. L., 1984, Recognition of favorable reservoir trends in Upper Pennsylvanian cyclic carbonates in western Kansas, *in* Hyne, N. J., ed., Limestones of the Mid-Continent, Volume 2, Tulsa Geol. Soc. Spec. Publ., p. 201-246.

Weber, L. J., Francis, B. P., Harris, P. M., and Clark, M., 2003, Stratigraphy, lithofacies, and reservoir distribution, Tengiz Field, Kazakhstan, *in* Ahr, W. M., Harris, P. M. M., Morgan, W. A., and Somerville, I. D., eds., Soc. Econ. Paleontol. Mineral. Spec. Publ. 78 and AAPG Memoir 83, p. 351-394.

West, R., Archer, A., and Miller, K., 1997, The role of climate in stratigraphic patterns exhibited by late Palaeozoic rocks exposed in Kansas: Palaeogeography, Palaeoclimatology, Palaeoecology, v. 128, no. 1-4, p. 1-16.

Wignall, P. B., and Maynard, J. R., 1996, High-resolution sequence stratigraphy in the early Marsdenian (Namurian, Carboniferous) of the central Pennines and adjacent areas: Proceedings of the Yorkshire Geological Society, v. 51, no. 2, p. 127-140.

Witzke, B. J., 1990, Palaeoclimatic constraints for Palaeozoic palaeolatitudes of Laurentia and Euramerica: Geological Society, London, Memoirs, v. 12, no. 1, p. 57-73.

Wright, V., 1992, Speculations on the controls on cyclic peritidal carbonates: ice-house versus greenhouse eustatic controls: Sedimentary Geology, v. 76, no. 1-2, p. 1-5.

Wright, W. R., 2011, Pennsylvanian paleodepositional evolution of the greater Permian Basin, Texas and New Mexico: Depositional systems and hydrocarbon reservoir analysis: AAPG Bulletin, v. 95, no. 9, p. 1525-1555.

Yang, K.-M., and Dorobek, S. L., 1995, The Permian Basin of west Texas and New Mexico: flexural modeling and evidence for lithospheric heterogeneity across the Marathon Foreland, *in* Dorobek, S. L., and Ross, G. M., eds., Stratigraphic Evolution of Foreland Basins, Soc. Econ. Paleontol. Mineral. Spec. Publ. 52, p. 37-50.

Zachos, J., Pagani, M., Sloan, L., Thomas, E., and Billups, K., 2001, Trends, rhythms, and aberrations in global climate 65 Ma to present: Science, v. 292, no. 5517, p. 686-693.

Zhang, T., Bombarde, S., Strebelle, S. B., and Oatney, E., 3D porosity modeling of a carbonate reservoir using continuous multiple-point statistics simulation, *in* Proceedings SPE Annual Technical Conference and Exhibition2005, Society of Petroleum Engineers.